

Lawrence Berkeley National Laboratory

Recent Work

Title

THE MESON SPECTRUM IN THE REACTION $pp \rightarrow d \pi^+$

Permalink

<https://escholarship.org/uc/item/4708m15t>

Author

Wicklund, Arthur Barry.

Publication Date

1970-03-01

C. 2

RECEIVED
LAWRENCE
RADIATION LABORATORY

JUN 15 1970

LIBRARY AND
DOCUMENTS SECTION

THE MESON SPECTRUM IN THE REACTION $PP \rightarrow d MM$

Arthur Barry Wicklund
(Ph. D. Thesis)

March 1970

AEC Contract No. W-7405-eng-48

TWO-WEEK LOAN COPY

This is a Library Circulating Copy
which may be borrowed for two weeks.
For a personal retention copy, call
Tech. Info. Division, Ext. 5545

LAWRENCE RADIATION LABORATORY
UNIVERSITY of CALIFORNIA BERKELEY

DISCLAIMER

This document was prepared as an account of work sponsored by the United States Government. While this document is believed to contain correct information, neither the United States Government nor any agency thereof, nor the Regents of the University of California, nor any of their employees, makes any warranty, express or implied, or assumes any legal responsibility for the accuracy, completeness, or usefulness of any information, apparatus, product, or process disclosed, or represents that its use would not infringe privately owned rights. Reference herein to any specific commercial product, process, or service by its trade name, trademark, manufacturer, or otherwise, does not necessarily constitute or imply its endorsement, recommendation, or favoring by the United States Government or any agency thereof, or the Regents of the University of California. The views and opinions of authors expressed herein do not necessarily state or reflect those of the United States Government or any agency thereof or the Regents of the University of California.

Contents:

Section I; Introduction.....	1
Section II; Hardware, Logic, and Event Selection.....	11
Section III; Resolution and Track Analysis.....	20
Section IV; Acceptance, Detection Efficiency, and Beam Contamination.....	31
Section V; Normalization.....	46
Section VI; Final Data Averaging.....	53
Section VII; Fitted Cross-sections.....	57
Appendix 1; Orbit Analysis.....	67
Appendix 2; Fitting the Orbit Parameters.....	73
Appendix 3; Beam Optics.....	77
Appendix 4; Acceptance.....	82
Appendix 5; Cerenkov Efficiency Corrections.....	84
Appendix 6; Kinematic Reflections.....	87
Tables.....	89
Figures.....	107
References.....	179
Acknowledgments.....	182

Tables:

1. Tallies of numbers of events obtained.
2. Expressions used in beam optics calculations.
3. (a) Differences (in standard deviations $\times 10$) of individual runs from averages of neighboring runs. (b) Break-down of variances and cross-sections for each momentum bin. (3.8 gev/c-1).
4. Same as 2, for 3.8 gev/c-2
5. Same as 2, for 4.5 gev/c-1
6. Same as 2, for 4.5 gev/c-2
7. Same as 2, for 6.3 gev/c-1
8. Same as 2, for 6.3 gev/c-2.
9. Overlap chisquares for the individual runs in each experiment.
10. Fitted cross-sections and resonance parameters at each energy.
11. Fitted pion peak masses and widths, and estimates for the mass calibration accuracy near 1 gev missing mass.
12. Kinematic quantities of interest at various beam energies.

Figure Captions.

1. Secondary beam layout.
2. (a) Event timing sequence, showing particle detection, event digitization, and chamber recharging separately.
(b) block diagram of the experimental layout.
3. Block diagram of the electronic fast logic.
4. Block diagram of the spark chamber triggering logic.
5. Recorded time of flight plotted against time calculated from fitted momentum.
6. Fraction of deuterons rejected by the cerenkov counter, and fraction of protons detected, versus momentum.
7. Derivate of M^2 versus beam momentum, secondary momentum and production angle both at 0° and in the Jacobean peak region.
8. Spectrometer resolution.
9. M^2 resolution, including fitted π peak widths.
10. Confidence level distributions for 3.8 gev/c data!
11. Events in the π peak region fitted with various chamber configurations.
12. Normalized pull quantities for various deuteron momenta.
13. Accepted solid angle versus dP/P_0 , for a point source, and for a diffuse source displaced .5" vertically.
14. Momentum spectra for 3.8 gev-1.
15. Same as 14, 3.8 gev/c-2.

16. Same as 14, 4.5 gev-1
17. Same as 14, 4.5 gev-2
18. Same as 14, 6.3 gev-1
19. Same as 14- 6.3 gev-2.
20. Schematics of upstream beam optics.
21. Beam optics through the spectrometer.
22. Correlation between horizontal entrance coordinates and slopes, versus dP/P .
23. Correlation between vertical entrance coordinates and slopes, versus dP/P
24. Measured vertical image size at the spectrometer entrance versus dP/P .
25. Measured excess steering in horizontal and vertical planes versus dP/P .
26. Systematic error in the spectrometer detection efficiency versus the calculated weight. These errors depend on dP/P indirectly through the weight.
27. Measured rms. coulomb scattering angles in the front scintillators versus momentum.
28. Spectrometer entrance coordinates plotted against slope discrepancies.
29. Discrepancies in the observed chamber coordinates (caused mainly by scattering in C1C2).
30. Horizontal and vertical acceptance plotted against dP/P ; one unit represents the size of the collimator entrance.
31. Beam profiles for typical data.
32. Normalized acceptance coordinates (horizontal) plotted against observed slope deviations; only $dP/P = 0$ rays are used.

33. Fraction of deuterons associated with the primary beam halo versus apparent normalization errors in the target empty cross-sections, for runs from 4.5 gev-2.
34. Average distribution of dP/P for events in and out of the beam halo, showing the peaking of halo associated events at $dP/P = -.06$.
35. (a) Correction for Cerenkov rejection of deuterons with normal logic (solid) and with logic of 3.8 and 4.5 gev-1 (dashed). (b) Fraction of accidentals that are not rejected by the cerenkov veto or by the timing requirement.
36. Typical distribution of normalized collimator entrance coordinates, for central momentum rays.
37. Target empty rates for 3.8 gev-1.
38. Same as 37, 3.8 gev-2
39. Same as 37, 4.5 gev-1
40. Same as 37- 4.5 gev-2
41. Same as 37 , 6.3 gev-1
42. Same as 37, 6.3 gev-2.
43. Subtracted Laboratory cross-sections, 3.8 gev-1
44. Same as 43, 3.8 gev-2
45. Same as 43, 4.5 gev-1
46. Same as 43, 4.5 gev-2
47. Same as 43, 6.3 gev-1
48. Same as 43, 6.3 gev-2.
49. Fitted differences between the laboratory cross-sections of 3.8 gev -1 and 2 and between 4.5 gev-1 and 2.
50. Superposed c.m. differential cross-sections, 3.8 gev, 1 and 2.
51. Same as 50, 4.5 gev, 1 and 2.

52. Same as 50, 6.3 gev, 1, 2.
53. C. M. cross-sections at 3.8 gev.
54. C. M. cross-sections, 4.5 gev
55. C. M. cross-sections, 6.3 gev.
56. C. M. cross-sections at 4.5 gev with systematic 5% magnification error.
57. C. M. cross-section at 3.8 gev, fitted.
58. Fitted c. m. cross-section at 4.5 gev.
59. Fitted c. m. cross-section at 6.3 gev.
60. Laboratory cross-sections.
61. Differences, averaged over beam energies, of measured c. m. cross-sections from fits to a linear expression in the laboratory momentum.
62. Fit chisquares versus 'delta' cross-section. (a) 3.8 gev, (b) 4.5 gev, (c) 6.3 gev.
63. Fit chisquares versus delta cross-section for various widths; (a) 3.8 gev, (b) 4.5 gev, (c) 6.3 gev.
64. Fit chisquare versus delta width for various cross-sections; (a) 3.8 gev, (b) 4.5 gev, (c) 6.3 gev.
65. Production diagrams for 2π and 3π final states.
66. Phase space contributions for various final states, in absolute units as defined in the text.
67. C. M. cross-section, $d\sigma/dM$ measured by Banner et. al. at 3.8 gev, showing the estimated contribution from a broad delta resonance at 975 mev.
68. Cross-sections minus linear background measured by Kienzle et. al., expressed in standard deviations, showing both their gaussian fit and a 50 mev wide Breit Wigner expression.
69. Excitation curves for pion, rho, and delta meson production plotted against P_{lab} .

70. Coordinate system used in defining particle orbits
in the spectrometer.

Section I- Introduction

In this report we present new experimental data on the non-strange, isospin 1 meson spectrum in the mass region around 1 gev. We first summarize the physical and historical issues that are pertinent to this study; other surveys of the existing experimental information may be found in the literature. (1), (2), (38)

The original observation of a narrow ($\Gamma < 5$ mev) resonance at 963 mev produced in the reaction $\pi^- P \rightarrow X^- P$ has not been convincingly confirmed or denied by any subsequent experiment. (3) The first apparent confirmation of this result of the CERN missing mass spectrometer (MMS) experiment was in the study of the reaction $PP \rightarrow dX^+$ at 3.8 gev/c incident momentum at Saclay. (4) With a resolution of 60 mev fwhm. in the mass, this experiment reported a 5 standard deviation (s. d.) enhancement at 960 mev in the mass. However, a subsequent study of the same reaction at Saclay by Banner et. al. (5), at the same beam energy and with the same technique (a narrow band magnetic spectrometer) revealed a smooth, featureless missing mass spectrum. No detailed information on the decay products of the ' $\delta(963)$ ' is provided by the CERN MMS. experiment, except that there is a 50% branching ratio into three or more charged particles. Perhaps it is important to note that the ratio of δ^+ to ρ^+ intensities is only 1%. Banner et. al. (6) also repeated the study of $\pi^- P \rightarrow X^- P$ at 1.8 gev/c incident momentum; although no evidence for the $\delta(963)$ was found, the upper limit was more than 1% of the ρ cross-section.

More recently, two experiments report an enhancement in the $\eta\pi^-$ mass spectrum from the reaction $K^-P \rightarrow \pi^+\pi^-\eta$. With a mass resolution of 40 mev (fwhm.), Ammar et. al. (7) report a mass and width of 980 ± 10 mev and 80 ± 30 mev respectively. With comparable resolution, Barnes et. al. (8) find a mass of 970 ± 15 mev and width less than 50 mev. In addition, Barnes et. al. give upper limits for the 2π , 3π , and $K\bar{K}$ decay modes that are essentially equal to the observed $\eta\pi$ decay rate. Crennel et. al. (9) argue that this ' $\pi_n(980)$ ' enhancement can be attributed to $\pi^0\pi^0$ background in the η signal; $\rho\pi$ formation in the resulting 3π system can produce a peak around 1 gev. However, Barnes et. al. and Ammar et. al. (38) find that this explanation gives a wider peak displaced from the observed resonance position that cannot account for the effect. This criticism may, nonetheless, apply to the observed enhancement in the $\eta\pi^-$ signal in the reaction $K^-n \rightarrow \eta\pi^-$ reported by Miller et. al. (39). Parenthetically, it is clearly desirable to study the $\eta\pi$ system with better resolution and better signal to noise ratio in the identification; this would require detecting the 2γ decay mode.

Two other experiments report production of $\pi_n(980)$ as a decay product of the $D^0(1285)$, with the $\pi_n(980)$ subsequently decaying into $\eta\pi$. Campbell et. al. (10), studying the reaction $\pi^+d \rightarrow P_S P \pi^+\pi^-\eta$, report a mass and width of 980 ± 10 mev and 40 ± 15 mev, and a branching ratio $D^0 \rightarrow \bar{K}K^0\pi / D^0 \rightarrow \pi_n\pi = .16 \pm .08$. Defoix et. al. (31) obtain similar results from a study of the reaction $P\bar{P} \rightarrow 2\pi^+2\pi^-\eta$; they find a mass and width of 975 and 25 mev, and a branching ratio of $.12 \pm .04$.

The importance of the D^0 branching ratio into $K\bar{K}$ lies in the possible connection between the $\pi_n(980)$ and the ' $\pi_n(1016)$ '; the latter is seen as a threshold enhancement in the $K\bar{K}$ system in a variety of $P\bar{P}$ annihilation channels.⁽¹²⁾ Examination of D^0 decay (produced in $P\bar{P}$) suggests that the dominant decay mechanism may be through the $\pi_n(1016)$ channel.⁽¹¹⁾ Thus, if $\pi_n(980)$ and $\pi_n(1016)$ are manifestations of a single enhancement, then the D^0 branching ratio measures the relative probability $\pi_n \rightarrow K\bar{K} / \pi_n \rightarrow \eta\pi$. Astier et. al.⁽¹²⁾ studying the channel $P\bar{P} \rightarrow \pi_n(1016)\pi$, give a lower limit of .2 for the ratio $\pi_n(1016) \rightarrow K\bar{K} / \pi_n(1016) \rightarrow \eta\pi$; this is barely consistent with the upper limit inferred from D^0 decay into $\pi_n(980)$, namely about .24.

Before pursuing this identification problem further, we consider the possible quantum numbers of the isovector resonances seen in the major two particle channels; these are summarized as follows:

JPC	0 ^{-*}	0 ^{+*}	0 ⁻⁺	0 ⁺⁺	1 ⁻⁻	1 ⁺⁻	1 ^{-+*}	1 ⁺⁺	2 ⁻⁻	2 ^{+*}	2 ⁻⁺	2 ⁺⁺
$\pi\pi$					G=1							
$\eta\pi$				G=-1		G=-1						G=-1
$(K\bar{K})^{+-}$				G=-1		G=1						G=-1
$K_1\bar{K}_2$					G=1							
$K_1\bar{K}_1$				G=-1								G=-1
π			G=-1				G=-1	G=-1				G=-1
π	G=1					G=1	G=1		G=1	G=1		

Empty entries in the table are victims of extended Bose statistics or C and P conservation, etc. The columns marked with an asterisk are incompatible with the quark-

antiquark model of meson spectroscopy⁽¹³⁾; thus, the triplet $q\bar{q}$ states have $C = -1^{L+1}$, $P=C$, while the singlet states have $C = -1^J$, $P = -C$, so that possibilities like $J^{PC} = 1^{-+}$ are ruled out. However, a more fundamental consideration applies to some of these channels, namely the fact that the couplings are forbidden by SU(3) invariance. Without working out the Clebsch-Gordon coefficients, this can be seen as follows: C invariance in the decay into two pseudoscalar mesons requires pure D or F type coupling, depending on whether C is even or odd; extended Bose statistics, implied by ordinary Bose statistics plus SU(3) invariance, then constrains the symmetry of the spatial wave function of the decay mesons. Thus, if the $\eta\pi$ enhancement were 1^{-+} (C must be even from G parity conservation), the $\pi_n(980)$ wave function would be antisymmetric (P wave) even though the SU(3) wave function must be symmetric to give positive C parity. Note that it is not possible to observe this type of SU(3) violation by studying $\pi\pi$ interactions, which are constrained by isotopic spin invariance. To study violations of the quark model classification scheme that do not break SU(3) symmetry, one must examine $\rho\pi$ and $\omega\pi$ channels, where Bose statistics do not apply.

The experimental data have not yielded a definite spin assignment for the $\pi_n(980)$. However, the apparent absence of the $\rho\pi$ decay mode favors the 0^{++} assignment. In general, there is no evidence for 2π or 3π decay modes; reports of enhancements in the 3π spectrum in this region are statistically weak and do not coincide in mass.^{(14), (15)}

In the case of the $\pi_n(1016)$, the observation of the K_1K_1 mode

rules out the odd spin assignments, and the low q value of the decay then makes the 0^{++} assignment most probable. Thus, a common 0^{++} assignment for $\pi_n(980)$ and $\pi_n(1016)$ would be consistent with present data.

Several interpretations of the $K\bar{K}$ spectrum give satisfactory fits to the data, according to Astier et. al. (12): (1) a positive or a negative complex scattering length, with $\text{Im}(A_S)/\text{Re}(A_S)$ less than .25; (2) a resonance in $K\bar{K}$ at 1016 mev with width 25 mev. The negative scattering length solution requires a $K\bar{K}$ bound state at 975 mev; this can produce a 'virtual bound state resonance' in the $\eta\pi$ channel (see Dalitz, (16)). Briefly, the width of the virtual resonance is governed by the coupling between the $\eta\pi$ and $K\bar{K}$ systems, which allows virtual transitions from $\eta\pi$ to the $K\bar{K}$ bound state; the width is given approximately by

$$\Gamma \approx \text{Im}(A_S)/\text{Re}(A_S) \cdot 8 k_r^2 \quad \text{I-1}$$

where k_r is the (magnitude of the $K\bar{K}$ C.M. momentum at 980 mev, so that Γ is less than 15 mev. The narrow width implies a small coupling to the $\eta\pi$ channel, and a production ratio $\eta\pi/K\bar{K}$ given approximately by

$$\frac{g_{\eta\pi}^2}{g_{K\bar{K}}^2} = \frac{\int ds q_{\eta\pi} / (s-s_r)^2 + (M\Gamma)^2}{\int ds q_{K\bar{K}} / (s-s_r)^2} \quad \text{I-2}$$

where the effective couplings, deduced from the elastic scattering amplitudes, are

$$g_{\eta\pi}^2 = 2 \text{Im}(A_S)/\text{Re}(A_S) \cdot (4M_k^2 - s_r)/q_r,$$

$$g_{K\bar{K}}^2 = 8 (M_k^2 - s_r/4)^{1/2}$$

In any case, these consequences of the bound state solution

do not agree well with the $\pi_n(980)$ data summarized above.

An alternate possibility is a resonance below $K\bar{K}$ threshold which decays into $K\bar{K}$ and $\eta\pi$; the branching ratio depends on the width and relative vertex strengths. Specifically, the symmetric SU(3) coupling for $0^{++} \rightarrow 0^{-}0^{-}$ predicts a ratio of 2/3 for $g_{\eta\pi}^2 / g_{K\bar{K}}^2$. Assuming factorizable residues, the width is constrained by extended unitarity to be proportional to $q_{\eta\pi} g_{\eta\pi}^2$ below $K\bar{K}$ threshold and to $(q_{\eta\pi} g_{\eta\pi}^2 + q_{K\bar{K}} g_{K\bar{K}}^2)$ above threshold. Then the ratio of the decay rates $K\bar{K}/\eta\pi$ is approximately 16% if the width is greater than 40 mev, consistent with the estimates derived from $\pi_n(1016)$ decay and from D^0 decay.

In the present experiment we find evidence for an isospin one object produced in the reaction $PP \rightarrow dX^+$ with mass 975 mev and width 60 mev. Since our mass resolution is 12 mev (fwhm.), we can rule out the possibility that this is really the narrow ' $\delta(963)$ ', a problem that is not entirely resolved for the other experiments. The production ratio of ' δ ' to ρ in our experiment is about 20%, not 1% as in the CERN MMS. results. Indeed, even if these objects are identical, we might expect to see a large suppression of ' δ ' relative to ρ production in the MMS. reaction $\pi^-P \rightarrow X^-P$. The logical exchange mechanisms that can produce the $\pi_n(980)$ in this reaction are the η and D^0 trajectories (and possibly the B trajectory, although the decay $B \rightarrow \pi_n(980)\pi$ has not been observed). In the case of the η trajectory, the measured F/D ratio for the coupling $B\bar{B}P$ implies that the $P\bar{P}\eta$ vertex is 10 times weaker (absolute square) than the $P\bar{P}\pi^0$ vertex. ⁽¹⁷⁾ The ratio of δ to ρ production should be approximately .08. ⁽¹⁸⁾ By contrast, we expect the reaction $PP \rightarrow dX^+$ to be dominated by exchange of isospin 1/2 nucleon trajectories, so that

the ratio of δ production to ρ production is given by $1/3 g_{\delta \bar{P}N}^2 / g_{\rho \bar{P}N}^2$ ⁽¹⁸⁾. Note that the isovector couplings do not depend on the F/D ratio.

Other missing mass studies involving fermion exchange, specifically in the reaction $\pi^- P \rightarrow PX^-$, fail to show any $\pi_n(980)$ signal. ⁽¹⁹⁾ However, this reaction forbids ispin 1/2 exchange in the 'u' channel, whereas in $PP \rightarrow dX^+$ this is the only allowed exchange. Thus, the meson spectrum in the two reactions need not be comparable.

Finally we note that our experiment is in disagreement with Oostens et. al. ⁽⁴⁾ who report evidence for a narrow ' δ '; their mass spectrum at 3.8 gev/c is considerably more structured than ours. At this energy, our conclusions are consistent with Banner et. al. ⁽⁵⁾ who observe no fine structure in the ' δ ' region in the same reaction. As we discuss below the rapid variation of the background phase space in the ' δ ' mass region at 3.8 gev/c makes broad resonance structure virtually undetectable.

The real importance of meson spectroscopy and missing mass experiments will probably not be evident until more conclusive experimental results are obtained. At least in the simple quark-antiquark model of Dalitz ⁽¹³⁾ a $J^{PC} = 0^{++}$ object is needed to fill the P wave levels. Thus, assigning the isovector mesons A2(1300), B(1200), and A1(1080) to the $^3_2 p_2$, $^1_1 p_1$, and $^3_1 p_1$ $q\bar{q}$ states respectively, a spin-orbit mass splitting mechanism ($M^2 = J \cdot J + 1 - L \cdot L + 1 - S \cdot S + 1$) predicts a $^3_0 p_0$ level at 950 mev. Accomodation of two such levels nearby in mass, namely the $\pi_n(980)$ and the $\pi_n(1016)$ would require new fine structure mechanisms. Clearly, from this phenomenological point of view, it is desirable to clarify this part of the meson spectrum.

General Experimental Considerations:

In this experiment we measure the missing mass in the reaction $PP \rightarrow d MM$ at incident momenta of 3.8, 4.5, and 6.3 gev/c. The deuterons are produced at 180° in the center of mass system and are detected at 0° in the laboratory with momenta between 1 and 2 gev/c. There is no kinematic overlap between deuterons produced forward and backward in the center of mass system in this range of laboratory momenta. The separation of deuteron events from a much larger background of charged secondaries is accomplished with a water cerenkov detector and time of flight measurement. No attempt is made to detect other particles produced with the deuteron.

The topics covered in this report are as follows: in section II we discuss event selection and other on-line aspects of the experiment; section III treats the momentum analysis and resolution, comparing the precision of our spectrometer with comparable experiments based on the 'Jacobean Peak' method; analysis of acceptance and detection efficiency is taken up in section IV; section V explains normalization procedures and systematic corrections to the cross-sections; the internal consistency of the data is studied in VI; the statistical significance of the fitted results is discussed in VII.

Before discussing these detailed aspects of the experiment, we review the principal considerations that affect the validity of the results. Kinematically, the missing mass depends only on the deuteron momentum in this reaction; the momentum is measured in a magnetic spectrometer with six wire spark chambers employing magnetostrictive readout. Our mass

resolution (f. w. h. m.), at a missing mass of 1 gev, is 8, 13, and 23 mev respectively at the incident momenta 3.8, 4.5, and 6.3 gev/c. The entire beam system, including a 3" liquid hydrogen target, two additional bending magnets, and a quadrupole doublet, is illustrated in figure 1.

In order to achieve the desired momentum resolution, it is necessary to distribute the spark chambers over 20' lever arms, tuning the spectrometer magnet to a 15° bend. Since the chambers are only 10"X10", this limits the momentum acceptance of the spectrometer; for the entire beam transport system the full base acceptance is 25%, and only the central 13% band is useful for final analysis. Thus, to cover the momentum region from 1100 to 2000 mev/c, the data must be taken in overlapping spectra, and around the 'delta' region these distributions have useful mass widths of 130, 180, and 330 mev respectively at the three incident beam momenta. The solid angle acceptance varies by 50% over the range of each distribution, and additional detection efficiency corrections vary by up to 15%. As a result, to detect a physical effect as wide as the Rho meson, great care must be taken in unfolding the distributions, and the mutual consistency of different spectra must be examined. On the other hand, the high resolution makes it straightforward to detect narrow enhancements- these should appear in the individual spectra before unfolding. Ultimately, to determine the acceptance and detection efficiency with sufficient precision, it is necessary to impose severe fiducial cuts on the data- these accept 35 to 50% of the events. In spite of this, 450,000 target full events and 170,000 target empty events are available for the final analysis;

the relevant statistics for the experiment are listed in table I.

Signal to noise ratio is another critical consideration. Referring again to figure 1, deuterons are produced in a 3" long cylindrical hydrogen target (3" in diameter) in the external proton beam at the Bevatron. The target is small so that random energy loss in the hydrogen is negligible. The amount of non-hydrogen material exposed to the beam must be minimized, since deuterons are produced more copiously per gram of material off of heavier nuclei; ⁽²⁰⁾ mylar and kapton windows in the target and beam pipes (.05" total) represent the mass equivalent of 1" of liquid hydrogen. The target full to empty ratio varies from 5 to 1, and is largest at high deuteron momenta and low incident energy. The data is taken in runs consisting 15,000 to 40,000 target full events followed by 5,000 to 15,000 target empty events.

The incident beam flux is typically $3 \cdot 10^{10}$ protons over a 200 to 500 msec. flattop. Beam intensity is monitored by the counters M1-M2 in figure 1, which detect secondaries produced at 80° to the beam line. The absolute normalization accuracy about $\pm 12\%$ for the final cross-sections.

As indicated in table 1, the data is organized into six independent experiments, two at each beam energy. Systematic differences exist between the results of these experiments due to changes in the experimental logic, as discussed below. In the final analysis we require consistency between the experiments and the runs within the experiments, and these requirements in turn lead to a clearer understanding of the systematic errors. We now turn to the experimental details.

Section II- Hardware, Logic, and Event Selection

Data Acquisition:

The data retrieval system is discussed in Ref. 21, and figure 22 shows a block diagram of the system and also of the timing sequence involved in processing an event. The fast logic identifies a deuteron event by suitable time of flight and Cerenkov radiation criteria, and triggers the spark chambers every 10 msec., depending on the deuteron flux. The spark chamber coordinates, twelve in all, are located by magnetostrictive readout; each chamber provides two coordinates sandwiched between pairs of fiducials, and the relative time lapse between these signals is digitized by scalars that are connected to a 10 MHz quartz clock. The output from this chamber logic is stored in the PDP-5 computer memory, together with the digitized time of flight supplied by the fast logic. At the end of each Bevatron burst, this data (up to 50 deuteron events) is written onto magnetic tape. Each tape record also contains the readings of eight TSI scalars, which monitor various counting rates, and the output from a digital voltmeter, which monitors the magnet currents. Under reasonably good running conditions 20,000 events can be recorded per hour. Some on-line analysis is done to improve the data quality; specifically, the PDP-5 monitors the spark chamber efficiencies, and a pulse height analyzer stores the time of flight distributions, providing a handle on the deuteron separation and on the momentum acceptance characteristics.

Chamber Operation:

The chambers are constructed of two 10"X10" planes of .007" copper wires oriented at 90° to one another; the wire spacing is 1 mm. and the gap is 1 cm. Neon-helium gas (90% Ne, 10% He) is circulated through the chambers ($30 \text{ cm}^3/\text{min.}$). In order to reduce multiple scattering in the spectrometer, which is a severe problem in detecting 1 to 2 gev/c deuterons, helium bags are placed between the chambers; to contain this helium and the chamber gas, an additional .01" thickness of mylar is needed for each chamber.

The triggering logic is outlined in figure 4. The spark gap trigger amplifier supplies a 10 KV pulse to break down the main spark gap; this process is catalyzed by ultraviolet radiation from the corona lamp. The rise time for the chamber voltage, given by the product of the gap resistance and the chamber capacitance, is about 3 nsec. The chamber's stray capacitance is kept small by the use of lucite instead of metal bars to support the magnetostrictive wand. The 1800 Pf. condensor holds the chamber voltage for 400 nsec., and the lifetime for a spark avalanche is about 30 nsec. Two fiducial wires in each plane are pulsed when the chamber voltage is dropped; jitter in the spark timing as compared with the fiducial timing has negligible effect on the chamber coordinates- a 10 nsec. jitter in the timing of the electrical pulse would cause a .05 mm. variation in the position of the acoustic wave. After a discharge occurs, it takes 10 msec. for the power supply, which is in parallel with large storage condensers, to restore the 5 KV bias on the main gap.

A 90 volt clearing field is kept on the high voltage plane to erase old tracks. Chamber efficiency is limited mainly by reignitions, which appear in the data as a fiducial followed by two coordinates instead of by a coordinate and a fiducial (any spark produces an acoustic pulse which precedes the last fiducial signal). It was learned that increasing the clearing field over a wide range did little to cut down on the reignitions; however, substantial reduction in the number of spurious discharges is achieved by passing the chamber gas over alcohol (at 0°); the alcohol vapor picked up the ultraviolet radiation produced by the spark avalanche. The number of missed sparks is negligible. On the average, 80 to 85% of the events have single output coordinates in the horizontal plane in all six chambers, and fewer than 1% of the events have double sparks in more than two chambers. Deterioration of the magnetostrictive wand reduces the quality of the output signals; in particular, the wand next to the high voltage plane oxidizes rapidly until the acoustic pulses become unacceptable.

The use of magnetostrictive readout is discussed in Ref. 22, and details pertaining to the magnetostrictive properties of materials can be found in Ref. 23. Briefly, the time varying magnetic field associated with a current pulse in a wire generates a longitudinal stress in the Fe-Co wand; this wave is detected by a small coil around the end of the wand, where the acoustic pulse generates a time varying magnetic flux. The output voltage pulse from this coil, about 1 microsec. long, is amplified and differentiated to locate the center of the pulse. These pulses are clocked by the scalers with a least count of .5 mm. (this least count is determined by the speed of sound, $5 \cdot 10^5$ cm./sec., and the time intervals supplied by the quartz

clock, 10^{-7} sec.). The true spatial resolution of the spark chambers, .75 mm., is deduced from the 'straightness' of the fitted tracks, as discussed in section III.

Fast Logic

Figure 3 shows a block diagram of the fast logic, which consists of 50 and 100 MC Chronetics and E. G. & C. components. During the Bevatron spill, 20 to 100 deuterons are selected from a background of 20,000 pions and protons by means of a water cerenkov detector (C) and time of flight requirement. Referring again to figure 3, a trigger is defined by the coincidence $C1-C2-C3-C4-C5-\bar{C}$. All triggers are counted on one scaler to determine the cross-section normalization; the spark chambers are fired only when (1) no chamber trigger has occurred in the previous 10 msec., and (2) no C1-C2 coincidence has occurred in the previous 2 microsec. (to avoid double tracks). The cerenkov signal vetoes the C3-C4-C5 coincidence for 50 nsec., causing a total dead time of about 1 msec. out of the spill. The event coincidence allows a total time spread of 7 nsec. on either side of the nominal time of flight, which is determined by the momentum tuning for each run. For subsequent analysis the time to amplitude converter measures the time of flight for each recorded event.

All counter coincidences are gated by a signal which measures the Bevatron ring's magnetic field; the time derivative of the field, measured by a coil in the ring, is integrated, and a gate signal is generated when this integrated voltage lies within preset limits.

The following coincidences are recorded by the scalers for

subsequent analysis: the counts from M1-M2 monitoring primary beam intensity; the coincidence rate between M1 and M2 when the latter is arbitrarily delayed (to estimate accidental rates); C3-C4-C5 and C3-C4-C5- \bar{C} where the cerenkov signal is delayed 30 nsec. (to determine dead time losses); also the spark chamber trigger rate and the total rate as stated above.

From measured time of flight spectra, we conclude that the cerenkov anticoincidence eliminates at least 98% of the secondaries that have v/c greater than .75 (the threshold v/c for cerenkov light; the corresponding proton momentum is 1070 mev/c). The time-of-flight separation leaves a negligible background of non-deuterons. By comparing measured time of flight with the time deduced from the momentum determination, we conclude that the time resolution of the scintillators is at least 3 nsec. f. w. h. m. ; this resolution is achieved by using two photomultiplier tubes with each counter to minimize variations in the light transit time. This resolution is to be compared with the flight time difference between protons and deuterons over the 44' path from C1-C2 to C3-C4-C5; this ranges from 29 nsec. at 1100 mev/c to 15 nsec. at 1900 mev/c. Thus the 14 nsec. gate requirement imposed on the C1-C2-C3-C4-C5 coincidence is by itself sufficient to reject any protons that survive the cerenkov veto. In any case, further refinement of the deuteron sample is accomplished by eliminating events in which the momentum is inconsistent with the time of flight.

Figure 5 shows the linear correlation between measured times of flight and the times deduced from momentum determination. In the 6.3 gev/c data, which is representative of four of the six experiments performed, three distinct bands of

events are evident, corresponding to protons, deuterons, and pions- these events have all survived the cerenkov and coincidence gate requirements. It is probable that the non-deuteron events are in fact associated with a failure of the gate on the time to amplitude converter, which is supposed to ensure that a time of flight is measured only when a deuteron trigger occurs. The momentum distributions of the 'non-deuteron' events show the narrow peak associated with the reaction $PP \rightarrow d\pi^+$. Thus, the net effect of the apparent non-deuteron contamination in figure 5 is to introduce a 2-3% normalization uncertainty; the momentum distributions are correct, since only the 'deuteron' events are accepted for analysis.

The second plot in figure 5 is representative of the first experiments at 3.8 and 4.5 gev/c. A significant cluster of events with measured time of flight greater than 73 nsec. is evident, events that are apparently not deuterons. The fast logic for this data differs from the diagram in figure 3 in that the cerenkov veto is applied to the C1-C2 coincidence rather than to the C3-C4-C5 coincidence. The anomalous events in figure 5 are accidentals; a proton can trigger the C1-C2 scintillators and miss the last counters and the cerenkov detector. If this is followed within 20 to 30 nsec. by a second particle, then the timing between the first C1-C2 count and the second C3-C4-C5 signal simulates a deuteron event. The cerenkov signal from the second proton vetoes the second C1-C2 coincidence but not the first. The accidentals in figure 5 have measured times of flight greater than 73 nsec. The reason for this is that the cerenkov signal arrives at the C1-C2

coincidence unit in time to anti a non-deuteron event- one with time of flight between 23 and 73 nsec.

With the improved logic of figure 3, accidentals are extremely unlikely; only secondaries that fail to trigger the cerenkov counter after passing through C3-C4-C5-C can contribute to this contamination. However, there is considerable loss of flux between the first and the last sets of counters (as much as 30%), so that large accidental rates are possible with the setup described above. It may seem paradoxical that the accidental rates are as large as implied by figure 5. Even with a duty factor of 10, we expect an average separation of 1000 nsec. between protons. However, the proton flux is 1000 times greater than the deuteron signal; if only .1% of the protons are followed by a second particle within 30 nsec., which is consistent with the 1000 nsec. average time separation, then 10 accidentals are expected per spill.

Efficient rejection of accidentals is possible for momenta greater than 1660 mev/c (then the time of flight in figure 5 is less than 68 nsec.). However, because of the finite time resolution and the jitter in the arrival of the cerenkov veto (about 2 nsec.), the region below 1660 mev/c is characterized by overlapping distributions of deuterons and accidentals; half of the accidentals can be removed by rejecting events in which the measured time of flight exceeds the calculated value by more than 3 nsec. Depending on momentum, the remaining contamination is 8% or less. These residual accidentals are protons or pions and are expected to contribute a smooth background to the momentum distribution that falls to a negligible level above 1650 mev/c; this background cannot produce fine structure in the momentum spectrum.

The number of events with double tracks in the first three chambers in this early data constitutes 8% of the total; after changing the logic, the double track rate falls to 1/2%. Consequently, we reject these events in the early data, attributing them to accidentals, and normalize the spectra accordingly. Additional purification of the sample is achieved by rejecting events with any doubles in the first three chambers; the upper limit of 8% accidental contamination given above applies after these corrections have been made.

Besides accidentals, the early data suffers from the following defect: deuterons can produce a cerenkov signal by exciting fast electrons in the water, so that deuterons are rejected by the cerenkov veto at a predictable momentum dependent rate. The problem is that the deuterons in the early data are rejected by the cerenkov signal only if their time of flight is less than 73 nsec. Thus, if the time resolution of the scintillators and cerenkov detector were perfect, we would observe a sudden drop in the deuteron cross-section above 1550 mev/c (about 20%). Because of the time resolution and the smallness of the derivative dT/dP , there is instead a transition region between 1450 and 1650 mev/c in which the cross section is gradually depleted by the cerenkov veto. This effect, like the accidentals problem, cannot produce fine structure in the spectrum; the net effect is that we must normalize the early data to the later cross-sections gotten with the improved fast logic. We defer the mathematical details of these corrections to section V, where all systematic normalization errors are analyzed.

We conclude this section by noting that the 14 nsec. gate imposed on coincidences is wider than the momentum acceptance of the beam at all momenta; for example, at 1550 mev/c

(the delta region), only a 5 nsec. bite in the center of this gate is used in cross-section analysis.

Section III- Resolution and Track Analysis

Kinematic Considerations

In a 'missing mass' study of the reaction $a+b \rightarrow c+X$, the differential cross-section $d^2\sigma/dP_c d\theta_c$ is measured along a contour in phase space, i. e. $P_c = P_c(\cos\theta_c)$, $P_a = P_a(\cos\theta_c)$; a Jacobean transformation gives the C=M differential cross-section $d^2\sigma/dM_x^2 d\theta_x$ along a corresponding path $\cos\theta_x = \cos\theta(M_x^2)$. The choice of phase space contour determines the mass resolution and also the relation between the missing mass and the C.M. production angle, $\cos\theta_x$; if the latter varies significantly over the desired mass range, then it is necessary to vary the incident beam energy also, since otherwise one cannot distinguish between the mass dependence of the amplitude (i. e., resonance formation) and the angular dependence (diffraction minima, for example).

Two techniques prove to be practical. In the present experiment the laboratory production angle θ_c is fixed at 0° , the beam energy P_a is varied in discrete steps, and M_x^2 depends only on P_c , since $dM_x/d\theta_c = 0$ at $\theta_c = 0$. An alternate method is to use the Jacobean peak, where $dM_x/dP_c = 0$, and M_x depends only on θ_c ; here the recoil energy E_c is chosen for a particular value of M_x , and the cross-section variation with angle is studied for fixed P_c . Note that in this technique, the C.M. production angle must vary with M_x as one sweeps the desired mass range; in the 0° experiment, the C.M. angle is fixed at 0° or 180° . One practical consequence of fixing θ_c is that it is easier to piece together spectra taken at different mass settings, since the phase space contours for each spectrum are part of a continuous contour- namely $\theta_c = 0$.

Specializing to the reaction $PP \rightarrow dX^+$, we show in figure 7 the derivatives of M_x^2 with respect to P_c and P_b for the 0° experiment, and also the derivatives with respect to θ_c and P_b in the Jacobean peak region (P_b is the beam momentum). It can be seen that the mass resolution for a Jacobean peak experiment with a 1 mr. standard error is equivalent to that for the 0° experiment with 3 mev/c momentum resolution. In figure 7 the missing mass is fixed at 1 gev; as the missing mass and beam momenta are increased, the resolution of the 0° experiment improves relative to the Jacobean peak experiment. Moreover, it can be seen from figure 7 that the beam energy resolution is critical in the Jacobean peak region but not at 0° .

Other considerations are, first, that triggering is easier for the 0° experiment, since the deuteron momentum ranges from 1400 to 1800 mev/c in the mass region around 1 gev; the corresponding momentum in the Jacobean peak region is from 2300 to 3000 mev/c, depending on beam momentum. (Deuteron identification depends on the smallness of v/c .) In terms of acceptance, both techniques are comparable. Thus, at 4.5 gev/c incident momentum, a 13% momentum bite in the 0° experiment gives a 200 mev mass range around 1 gev; the Jacobean peak method requires a 4° angular acceptance to achieve this. Concretely, one could perform the Jacobean peak experiment with two 10" wire chambers spaced 8' apart, one being next to the target; if the scattering in the target holder limits the angular resolution to 2 mr., then this would be equivalent in resolution to a 0° experiment with $dP/P = \pm .5\%$. A disadvantage of the Jacobean peak technique is that the large transverse momentum of the deuteron (400 to 600 mev/c here), should be accompanied by a rate reduction of 50 to 80%; this means that target empty background

must be virtually eliminated.

Spectrometer Resolution:

We optimize the accuracy of the momentum determination by using a mathematical representation of the magnetic field which is discussed in appendix 1. The measured coordinates are fitted to analytic expressions for the trajectories in both horizontal and vertical planes. The variation of the field with the transverse coordinates x and z is treated with a perturbative correction to the orbit parameters; these perturbations on the line integral vary by less than 2% over the aperture in the magnet which is accessible to the tracks. At any fixed spectrometer setting, the inclusion of field inhomogeneities improves the momentum resolution by only .2%. The reason for worrying about this detail is that the inhomogeneities vary systematically over the momentum spectrum; this is because of the strong correlation between momentum and position at the magnet entrance, caused by the upstream beam optics. When we piece together spectra taken at different spectrometer settings, the ultimate resolution depends on correctly calculating the inhomogeneities, since otherwise real physical fine structure will appear to occur at different momenta in different spectra.

The resolution is limited by multiple scattering in the chambers, digitization accuracy, and random energy loss in the hydrogen target. There are two experimental measures of the resolution: (1) the r. m. s. scatter of the chamber coordinates from the fitted trajectories, and (2) the width of the π^+ peak from the monoenergetic reaction $PP \rightarrow d\pi^+$. The pion energy is affected by the momentum spread in the primary beam ($\pm 4\%$), but this contributes only 5% to the width.

We estimate the various sources of error as follows:

- (1) $15/Pv \times .025$ is the rms. multiple scattering in the .01" of mylar around each chamber.
- (2) $15/Pv \times .098$ is the rms. in the .006" copper wires in the chambers; these are spaced 1 mm., so the probability of traversing one wire is 23%, while the probability of going through both horizontal and vertical wires is 1.5%.
- (3) $15/Pv \times .0022$ is the rms. scattering per inch of helium in the gas between the chambers (total path length is 500").
- (4) $.59 / (v/c)^3$ mev /c is the rms. momentum loss in the 3" hydrogen target, corresponding to a random energy loss of up to $.92/(v/c)^2$ mev.
- (5) .03" and .04" are the estimated digitization uncertainties in the horizontal and vertical planes respectively. The vertical sensor wire tends to oxidize because of the high voltage and gives poorer spatial resolution.

Because the deuterons have $v/c \approx .75$, multiple scattering overshadows the digitization uncertainty, which we take to be momentum independent (in fact, there is presumably some dependence on the number of ions and delta rays produced in the chambers and hence on v/c). Nuclear scattering in the chambers can be neglected. The most serious problem is multiple scattering in the wires; the distribution of multiple scattering angles in a single chamber is expected to be the sum of two gaussians - one having a total probability of 77% and a width of .4 mr. (at 1500 mev/c), the other having a probability of 23 % and width of 1.6 mr., caused by wire scattering. Thus, the physical errors are not gaussian, although in a practical fitting program for 2,000,000 events we must approximate them as gaussian.

Scattering in either the first or last chambers does not affect the resolution. In the central four chambers the distribution of single wire scatters is:

0 chambers- 35%
 1 chamber- 42%
 2 chambers- 19%
 3 chambers- 4%
 4 chambers- 0%

In addition, there is a 6% probability of at least one double wire scatter. Thus, a practical goal is to eliminate events with more than two wire scatters, and this can be done in an average sense by increasing the estimated multiple scattering in the mylar in each chamber to $Pv \times .035$ mr. Monte Carlo simulations show that by retaining only events with satisfactory confidence levels, we achieve a momentum resolution consistent with the revised estimate of multiple scattering. Obviously, we can improve the resolution even further at the expense of statistics by lowering the scattering angle parameter.

Knowing the multiple scattering angles, we deduce the digitization accuracy of the chambers by using the constraints implied by the orbit parametrization. Five parameters define an orbit- the momentum, P , the initial coordinates, X_0, Z_0 , and the initial slopes, $dX_0/dy, dZ_0/dy$; we fit these to their values at the spectrometer entrance, before multiple scattering occurs, although they can be equally well fitted at any point along the trajectory by redefining the error matrix. Thus, with six chambers there are three horizontal and four vertical constraint equations, and corresponding 'pull' quantities. Except for tiny fringe field effects, the pull quantities are simply the deviation from straightness of a line connecting the first three chamber coordinates, the corresponding deviation for the last three, and the difference between the extrapolated meeting point of these two

lines in the center of the magnet. The mathematical details are analyzed in appendix 2; it is shown that a simple linear transformation exists between the correlation matrix of the pull quantities and the 6X6 coordinate error matrix $\overline{dX_m dX_n}$; knowing the coulomb scattering contribution to the latter, we determine the chamber digitization accuracy, dX^2 , from the definition of $\overline{dX_m dX_n}$, specifically,

$$\overline{dX_i dX_j} = dX^2 + \theta_{he}^2 \sum_i L_i^2 (3L_j - L_i)/6 + \theta_{ch}^2 \sum_{k \neq j} (L_i - L_k)(L_j - L_k)$$

where θ_{he}^2 and θ_{ch}^2 are the rms. scattering angles per inch of helium and in each chamber, respectively.

Figure 12 shows pull quantity distributions, expressed in standard deviations, corresponding to digitization uncertainties of .03" horizontally and vertically; the latter is underestimated, as discussed above, and the vertical pulls have a broader distribution as a result. The momentum resolution is plotted in figure 8 (half-width), together with the resolution in the parameters X_0 and dX_0/dy ; we include in the momentum resolution the uncertainty due to energy loss in the target. The fitted momentum half-width of the pion peak at 3.8 gev/c is 9 mev/c; this compares reasonably well with the predicted value of 8.5 mev/c. The method of fitting the tracks and calculating resolutions is explained in appendix 2.

Figure 10 shows the confidence level distributions for events in which 4, 5, and 6 chambers were used in the fits. The salient feature of these distributions is the tail of events with confidence less than 5%. Part of the tail is expected to be due to scattering in the chamber wires as discussed above. Approximately 25% of the low confidence events are deuterons that go around the

middle chambers and suffer severe coulomb scattering in the helium bags and in the chamber frames. We check that the rest of the events are not associated with steep entrance angles in the chambers or with particular momenta (by comparing their time of flight distributions).

Some events are expected to have low confidence levels because of scattering in chambers 2 and 5 (recall that scattering in chambers 1 or 6 has no effect on the fits). These tracks fail to be collinear in the appropriate three chambers, and consequently, we throw away the outermost chamber coordinate whenever the corresponding pull quantity exceeds two standard deviations. Then a kinematic fit can be made using the remaining coordinates. Thus, the events that fail because of poor confidence level are mainly those that scatter widely in chambers 3 or 4; in this case there is no way to isolate the anomalous scattering and determine the momentum reliably. In practice, after fiducial cuts are made on the chamber coordinates, the failure rate is about 5%.

In the vertical plane, which is unimportant for the momentum analysis, we require only that the fitted orbit lie within .2" of the measured coordinates, on the average.

We use events in which fewer than six chamber coordinates are available- either because a pull quantity is anomalously large, as discussed above, or because of misses or reignitions or double tracks. Some doubles are recovered by employing the collinearity constraint, but this clearly cannot improve our knowledge of a track significantly, since collinearity must be assumed a priori. Thus, it is important to show that our fitting procedure is reliable for fewer than six coordinates. To test this we fit the 3.8 gev/c π peak events using only selected configurations of coordinates, and compare the resulting

spectra with the fits obtained using all six chambers. Examples are shown in figure 11 (the "¹³C" fits are obtained by the method already described- the resolution is optimized by rejecting coordinates associated with anomalous pull quantities). The low confidence level fits are also plotted. Our conclusion is that the resolution would be adequate if only three chambers (closest to the magnet) were used in the experiment. The use of six chambers enables us to weed out bad fits and to increase the recovery rate. Thus, 80% of the events have six good chamber coordinates in the horizontal plane, 18% have five or four, and 1% have only 3; the total recovery rate is 99%, before events are rejected on the basis of confidence level.

The primary beam energy resolution, as indicated in figure 7, is less important than the spectrometer resolution- the momentum resolution of ± 7 mev/c in the 'delta' region is equivalent to a spread of ± 30 mev/c in the proton momentum. As discussed above, the event triggering is gated according to the magnetic field in the Bevatron ring; the circulating beam momentum is required to lie in a $\pm .4\%$ band about the preset level. The spread in the ejected beam energy, for a fixed Bevatron magnetic field, is expected to be smaller than the above limit; this intrinsic spread is governed by the range of betatron oscillation amplitudes at the energy loss target. Assuming a 1" spread in these amplitudes, the corresponding momentum spread at extraction is $\sim 1''/600'' v_x^2$, or .1%. Thus, we take the beam resolution to be $\pm .4\%$ (24), (25)

The expected resolution in M^2 (half-width) is shown in figure 9, together with the fitted mass-squared widths of the π peaks at each beam energy. In the 'delta' region, the mass resolution is ± 4 , ± 6 , and ± 12 mev at 3.8, 4.5, and 6.3 gev/c respectively.

Spectrometer Calibration:

The pull quantities that determine the resolution also measure the accuracy of the chamber alignment. Originally, each chamber is located in the horizontal and vertical planes using two targets mounted on either side of the frame above the beam line. These are sighted to align with an axis connecting fixed telescopes on either end of the spectrometer with a rotating mirror mounted on the center of the spectrometer magnet. A mirror can also be mounted on each chamber to detect tilts about the axes transverse to the beam line by autocollimation. The misalignments that most affect the momentum determination are horizontal displacements of the chambers from the beam line.

There are intrinsically three undetermined errors: (1) an overall displacement of all six chambers from the beam line, (2) a rotation of the entire spectrometer about the vertical axis through the magnet center, and (3) a change in the bending angle between the axes defining each triplet of chambers. Only the latter can affect the momentum determination and will appear as an overall calibration error in dP/P .

Three errors can be determined; these can be taken to be the non-collinearity of each triplet of chambers, and also the displacement of one set of chambers relative to the other. As discussed in appendix 2, these errors cause the average values of the pull quantities to deviate from zero. We can correct the chamber locations in an unbiased way by adjusting them until the pulls average to zero, at the same time minimizing the average magnitude of these corrections. The required corrections are empirically less than $.01''$; after correcting the

alignment, we measure the apparent jitter in chamber alignment from run to run. The jitter in apparent chamber location for different runs is less than .003"; there is no evidence for time dependence in these location errors that might be caused by distant earthquakes or experimenters jarring the chamber stands. Thus, the momentum errors caused by chamber alignment jitter can be ignored; after 'realigning' the chambers as described above, we are left with a single uncertainty in dP/P common to all tracks which depends on the error in the estimated bending angle. On the basis of the observed magnitude of the alignment discrepancies, we take the overall calibration uncertainty to be $\pm .2\%$.

Additional calibration uncertainty due to inaccuracy in magnetic field measurements has been minimized; the spectrometer magnet is monitored with the same digital voltmeter used in the measurements, and the measurements themselves were repeated many times with the "Rapid Mapper,"⁽²⁶⁾ and with various calibration coils.

The calibration of the incident beam momentum is accomplished by measuring the correspondence between the beam energy gate setting and the Bevatron timing. The value of the Bevatron field is a known function of the time at discrete points in the timing ('I. P. L. P.' times). Knowing the radius of the energy loss target, and subtracting the energy loss, we determine the beam momenta to be 3855, 4515, and 6290 mev/c respectively.

The fitted masses of the π peaks are given in table 11. The differences $M_{\pi}^2 - .0196 \text{ gev}^2$ can be compared with equivalent errors in either the spectrometer calibration or in the beam energy calibration; in turn, we can predict systematic mass errors in the 'delta' region, attributing the pion mass error alternately to the spectrometer and to the beam calibration.

The projected delta mass errors are less than 4 mev in all cases. Thus, assuming no fortuitous cancellation occurs between a large spectrometer setting error and a large beam momentum error, we conclude that the mass calibration in the 'delta' region is within ± 4 mev.

Section IV- Acceptance, Detection Efficiency, and Beam Contamination

As discussed above, this experiment is well suited for studying fine structure in the mass spectrum, structure with characteristic width less than $25 \text{ mev}/c^2$. For this purpose, it is almost sufficient to look for narrow peaks in the raw target full momentum distributions. The spectra that overlap the 'delta' and 'rho' regions are shown in figures 14 through 19; no striking features are evident (with the possible exception of figure 18), aside from occasional statistical wiggles. The full width momentum resolution spans three to four bins in these plots. However, strong interaction effects with mass width greater than 40 mev would have to be produced copiously to show up in these individual spectra. In general, such effects are expected to produce shoulders or elevate the central peaks that are already present. For example the rho meson cannot be 'seen' in any of the plots (to avoid confusion, the peaks to the left of some of the spectra are not structure but background contamination.)

The common trapezoidal shape of all the distributions is a reflection of the acceptance characteristics of the system, which depend strongly on the 'relative momentum'; we define this by the quantity $dP = (P - P_0)/P_0$, where P_0 is the momentum for which the magnets are tuned. The dependence of the accepted production solid angle on this variable is shown in figure 13; the acceptance is trapezoidal, and falls off linearly on either side of $dP=0$. Other systematic biases contribute to the spectral shapes, including (1) losses from scattering in the spectrometer, (2) deuterons produced outside of the primary beam spot, (3) angular dependence of the production cross section, and (4) non-deuteron contamination as discussed in

section II. Our ability to unfold the momentum distributions accurately determines the significance that can be attached to any 'strong interaction effects'.

The transmission properties of the beam can be calculated theoretically only within reasonable limits; there are uncertainties in the magnet calibrations (about 1%), in the focusing properties of the magnet fringe fields, in the relative alignment of the beam elements, and in the properties of the primary beam at the target. A major advantage in digitizing the tracks with wire chambers, besides the improvement in momentum resolution, is the fact that the secondary beam itself provides a highly resolved description of the phase space that is transmitted by the system. It is important to note that the scintillators (C1-C2 in figure 1) degrade the directional information by introducing a 2 to 4 mr. coulomb scatter in the tracks. However, the high statistics available compensate for this.

Some additional information is available. First, the beam spot is monitored once during each run with a televised scintillator just downstream of the target. The observed position (.3" off the beam line) and size (.25"X.25") remain stable from run to run, with a few exceptions. Second, the magnet currents are monitored after each flattop; even though the calibration and focusing properties of each element are not known precisely, the effect of small field variations on the particle orbits can be calculated accurately.

The study of the transmission properties can be conveniently broken into two issues: the first task is to determine the acceptance of the beam from the target to the scintillators C1-C2; the second is to determine the efficiency with which the spectrom-

eter detects this phase space. The latter problem arises because multiple scattering in the counters throws a significant number of deuterons out of the wire chambers and out of the final scintillators C3-4-5. In the absence of multiple scattering, tracks produced by a pointlike source at the target must exhibit a unique direction at the spectrometer entrance, depending on their momentum and position. To predict the spectrometer efficiency reliably, we must know this expected direction to within .3 mr. for all incident momenta and coordinates.

Thus, we have an iterative problem: in order to pin down the optical properties of the beam from the incoming tracks, we must understand the biases introduced by escape losses in the spectrometer; but to calculate these losses, we have to know the optical properties very well. Fortunately, it is known that some portions of the incoming phase space (i. e., tracks in a small spatial and momentum bite) do not incur significant escape losses, and these rays can provide unbiased correlations with which to study the optical parameters.

We can write the transport equations (x_t, z_t) and slopes (ξ_t, λ_t) to the spectrometer entrance coordinates (x_s, z_s) and slopes (ξ_s, λ_s) as follows:

$$\begin{aligned} x_s &= A^x_t + B^x x_t + C^x dP ; \xi_s = a^x_t + b^x x_t + c^x dP + d_c^z \\ z_s &= A^z_t + B^z z_t + C^z dP ; \lambda_s = a^z_t + b^z z_t + c^z dP + d_c^z \end{aligned} \quad \text{IV-1}$$

and as a result,

$$\begin{aligned} \xi_s &= a^x/A^x x_s + (b^x - B^x a^x/A^x) + (c^x - C^x a^x/A^x) dP + d_c^x \\ \lambda_s &= a^z/A^z z_s + (b^z - B^z a^z/A^z) + (c^z - C^z a^z/A^z) dP + d_c^z \end{aligned} \quad \text{IV-2}$$

The terms d_c^x and d_c^z represent the coulomb scatter in the counters. The coefficients are functions of dP , and the terms

a^x, b^x , etc., are derivatives of A^x, B^x ... with respect to longitudinal distance along the beam. The terms $c^x dP$ and $c^z dP$ describe the horizontal and vertical steering introduced by the magnets; ideally the latter is negligible. Second order beam optics corrections, which arise from the dependence of the path length on the longitudinal direction in the equations of motion, are of order $(dx/ds)^2, (dz/ds)^2$, and are negligible owing to the small angular divergence of the beam. Thus, the equations IV-2 predict a linear relation between position and direction at the spectrometer entrance, which can be broken only by the presence of higher order harmonics in the quadrupole field, or by negligible second order corrections.

We measure the coefficients in IV-2 as functions of dP , using data from runs at all incident beam momenta; to avoid possible non-linearity in the calibration uncertainties, we rely on data taken from a 400 mev/c momentum band in the 'delta' region, thereby optimizing the description in the mass region of interest. The detailed parametrization of the coefficients and the interpretation of the measurements is left to appendix 3.

The results of this study are that, with a reasonable parametrization of the magnetic fields, we can predict observed correlations of positions, directions, and momenta in all the experiments with good accuracy. The directions of the incoming rays can be predicted within .3 mr.; this corresponds to knowing the target coordinates within .1", which is a reasonable limit of accuracy. Equally important, the magnification of the beam from the target to the spectrometer entrance is known to within 5%. Uncertainty in the magnification parameters leads to systematic magnification errors that are linear in dP ,

and consequent linear errors in our estimate of the production solid angle. Specifically, these uncertainties can be expressed as $\pm(.05 + .32 dP)$. Since the parameter dP is restricted to the range $-.045$ to $.085$ in the final analysis, there is as much as a 4% uncertainty in the relative magnification of high and low momentum rays in any given spectrum. However, this uncertainty is common to all the spectra and its effects on the unfolded cross-section can be studied systematically.

Next we analyze the acceptance of the beam up to the counters C1-2. The behaviour of the rays in the upstream beam elements is displayed in figure 20. We have straightened out the actual beam line so that particle orbits are relative to the ideal ray of momentum P_0 for which the magnets are tuned. The secondaries are bent 17° in the first magnet M1, and then pass through a 24" brass collimator, which limits the maximum solid angle to 16 msr. Further collimation is accomplished by the 8" diameter pipe through the quadrupole bore. The quadrupole doublet focuses the beam in both planes with a focal length that depends strongly on dP . At the counters C1-2 the maximum extent of the beam is 4" horizontally by 1.7" vertically. The momentum dependent angular dispersion caused by the M1 magnet is reversed in the M2 magnet and then reversed again in the M3 magnet. Depending on the steering and initial targeting, some collimation is done in the flanges between the quadrupole and the M2 magnet.

The acceptance function in figure 13, which gives the ratio of solid angle to maximum solid angle as a function of dP , is calculated assuming that the beam elements are compatibly tuned and that the beam is a point source at the target center. The computation uses the transport equations IV-1; the

acceptance is an integral over production angles of a step function which vanishes wherever one of the limiting apertures in the beam is exceeded. From this function, which we denote by Ω , we can derive to an excellent approximation the corresponding acceptance for arbitrary target location,

$$\Omega(x_t, z_t, dP) = (1 - z_t^2/2) \Omega(0, 0, dP - .04x_t) \quad \text{IV-3}$$

Thus, changing the horizontal target location is equivalent to changing the value of the central momentum P_0 . The dashed curve in figure 13 shows the averaged acceptance for a 1/2" beam spot not centered vertically.

This theoretical description is useful only as a guideline. However, to know the value of the central momentum, P_0 , which gives the center of the acceptance function, we need to know the target location and the magnet calibrations precisely. Unfortunately, by measuring the average steering of rays entering the spectrometer, we cannot distinguish calibration errors in M1 from those in M2. If we use an incorrectly centered acceptance function to unfold the momentum distributions, we will generate adjacent peaks and valleys in the neighborhood of P_0 . In addition, as shown in figure 13, the shape of the acceptance around P_0 depends on the beam spot distribution, which is not precisely known. Another problem arises even if the acceptance is known exactly; because of the finite momentum resolution, the peaks in the momentum distributions near P_0 are underestimated. Consequently, after dividing these spectra by the acceptance, we expect to generate dips around P_0 , about 3% in magnitude. This problem is analyzed in appendix 4.

The solution to these difficulties is shown in appendix 4 also. We define the acceptance by means of a limiting aperture

at the spectrometer entrance; the coordinates x_s, z_s are restricted to lie in a region inside the boundaries of the transmitted phase space. The size of this inner region is dictated by the momentum resolution and by the expected size of the primary beam spot. It can be chosen small enough so that the number of events lost from the aperture due to measurement error and targeting uncertainty is balanced by the number gained. The choice of boundaries for the aperture is made empirically, eliminating uncertainties due to calibration errors or target centering. Needless to say, this entire analysis would be completely trivial if the acceptance function were not so highly structured near $dP=0$. The unfortunate dependence on dP arises because the beam is deflected in M1 before it is collimated; in an experiment using a non-zero production angle, M1 could be eliminated and the acceptance made essentially flat.

Turning to actual data, we define coordinates related linearly to the production angles, ' x_c, z_c ', which give the entrance coordinates at the collimator; they are calculated from the transport equations assuming that the target is centered and pointlike and that the magnet calibrations are correct; for convenience, we normalize them to the collimator dimensions " x_c^{\max}, z_c^{\max} ", so as to lie between ± 5 . Figure 30 shows x_c/x_c^{\max} and z_c/z_c^{\max} plotted against dP . On the basis of such plots, examined in detail run by run, we define fiducial cuts on x_c and z_c ; these cuts define the production solid angle. We note that the x_c distribution is centered beyond $x_c=0$; this is consistent with the inference from the horizontal steering measurements (discussed in appendix 3) that the primary beam is targeted to the left of center ($x_t = -.4''$). The z_c distribution is low and narrower than expected (the full width

should be about 1 unit on the plots). This is apparently related to the fact that the beam enters the spectrometer .5" low and steered downwards; this may be explained by a combination of circumstances- collimator misalignment, high vertical targeting, and vertical steering in the beam elements caused by misalignment. Any of these effects can reduce the vertical acceptance by the amount indicated in figure 30. As discussed in appendix 3, it would be inconsistent with the angular correlation measurements (between z_s and θ_s) to attribute these effects to magnification error.

Next we consider the spectrometer detection efficiency. Typically 40 to 60% of the events survive the phase space cuts described above; the remainder are subjected to restrictions on the chamber coordinates- the radial distance from the beam line to the spark must be less than 4.5", which is the radius of the helium bags between the chambers. The rear scintillation counters are large enough (9"X9") to detect all rays that survive this cut. Figure 21 shows the passage of high and low momentum rays through the spectrometer, with the coulomb scattering in C1-2 turned off. At the entrance the incident beam has an angular dispersion of 18 mr. over a 10% momentum bite (given by the coefficient of dP in IV-2). Although this dispersion is canceled by M3, the images of the high and low momentum components are separated by 4" horizontally at the last spark chamber. The scattering in C1-2 causes these images to have a 3" to 5" spatial extent, so that off momentum components suffer escape losses in the last three chambers. These losses are especially sensitive to the M2 magnet tuning- a 1% tuning

error displaces the beam by 1" in chamber 6.

The resulting detection efficiency is defined as an integral over coulomb scattering angles:

$$W^{-1}(dP) = \frac{\int \int dx_s dz_s d^2\delta_c F(\delta, \delta_c^2) \prod_{i=1}^3 D(R_{\max} - R_i(\delta, x_s, z_s))}{\int \int dx_s dz_s} \quad \text{IV-4}$$

Here $D(x)=1$ for $x > 0$, 0 for $x < 0$; $R_{\max}=4.5''$; $F(\delta, \delta_c^2)$ is the coulomb scattering distribution with r. m. s scattering angle δ_c^2 .

Systematic errors in the efficiency function are caused by errors in δ_c^2 , and by incorrect calculation of the expected chamber radial coordinates R_i , which depend on the predicted correlation of track direction with entrance coordinates and dP . As stated above, these directions are calculable within .3 mr. The differences between measured chamber coordinates and predicted coordinates are plotted in figure 29. These distributions are centered within .1" and their width is governed by the multiple scattering in C1-2.

We measure the r. m. s multiple scattering angle as a function of momentum using central rays ($dP \sim 0$) from all the experimental data. The raw results, which fall as $1/Pv$, are plotted in figure 327. Taking into account the finite momentum resolution (which introduces error in the predicted track directions through IV-2) and also the angular acceptance of the spectrometer, we find that the data follows the curve $2.50/Pv$ to within .1 mr. accuracy. This measurement is within .1 mr. of the value calculated using the known H/C ratio and mass of the scintillator⁽³⁷⁾.

In figure 26 we plot the systematic error in the weight, W ,

as a function of the weight; the curves are calculated for different errors in the expected track directions and in δ_c^2 , expressed in units of δ_c . Since W^{-1} is essentially the integral of a gaussian (the multiple scattering distribution), its error depends on the linear sum of the errors in central position and width ($\pm .1$ and $\pm .03$ standard deviations of the scattering distribution respectively). Thus, according to figure 26, if we eliminate data with calculated weight greater than 1.20, the maximum systematic error is between +8% and -6% (the upper and lower curves in figure 26 are for parameter errors that cause an underestimate or an overestimate of the weight, respectively). Using the error curves, we can compute the effect on the averaged cross section caused by a systematic weighting error in each run.

In addition to the fiducial cuts made on the chamber coordinates at the spectrometer entrance and in the spark chambers, we eliminate from the spectra events in the tail of the confidence level distribution, about 6% of the remaining sample. We test that these events do not have any momentum bias by studying their time of flight distribution.

The acceptance and efficiency calculations described so far make sense so long as the beam spot is less than .5"X.5" in size. The larger the beam spot, the more the overall solid angle acceptance is reduced; the phase space plots in figure 30 become increasingly depleted at the edges, and stricter fiducial cuts are necessary on the acceptance aperture in x_c, z_c space. In practice there are sources of deuterons that cannot be associated with a small beam spot and must be eliminated

from the data.

Referring again to the raw momentum spectra of figures 14 through 19, we notice a conspicuous peak of low momentum events in each distribution. Initial studies of the secondary beam showed that this low momentum tail dominates the distributions when the hydrogen target is completely removed from the beam. Furthermore, these rays enter the spectrometer with anomalously positive slopes - typically 15 mr. greater than expected. Looking upstream at the target, these secondaries appear to originate 5" to the left of the primary beam (in the direction of the top of the drawing in figure 1). They are apparently associated with interactions of the primary proton beam in the materials near the collimator, probably in the adjacent shielding and in the uranium backstop. The primary beam is too energetic to be deflected directly into the collimator material. In any case, these events are easily removed by requiring that the incoming direction not exceed the expected direction by more than 3 times the r. m. s multiple scattering angle.

Figure 31 shows the profile of the beam emerging from the quadrupole and from the M2 magnet entrance and exit. The relevance of these plots is that the beam is confined within the metal flanges at each of these ports (8" diameter at the quad, 4" vertically at M2), and any contamination of the beam must originate upstream of the quadrupole.

Figure 32 shows plots of the horizontal slope deviation versus the collimator entrance parameter x_c/x_c^{\max} . We emphasize that x_c is calculated as a unique function of dP and x_s by taking the target coordinate x_t to be zero. If the target coordinate shifts, then x_c does not correspond to the true collimator entrance coordinate; similarly, the expected entrance angle shifts by -3 mr. for a 1" shift in x_t . Ignoring the

spread in slope deviation caused by multiple scattering, it happens that the events which lie on a 45° axis in figure 32 have actually passed through the collimator center, having originated in a different target location.

The plots show three distinct clusters of events. The group in the center of each plot corresponds to acceptable events-rays that originate at the target center and have a slope distribution centered on the expected value. Near the top of each plot is the group of low momentum events discussed above; being far from the 45° axis, they cannot have passed through the collimator center. A third cluster of points has an average slope deviation of -7 mr. and abnormally negative x_c . The target origin is apparently displaced $1.5''$ to the right for these events. We conjecture that these rays are associated with a halo in the primary beam that interacts in the hydrogen and in the target walls- these anomalous events are, in fact, relatively more abundant in target empty runs. The effect is almost absent in the lower plot (4.5 gev/c -1); the upper plot, from 4.5 gev/c -2 , represents data taken while part of the external proton beam was used by the $25''$ bubble chamber. During this running, beam loss from the second to the third E P B foci was reportedly severe, and also, in some runs, the beam spot as observed in the target scintillator was as large as $1/2''$. In the second half of these 4.5 gev/c runs, the primary beam tuning was improved; this resulted in a marked reduction in the number of anomalous rays.

This contamination represents a serious problem. We know from equation IV-3 that if the target coordinate is shifted by $1.5''$, the acceptance function peaks at $dP = -.06$

rather than at $dP=0$. The maximum value of the acceptance depends on the vertical target distribution, which is probably fairly diffuse for rays produced in the beam halo (the vertical slope deviation distribution for these rays is, in fact, anomalously broad). In any case, these rays are expected to add a peak to each momentum distribution at $dP = -.06$. In figure 34, to confirm this prediction, we show the dP distributions for both the 'normal' and the 'anomalous' rays in this 4.5 gev/c data. These look essentially like the acceptance functions of figure 13, with the anomalous data shifted to $dP = -.06$ as expected.

Most of this contamination can be removed by imposing cuts on the horizontal slope deviation (not less than $-2\delta_c$), and on the collimator coordinate x_c (greater than $-.25 x_c^{\max}$). The latter cut is dictated by the fact that rays from the target wall ($x_t < 1.5''$) have non-vanishing acceptance in the band $-1.25 < x_c/x_c^{\max} < -.25$. Another way to visualize this procedure is as follows: the acceptance parallelogram (dP versus x_c) of figure 30 is tied to the 45° axis and drops by .5 units for each inch of target displacement; the cut on x_c makes the parallelogram for the 'normal' rays disjoint from that for the 'anomalous' rays. The cut in slope deviation is designed to eliminate to some extent rays that have re-scattered in transit, and also to reduce the overlap of events not produced at the target center (the beam halo may also create deuterons in the hydrogen).

It would be incorrect to rely on the subtraction of target empty cross sections to eliminate deuterons produced in the target walls. In the first place, the characteristics of the beam are not sufficiently stable from run to run to permit

a comparison of target full and target empty contamination. Secondly, errors in the subtraction procedure would produce enhancements in the low momentum part of each subtracted spectrum. In fact, it was precisely the observation of such an effect that led to this analysis. The reason for expecting subtraction errors is that the production of secondaries by the halo also perturbs the normalization of each run; the beam monitor counters do not differentiate 'good' secondaries from halo-initiated secondaries. However, we expect that the ratio of the number of 'normal' to 'anomalous' deuterons is proportional to the ratio of protons in the beam halo to protons in the central beam spot; the proportionality constant is given by the maximum solid angle acceptance for 'anomalous' rays.

These considerations are confirmed by studying the unfolded target empty cross-sections in experiment 4.5-2, where the halo effects are worst. Depending on the number of anomalous deuterons rejected, we observe systematic reductions in the target empty normalizations; the size of these reductions can be inferred from continuity. In figure 33 we plot the relative number of 'anomalous' deuterons versus the normalization errors. The data points are expected to follow a line

$$\frac{\text{true cross section}}{\text{measured cross-section}} = 1 + k^{-1} \frac{\text{'anomalous deuterons'}}{\text{'normal' deuterons}}$$

and k , the maximum acceptance for 'anomalous' deuterons turns out to be .5. Similar, though smaller, errors are observed in the target full cross-sections, and these are corrected by requiring continuity. The target full corrections are small because the beam monitor rates appear to depend

mainly on the number of hydrogen interactions, judging by the increase in the M1-2 counting rates when the target is full.

Thus, a consistent picture of the secondary beam contamination can be drawn, which accounts for observed anomalies both in the rates and in the spectral shapes. For the bulk of the data, the 'anomalous' deuteron rate is less than 10%; in a few runs where this rate fluctuates excessively, the normalizations are observed to be inconsistent, and the data is rejected. We may expect a systematic 10% uncertainty in the overall target empty normalization from this effect; however, this cannot affect the fine structure in the subtracted spectra.

One systematic correction to the individual spectra remains to be analyzed, namely the physical dependence of the cross section on production angle; assuming an $e^{-P_{\perp}/A}$ behaviour, we estimate that the production rates vary linearly with dP over the accepted momentum range by as much as 10% (taking $A = 300 \text{ mev}/c$)⁽³⁴⁾. The production angle is approximately

$$\Omega_{\text{prod}} = 13.5 x_c/x_c^{\text{max}} + 116 dP + 5 \quad (\text{mr.})$$

Of course, cross section variations over this range of production angles (-3 to +19 mr. in the accepted dP range) are not known. Figure 36 shows a distribution of x_c/x_c^{max} for rays with $dP \sim 0$; over the corresponding angular range of -1 to +12 mr. the number density falls by 2 to 5%. Since the effects of this correction are numerically indistinguishable from the linear magnification uncertainty discussed above, in the actual analysis we ignore the correction.

Section V - Normalization

The beam flux is monitored with the scintillators M1-M2 shown in figure 1; these record typically 300 secondaries per 10^{10} protons with target full, and 60 with target empty. To obtain the relative calibration between target full and empty, the proton beam was focused on a 3" diameter secondary emission monitor 8' downstream from the target; counting rates with target full and target empty were compared with the S. E. M. voltage. To check the calibration of the S. E. M., which is known to within 15%⁽²⁷⁾, or equivalently, the exact calibration of the target full monitor, the monitor counts were compared with a polyethylene foil activation. The proton beam was focused on a thin (4 mg./cm²) foil and the calibration was accomplished with the reaction $C^{12}(p, pn)C^{11}$, which has a known cross-section. The C^{11} beta decays to B^{11} in 20.5 minutes, and the foil activity thus measures the incoming beam intensity. This measurement agrees within 10% with the nominal S. E. M. calibration; the principal source of error seems to lie in the dependence of the M1-2 counting rates on the beam focusing, as discussed above. The systematic normalization error is estimated at $\pm 10\%$ (mainly from uncertainties in the nuclear reaction cross-section).

The differential cross-section can now be defined as

$$d^2\sigma/dP_d = d^2N/dP_d d\Omega \cdot N_t/N_d \cdot 1/L_p^h \cdot 1/N_p \cdot F \quad V-1$$

where $d^2N/dP_d d\Omega$ is the differential deuteron production rate including detection efficiency corrections, measured by unfolding each spectrum; N_t/N_d is the ratio of the number of deuterons detected to the number of spark chamber triggers; $1/L_p^h$

is the reciprocal of the number of target protons per unit area, or 3.1 barns per target proton ($L=3''$, $\rho_h = .07 \text{ gm./cm}^3$. $6 \cdot 10^{23}$ atoms/mole); N_p is the number of beam protons as determined by the monitor counters; finally F denotes all additional corrections to the normalization.

The following effects are lumped in F :

- (1) Attenuation of the primary and secondary beams (3%)
- (2) Dead time corrections caused by the 50 nsec. cerenkov gate (1-5%)
- (3) Production of deuterons by secondaries in C1-C2 (negligible).
- (4) Rejection of deuterons by formation of knock-on electrons in the cerenkov water (from 2% at 1100 mev/c to 40% at 2000 mev/c). This correction must take account of the logic used in experiments 3.8 gev-1 and 4.5 gev-1, where the cerenkov veto is correlated with the time of flight, as discussed in section II, and also where wave shifter is used in the cerenkov water to improve the light collection efficiency.
- (5) Accidentals in experiments 3.8 gev-1 and 4.5 gev-1 that are not removed by the time of flight requirement (5-10%).

The last two corrections are momentum dependent, besides being large in magnitude. The first three affect only the absolute cross-section calibration. We stress that none of these effects can introduce fine structure into the cross-sections.

Attenuation of the Primary and Secondary Beams:

The average proton flux at the center of the target is reduced from the upstream intensity by a factor

$$1 - N(\text{center})/N(\text{upstream}) = \sigma_{pp} \cdot N \cdot (L_t/2\rho_h + L_w \rho_w A_w^{-1/3})$$

where σ_{pp} is the total PP cross section (40 mb.),

$N = 6 \cdot 10^{23}$, L_t and L_w are the thicknesses of the hydrogen (3") and the target walls (.017"), p_h and p_w are the corresponding densities, and A_w is the mean atomic number of the wall material (12). Numerically the relative beam loss is 1.6%. Since the beam monitors were calibrated by determining the beam flux in polyethylene foil placed upstream from the target, we must correct this normalization by the factor above. For target empty situations, the attenuation is .4%.

The secondary beam is itself attenuated by nuclear interactions in the hydrogen and in the target walls, in the thin windows which hold vacuum in the beam system, and in the counters C1-C2 and in the spectrometer as far as the center of the analyzer magnet. We anticipate that most of the nuclear losses result in stripping of the deuterons; if stripping occurs after the spectrometer magnet, the resulting proton will be detected as a deuteron, since it will have the correct velocity. Stripping upstream of this magnet will produce protons that are too low in momentum to lie in the accepted portion of the momentum spectrum. Taking the total deuteron scattering cross section to be 60 mb. per target nucleon, we estimate an attenuation of 3.1%, most of which occurs in the counters C1-C2.

Dead Time Corrections:

The incident flux at counters C1-C2 is 30,000 particles over a 200-500 msec. spill, or one particle every 10 microsec. on the average (ignoring the Bevatron duty factor). Since the cerenkov veto gates the electronics for 50 nsec., we expect a dead time

correction on the order of 1%, depending on the duty factor. To obtain an empirical estimate, we compare the following coincidence rates: (1) C3C4C5 and (2) C3C4C5 \bar{C} , where \bar{C} is delayed by more than half the gate width. This measures the probability that a C3C4C5 coincidence will be vetoed by a previous cerenkov signal. The delay is chosen to be 30 nsec., small enough so that structure associated with the 300 nsec. Bevatron period of revolution does not give rise to systematic error. Dead time corrections for the scintillation counters can also be ignored; if two particles, a proton and a deuteron, arrive at C3C4 simultaneously (within a few nsec.) the cerenkov veto will eliminate the event whether or not the photomultiplier output pulses are distinct. Accidentals involving simultaneous deuteron events can be neglected because of the low flux.

Production of Deuterons by Secondaries:

We estimated above that 1.6% of the incident beam is involved in collisions in the upstream target wall and in the first 1.5" of hydrogen; secondaries produced in these reactions can themselves create deuterons in the remaining hydrogen and in the downstream target wall. Thus, the attenuation calculated above is an overestimate; elastic PP collisions will not attenuate the beam available for deuteron production; inelastic PP collisions that create a pair of slow nucleons will in general enhance the probability of creating a deuteron (as compared with the chances that the original fast proton would have made a deuteron). In any case, the normalization corrections involved are smaller than the systematic calibration uncertainty. The momentum distribution

of these tertiary deuterons is governed by the acceptance function and cannot introduce spurious fine structure.

Deuterons can be created in C1-C2 by secondary protons, but the flux is too low to produce an appreciable effect. We expect the dominant mechanism to be the reaction $P N \rightarrow d \pi^+$, where N is any nucleon in the scintillator; at incident proton momenta of 1200 mev/c, the differential cross-section for this reaction is 500 microbarns/ sr. ⁽²⁹⁾, 20-50 times larger than the cross-sections at the primary proton energies under study. Moreover, the solid angle acceptance for deuterons produced in the scintillators is larger than the maximum solid angle for production at the target. It turns out that the momentum distribution of these deuterons places them outside of the time of flight gate, except for a 5-10% tail caused by the Fermi momentum of the target nucleons. As a result, about 1 in 10^4 deuterons is expected to be produced in the scintillators by this process.

Rejection of Deuterons by the Cerenkov Detector.

The rejection of deuterons by formation of knock-on electrons in the cerenkov water is analyzed in appendix 5. The rate can be calculated analytically as a function of momentum and depends only on the overall light collection efficiency of the detector; specifically, if N photons are produced in the water, then the number of photoelectrons, N_e , created in the six tubes in the detector is distributed as $P(N_e) = (E \cdot N)^{N_e} \cdot e^{-E \cdot N} / N_e!$ where E is the efficiency. The rejection probabilities for different efficiencies are plotted as functions of momentum in figure 6, together with the corresponding rejection probabilities for protons. The deuteron losses are determined

empirically by comparing time of flight spectra in which a cerenkov count is required with spectra in which all secondaries are recorded; the measurements are shown in figure 6.

In experiments 3.8 gev-1 and 4.5 gev-1, wave shifter was used in the cerenkov water to improve the light collection efficiency (this converts the high frequency radiation to the visible region, around 4000 \AA , where the R C A- 8575 tubes are most sensitive.) This was removed when it became apparent that 45% of the high momentum deuterons (above 1900 mev/c) were being rejected. At first it was guessed that the wave shifter was acting as a scintillator; however, the observed rejection rate increased rapidly with momentum rather than falling as $1/v^2$. To account for this observed loss of high momentum deuterons, the cerenkov efficiency for this data must be around 2.3%, according to figure 6. The effect is dramatized by the unfortunate logic used in this data, as discussed in section II, the cerenkov veto does not become fully effective until the deuteron momentum exceeds 1660 mev/c. (Recall that the gate reaches C1-C2 in time to reject protons and pi ons but too late to reject slow deuterons.) We let $C(P_d, E)$ denote the probability that a deuteron will not trigger the cerenkov counter; then for this early data with the veto applied to C1-C2, the deuteron flux must be corrected by the function

$$W(P_d, E) = 1 / (F + C(P_d, E) \cdot (1-F)), \text{ where } V-2$$

$$F = \int_{-\infty}^{t_d} dt e^{-(t-t_c)^2 / 2\gamma^2} / (2\pi)^{1/2} \gamma \text{ is the probability}$$

that the deuteron time of flight, t_d , will precede the onset of the cerenkov veto, t_c ; γ is the combined jitter in the cerenkov and

scintillation timing (from 1.5 to 2.5 nsec.). For later data taken with the cerenkov veto applied to C3C4C5, the appropriate weighting correction is just

$$W'(P_d, E') = 1 / C(P_d, E')$$

The function $1/W(P_d, E)$ is plotted in figure 35-a, assuming $E=2.25\%$, $\gamma=2.4$ nsec.

We emphasize that the resulting corrections are smooth functions of momentum that cannot introduce fine structure in the mass spectrum. Inevitably, there are uncertainties in the normalization and overall shape of the first experiments at 3.8 and 4.5 gev/c, since the parameters t_c , E , and γ are not precisely known, but must be determined by comparison with later data.

Accidentals in the early Data:

As discussed in section II, deuteron events must not only lie in the 14 nsec. timing gate but must also exhibit the correct correlation of time of flight with momentum (within ± 4 nsec.). Accidentals with momentum greater than 1660 mev/c are well separated from the deuterons because the cerenkov veto completely overlaps the deuteron band, as shown in figure 5; accidentals must exhibit a long time of flight that lies outside the cerenkov anticoincidence gate. Below 1660 mev/c some accidentals can lie inside the deuteron band; denoting the accidental flux by $R(P)$ - a function proportional to the total secondary flux (essentially a constant in P after unfolding the acceptance)- the number of accidentals, $N_a(P)$ that survive the time of flight criteria is given by

$$N_a(P) = \int_{t_d-4}^{t_d+4} dt' \int_{-\infty}^{t'} dt'' \frac{e^{-(t''-t_c)^2/d\gamma^2}}{(2\pi)^{1/2}\gamma} \cdot R(P) \quad \text{V-3}$$

Here, t_d is the deuteron time associated with momentum P , t_c is the arrival time of the cerenkov veto, and γ is the timing jitter, as above. $N_a(P)$ is a smooth function of momentum and is plotted in figure 35b, again assuming that $\gamma = 2.4$ nsec. The above expression simply counts the number of events in the allowed time interval (flight time = $t_d \pm 4$ nsec.) that miss the cerenkov veto, which arrives at t_c ; the range of t_d is limited by the momentum acceptance, and as a result, the band $t_d \pm 4$ nsec. always lies inside the original 14 nsec. gate.

The functions V-2 and V-3 can be well approximated by quadratic and cubic functions of the momentum respectively over the range 1470 to 1800 mev/c, provided that γ is greater than 1.5 nsec., which is in fact the observed time resolution of the scintillators. If γ were very small, we would observe a discontinuity in the cross-section at the deuteron momentum corresponding to t_c - beyond this momentum accidentals would be well separated from deuterons, and the deuteron flux would suddenly drop because of the rejection caused by knock-on electrons in the cerenkov counter. Empirically, there is no discontinuity in these momentum distributions. Consequently, after applying correction V-2 for the cerenkov rejection, using the above values of E , γ , and t_c , we subtract a fitted cubic in the momentum from this data to achieve agreement with the later data; this procedure is discussed in section VI.

Section VI- Final Data Averaging

The next problem is to determine the average hydrogen cross-sections without introducing spurious discontinuities due to the discrete character of the data runs. To subtract the non-hydrogen background, we fit the target empty data to a quadratic in the deuteron momentum so as to eliminate needless additional statistical errors. Physically, we expect the non-hydrogen cross-sections to be structureless; deuterons produced in reactions like $(P, C^{12}) \rightarrow (dC^{11})$ lie outside of our momentum range, and deuterons formed by meson production collisions with single nucleons have a wide momentum spread from the Fermi motion. The results for the six experiments are shown in figures 37-42, where we plot the corresponding center of mass background differential cross-sections $d^2\sigma/dM^2d\Omega$ to facilitate comparison with the hydrogen cross-sections; as a function of momentum, the laboratory background differential cross-section $d^2\sigma/dPd\Omega$ is essentially flat.

An overlap chisquare is defined for the subtracted data to test the mutual agreement of the runs in each experiment:

$$X^2 = \sum_{\text{runs } P_i} \frac{(\sigma(P_i) - \sigma_i')^2}{\gamma_n^2(P_i)}, \text{ where } \gamma_n \text{ is the statistical}$$

error and σ_i' are the free parameters that define the average cross-section in momentum bin "i". There can be overall normalization errors in each run; these normalizations are statistically accurate within 1-2%, but systematic errors may arise in the dead time corrections or in the beam normalizations, for example. Rather than introduce discontinuities in the

cross-section wherever a run begins or ends, we renormalize each run so as to minimize the overlap X^2 . The calculated corrections are generally 1-3% in magnitude, and do not alter the structural details of the cross-sections significantly. Also, to reduce the effects of other systematic errors that could lead to slight discontinuities from run to run, we overestimate the errors near the edges of the runs; specifically, the error bars are systematically increased by a factor $(1 + \exp(dP - dP^- / .015) + \exp(dP - dP^+ / .015))$, where dP^- , dP^+ define the momentum range of each spectrum and are taken to be -.045 and .085 respectively to give a 13% momentum bite. The resulting error bars in the average cross-section are not significantly increased; the purpose is to ensure smoothness in the transition from one run to the next by damping the statistical weights of the outermost data points. The overlap X^2 's for the six experiments are listed in table 9, and are within statistical expectations.

As a further test to see whether disagreements between runs are random or systematic, we measure for each run the point to point deviation from the average values obtained from all the neighboring runs. Thus, tables 3a-8a show the differences, expressed in units of .1 s. d., between each single run and its neighbors; the comparison is broken into 10 mev/c momentum bins, and each column corresponds to a single run. No gross systematic structure is discernible in these residuals. In addition, in tables 3b-8b, we list the C. M. differential cross-sections together with mean square deviations of the individual runs from their averages, for each 10 mev/c momentum bin. Confidence levels are given for

each point. The contributions to the overlap X^2 do not cluster in any particular momentum region.

Figures 43-48 show the laboratory cross-sections for each experiment; the individual run cross-sections are superposed using different symbols to illustrate the overall run to run consistency.

Because of the uncertainties in accidental rates and in cerenkov efficiency and timing, we expect to see systematic differences between the early data at 3.8 and 4.5 gev/c and the later data. Since these differences are 'smooth' as discussed in section V, we can fit the experimental differences satisfactorily with a cubic function of momentum over the range 1470 to 1800 mev/c. These functions are plotted in figure 49; they are too smooth to alter the fine structure in the early data and in magnitude they are typically 4-8% of the original cross-sections. At 6.3 gev/c there is some systematic difference between the two experiments; most of this discrepancy can be associated with the target empty cross-sections, which are higher in 6.3 gev-1 (see figures 41, 42). Unfortunately, the hydrogen cross-section is only 30-50% of the background rate in the mass region below 1 gev, so that small errors in target empty normalizations have a serious effect on the subtracted cross-sections. We use the same procedure for this 6.3 gev/c data as for the other energies: we assume that the target empty data of 6.3 gev-2, which is very limited statistically (one run in the low mass region) is somehow incorrectly normalized. Again, the fitted difference between these experiments is smooth in momentum. Figures 50-52 show the C.M. differential cross-sections for the three pairs of experiments superposed (after the systematic correction

has been made).

Systematic errors in the magnification and detection efficiency calculations have been discussed above. To test their effects, we analyze the data using the upper and lower bounds on the magnification parameters, by introducing the systematic linear correction factor $\pm(.05+.32dP)$ to each spectrum. No difference in either the fine structure or in the overlap X^2 can be introduced in this way; this can be seen by comparing figure 56 with figure 54- these show the differential cross-sections at 4.5 gev/c with and without the systematic correction. Similar results are obtained from varying the detection efficiency calculation by systematically shifting the average incident direction of the secondaries (as a function of dP and X_s) and the r. m. s. scattering angle. The averaged effect on the differential cross-section is 5 to 10 times smaller than the statistical uncertainties (assuming 20% uncertainties in the directions and rms. scattering angles); this is partly because the errors tend to cancel when the overlapping runs are averaged, and partly because the systematic errors are small to begin with- especially since the portions of the spectra with the largest detection efficiency corrections are weighted least heavily due to the systematic increase in the error bars described above.

Section VII- Fitted Cross-Sections

The averaged C.M. differential cross-sections for each energy are shown in figures 53-55. The data is initially organized in 5 mev/c momentum bins, and the figures display both coarse and fine binning. Figures 57-59 present the same spectra with fitted curves; the bin widths are 20 mev/c (in momentum) at 3.8 gev/c, 10 mev/c at 4.5 gev/c ($M^2 < 1.3 \text{ gev}^2$), and 10 mev/c at 6.3 gev/c ($M^2 < 1.6 \text{ gev}^2$). In the ' δ ' region, the corresponding mass bins are 10 mev at 3.8 and 4.5 gev/c, and 18 mev at 6.3 gev/c. Figure 60 shows the laboratory cross-sections. Noting that the laboratory differential cross-section $d^2\sigma/dPd\Omega$ is roughly linear beyond the ρ meson region, we display differences between the actual data and a linear fit in figure 61; the fit is confined to the M^2 region between .75 and 1.25 gev^2 , and to maximize the statistics, we average the results from the three energies. If structure in the cross-section is uncorrelated with the missing mass (i. e., if it is due to statistical or systematic effects), we would expect it to wash out in this averaging process; instead, we see a peak at .95 gev^2 on top of a flat background.

The most prominent feature at each energy is the reaction $PP \rightarrow d\pi^+$. Production of the ρ^+ meson is evident at 3.8 and 4.5 gev/c; the signal at 6.3 gev/c suffers from the large target empty cross-section (3 times the hydrogen rate at M^2), and also from the paucity of data in this region (1 run). The unfavorable target empty rates made it advisable to concentrate on the mass region of greatest interest at 6.3 gev/c.

Neither the A1 (1.14 gev^2) nor the A2 (1.6-1.7 gev^2) are prominent; kinematically, the A2 should be visible at 6.3 gev/c , and the A1 at 4.5 and 6.3 gev/c . At 4.5 and 6.3 gev/c there is evidence for structure in the ' δ ' region; 3.8 gev/c is essentially featureless here.

We fit the data to an incoherent sum of π^+ , ρ^+ , and δ^+ production superposed on a smooth background; the exact expression used is the following:

$$d^2\sigma/dM^2 d\Omega = \sigma_{\pi} \frac{e^{-(s-s_{\pi})^2/2\gamma_{\pi}^2}}{(2\pi)^{1/2}\gamma_{\pi}} + \frac{\sigma_{\rho} \gamma_{\rho}(s)}{\pi((s-s_{\rho})^2 + \gamma_{\rho}^2)} + \frac{\sigma_{\delta} \gamma_{\delta}}{\pi((s-s_{\delta})^2 + \gamma_{\delta}^2)} + \sum_1^7 A_n s^{n-1} \quad \text{VII-1}$$

where $\gamma_{\rho}(s) = (q(s)/q(s_p))^3 \cdot 2q^2(s_p) \cdot \gamma / (q^2(s) + q^2(s_p))$

The fit is done iteratively; the resulting curve and also the background polynomial are drawn in figures 57-59. The fit parameters and errors are listed in table 10. The errors on the ρ^+ cross-section come principally from the uncertainty in the polynomial background. The errors on the δ^+ cross-section and width are strongly correlated with the background shape.

Before analyzing these errors, we note that conventionally the background would be fitted to a phase space expression, given by a sum over two and three particle channels, i. e.

$$d^2\sigma/dM^2 d\Omega = 1/4s \cdot q_d/q_p \cdot \sum_{i=\text{channels}} |T_i|^2 \cdot \prod_k d^3p_k/2E_k \quad \text{VII-2}$$

where the phase space factors include the recoiling meson system with fixed M^2 ; for two and three-particle systems these are:

$$\prod_1^2 d^3 p_k / 2E_k = q(M^2) d\Omega / 4M$$

$$\prod_1^3 d^3 p_k / 2E_k = q_{12} q_{12,3} dM_{12} d\Omega_{12} d\Omega_{12,3} / 8M$$

The coefficients relating the $1T_{i1}^2$ matrix elements to $d^2\sigma/dM^2 d\Omega_d$ are plotted as functions of M^2 in figure 66.

The non-resonant background given by the polynomial fit cannot be successfully represented by a sum of phase space terms; the fit X^2 's are twice the number of degrees of freedom in every case. Including only the 2π and 3π contributions, we find that the corresponding matrix elements $1T_{i1}$ both fall with energy as $(s)^{-1.4}$, approximately. The corresponding matrix element for single pion production falls as s^{-1} approximately (the C. M. cross-section $d\sigma_\pi/d\Omega_\pi$ falls as $s^{-2.6}$). (3), (29)

Since we are forced to use a polynomial in M^2 to describe the background adequately, there is systematic uncertainty in fitting the δ parameters. Since the signal is clearest at 4.5 gev/c, we determine the resonance mass ($M^2 = .952 \pm .012$ gev²) from this data. Then, fitting to a Breit-Wigner expression plus background polynomial over the range $.75 \leq M^2 \leq 1.4$ gev², we study the variation of X^2 with σ_δ and γ_δ . In general, if we fit an expression by fixing one parameter and varying the rest, then the difference $X^2 - X_{\min}^2$ is distributed according to one degree of freedom as the fixed parameter is set to different values. It is obvious that with more variable parameters in the fit, X^2 must rise more slowly away from X_{\min}^2 ; the number of variable parameters is therefore dictated by seeing whether additional terms improve X_{\min}^2 by more than one unit.

In figure 62 a-c, we plot X^2 as a function of σ_δ ; here γ_δ and the background polynomials are varied, and it can be

seen that the degree of the polynomial needed for a good fit is saturated at 4, 3, and 1 terms respectively at 3.8, 4.5, and 6.3 gev/c. The difference $X^2 - X^2_{\min}$ increases to 9.5, 18.6, and 15.0 respectively at $\sigma_\delta = 0$. The X^2 distributions are asymmetric, and consequently so are the error bars in table 10. The significance of the δ in the fit is determined not by the error bars but by the poorness of the fit when $\sigma_\delta = 0$.

Figures 63 a-c and 64 a-c show the likelihood contours as functions of σ_δ and γ_δ ; in 63 we show X^2 as a function of σ_δ for various γ_δ , and in 64 we plot X^2 versus γ_δ for various σ_δ . The errors on either variable are gotten from the envelope of the appropriate family of likelihood contours; thus, the curves in 62 a-c are just envelopes of the X^2 contours in 63. The errors in σ_δ and γ_δ in table 10 reflect both the uncertainty in the background and the uncertainty in γ_δ and σ_δ respectively.

The 4.5 and 6.3 gev/c data agree in minimizing X^2 at $\gamma_\delta = .06 \text{ gev}^2$, within errors, and in determining the values of σ_δ , we use this value of the width as a constraint. It is clear from 62a that the X^2 at 3.8 gev/c falls monotonically with increasing σ_δ and γ_δ ; to estimate σ_δ we fix γ_δ in 63a, and this only gives a lower bound on σ_δ . The upper bound is gotten by constraining the range of γ from the fits at 4.5 and 6.3 gev/c. The problem at 3.8 gev/c can be understood from inspection of the mass plot in figure 57. The resonance is essentially as wide as the rapidly varying background around 1 gev^2 , and the presence or absence of a broad enhancement cannot be inferred directly from the

3.8 gev/c data. The 3π phase space contribution shown in figure 66 peaks rather sharply at 1 gev in the mass - this difficulty is absent at higher beam energies.

Another problem at 3.8 gev/c is the relation between momentum acceptance and resonance width. Comparing the full width with a corresponding 10% momentum band, we find:

<u>Energy</u>	<u>Momentum Width of δ</u>	<u>10% Acceptance</u>
3.8 gev	92 mev/c	167 mev/c
4.5 gev	52 mev/c	159 mev/c
6.3 gev	27 mev/c	148 mev/c

Thus, at 3.8 gev/c the resonance at full base is wider than the acceptance and may be affected by normalization errors in the individual runs. Even if the expected phase space at 3.8 gev/c were flatter, identification of such a broad effect would be problematical. At 4.5 and 6.3 gev/c, however, the resonance spans less than a 3% momentum bite.

We also fit the cross-sections with a gaussian (width given by the resolution) representing the narrow ' δ (963)' reported in $\pi^-P \rightarrow \delta^-P$ by Kienzle et. al. ⁽³⁾, and detected in $PP \rightarrow d\delta^+$ at 3.8 gev/c by Oostens et. al. ⁽⁴⁾ Upper limits are given in table 10. The peak reported by Oostens et. al. corresponds to a C.M. cross-section of .2 microbarns/sr., which is six standard deviations larger than our measurement at 3.8 gev/c (.043 \pm .023 microbarns/sr.). Thus in our experiment, with significantly better resolution, the ' δ (963)' cross-section is inconsistent with Oostens et. al.

Our data at 3.8 gev/c agrees with Banner et. al. ⁽⁵⁾ in not seeing a narrow δ ; neither experiment shows evidence for structure in the δ region, but, as stated above, the mass plots are not inconsistent with a 60 mev wide resonance. In figure 67

we reproduce Banner's data; the dashed curve under the measurements shows the effect of subtracting out the resonance contribution as determined from our experiment. It is clear that the δ cannot produce a detectable signal in this data. The cross-section from Banner et. al. is in units of $d\sigma/dM$, not $d\sigma/dM^2$ as in 57; when the latter units are compared there are systematic differences between the experiments, but these do not alter the conclusions.

In figure 68 we return to the data from the CERN MMS experiment⁽³⁾; the data is plotted in units of standard deviations from a linear background. One bin at 960 mev is 4.5 standard deviations removed from the background, contributing 20 to the X^2 for a linear fit. The same point is 1.3 s. d. above a gaussian fit with width 10 mev; our dashed curve, which represents a 50 mev wide Breit-Wigner, lies 2.3 s. d. below this peak. Since the X^2 changes by 2 in going from the gaussian to the Breit-Wigner, the width of the ' δ (963)' is 2 standard deviations removed from 50 mev. If the latter experimental width were accepted, then the finite mass resolution of the MMS. (26 mev fwhm.) would no longer force the conclusion that $\gamma < 5$ mev. Note that the quoted mass resolution of the MMS. is wider than the fitted full width of the gaussian (20 mev). Of course, this is not necessarily the solution to the contradictory experimental results; Kienzle et. al. show evidence for narrow peaks at four beam energies. However, the effect has not been confirmed by any subsequent studies of π^-P interactions and therefore merits further study.

It is possible that the δ (963) is unrelated to the enhancement

in $PP \rightarrow d\delta^+$, which we will henceforth refer to as $\delta(975)$; the identification of either of these objects with $\pi_n(980)$ or $\pi_n(1016)$ cannot be made conclusively since the decay products of the δ 's are completely uncertain. However, the physical mass and width of the $\delta(975)$ are consistent with the parameters reported for $\pi_n(980)$, although the poorer mass resolution of the $\pi_n(980)$ experiments makes the comparison ambiguous. If this identification is made and if $\pi_n(980)$ is accordingly assigned a 60 mev width, then as argued in section I, SU(3) symmetric couplings predict a branching ratio $\gamma(KK)/\gamma(\eta\pi) = .17$, a result which is compatible with the upper limits of references 8, 10, and 31, and with the lower limit found by Astier et. al. ⁽¹²⁾

In appendix 6 we consider the possibility that the $\delta(975)$ effect in our experiment is a kinematical reflection of complicated production processes involving intermediate state baryon resonances. Briefly, if the π 's in the recoiling meson system resonate with the nucleons in the deuteron, then enhancements may be expected at certain points in the M^2 spectrum. However, it is shown that the expected widths are more than $.7 \text{ geV}^2$, or five times the observed δ width.

Excitation curves for π^+ , ρ^+ , and δ^+ production are shown in figure 69, with data from Anderson et. al. ⁽²⁹⁾, Pellett ⁽⁷⁾, Dekkers et. al., ⁽³²⁾ and Turkot et. al., ⁽³³⁾. The π^+ cross-sections from the present experiment exceed those of Anderson et. al. by 60%; however, the latter are measured at 5° , where P is .11 gev, and according to the high energy angular dependence found by Allaby et. al. ⁽³⁴⁾, namely $e^{-4.6P_1}$, a suppression of 1/1.6 is expected. At 21 gev/c Allaby et. al.

find equality between the production rates for the isovector mesons π^+ , ρ^+ , $A1^+$, and $A2^+$, and no evidence for δ^+ .

The smooth curve in figure 69 gives the energy dependence for π production found by Barger and Michael⁽³⁵⁾; it represents an approximately degenerate exchange of N_α and N_γ trajectories and can be crudely parametrized by

$$d\sigma_\pi/d\Omega = f(u) s^{2a(u)-1}, \text{ where } u \text{ is the momentum}$$

transfer, and the effective trajectory, $a(u)$, is

$$a(u) = -.8 + .6u, \text{ and}$$

$$f(u) = e^{-5u}$$

VII-3

It is seen that in the region 3 to 4 gev the π cross-section is considerably enhanced; this is explained by the direct channel resonances in the $\pi(NP)$ system, in particular in the 1920 mev region.⁽³⁶⁾ As suggested by duality, the fit by Barger and Michael averages these local enhancements.

It remains to understand the relative magnitudes of σ_π , σ_ρ , and σ_δ ; at 4.5 gev/c these are in the ratio 20:4:1, while at 21 gev they become 4:4:1. The π to ρ ratios can be understood from the residue function $f(u)$ in VII-3; if one postulates that π and ρ are produced by the same exchange mechanisms, then if $\sigma_\pi = \sigma_\rho$ at 21 gev/c, the ratio σ_π/σ_ρ should be about 5 in the low energy region, where u differs by .3 gev² (see table 12 for 0° kinematical quantities at all energies.) Note that since the ρ can be produced in 3 spin states, the cross-section equality between π and ρ at high energies implies that the effective couplings $g^2_{\pi nn}$ and $g^2_{\rho nn}$ are in the ratio 3:1 approximately, if all spin states are equally populated.

In the energy region covered by the present experiment, the excitation curves for ρ^+ and δ^+ are not significantly

different. If we postulate the same production mechanisms for π and δ , and extrapolate from the 3-6 gev data using VII-2, we expect the ratio $\sigma_\delta / \sigma_\pi$ to be about .2 at 21 gev/c. This is not in violent contradiction with Allaby et. al. The empirical fact that the isovector mesons have approximately equal production cross-sections at high energies, both in $PP \rightarrow dX^+$ and in $\pi^- P \rightarrow PX^-$ ⁽¹⁹⁾, does not in itself imply degeneracy in the couplings, since different numbers of spin states and different values of u are involved in each channel; consequently, we do not expect, as a general dynamical rule, that all isovector mesons will be produced with equal intensity at asymptopia. In the case of $PP \rightarrow d\pi^+$, the anticipated degeneracy between the contributions of the N_α and N_γ trajectories is badly broken in Barger and Michaels' fit (they require that the N_γ residue be 8 times the N_α residue to fit the data.) Thus, the observed cross-section equalities at 21 gev/c may themselves be dynamical accidents.

In conclusion, we have presented evidence for production of an ispin 1 resonance in $PP \rightarrow d\delta^+$ with mass 975 mev and width 60 mev. The high mass resolution of this experiment rules out identification with the δ (963) reported by the MMS., if the latter has width less than 5 mev. On the other hand, the statistics in the MMS. experiment do not preclude the possibility that the width of δ (963) is as large as 50 mev. In any case, if the δ (975) observed in the present experiment is identified with the π_n (980) enhancement, then a branching ratio into $K\bar{K}$ is predicted which allows identification of the π_n (980) with the π_n (1016). In studying the $\eta\pi$ system directly, it is impossible to get good mass

resolution and good signal to noise ratio when the η is identified by its 3π decay mode (especially by the $3\pi^0$ mode); therefore, a logical experimental goal would be to study the η π system in detail, detecting the 2γ decay mode of the η . It goes without saying that similar studies of the $K\bar{K}$, ρ π , and ω π channels are needed to pin down the isovector meson quantum numbers.

Appendix 1. Orbit Analysis

We calculate the coordinates along the particle orbits as functions of the trajectory parameters - p , x_0 , z_0 , dx/ds_0 , dz/ds_0 . The coordinate system is depicted in figure 70; 'y' is the longitudinal axis through the magnet center, and 'x' and 'z' are the horizontal and vertical transverse coordinates. The spectrometer arms are inclined at angles α^- and α^+ with respect to the y-axis (ingoing and outgoing ends respectively). To make the orbit analysis sufficiently rapid, the following techniques are utilized: (1) the y coordinate at each chamber is fixed, even though the spark occurs at different y values if the inclination angles α_{\pm} are not zero- this requires extrapolation of the measured coordinates, x and z, discussed below; (2) the magnetic field is defined analytically so that the effects of field inhomogeneities (dependence on x as well as on y and z) can be included as perturbative corrections, without actually tracing any rays through the field. In appendix 2 we describe the fitting procedure and the derivation of systematic errors in the chamber alignment. Note that we do not perform the momentum analysis by simply measuring the change in the slope dx/ds ($=p_x/p$), which would be appropriate for an x-independent field in which the directions can be measured independently on either end of the field; the purpose of calculating the exact coordinates along the trajectories and not simply the change in slope is to make the technique applicable to cases where the slope is not well measured on one end of the spectrometer (when 2 of the 3 chambers fail to fire), and also to be able to take

into account the error correlations caused by multiple scattering.

We summarize the formulae derived in reference 39 for describing the spatial dependence of the magnetic field. Assuming symmetry in 'z', the most general scalar potential is

$$\phi(x, y, z) = z \sum (iz)^{2n} / (2n+1)! (d/dx^2 + d/dy^2) F(x, y) \quad 1-1$$

The function F is adequately described (within a few parts in 10^4) by the sum of three functions, F_1 , F_2 , and F_3 :

$$\begin{aligned} F_1 &= B_1/2i \{ \text{Ln} (y-s_1^*/y-s_1) + \text{Ln} (y+s_1^*/y+s_1) \} \\ F_2 &= B_2/2i (1/y-s_2 - 1/y-s_2^* + 1/y+s_2 - 1/y+s_2^*) \\ F_3 &= B_3/2 (-1/y-s_3 - 1/y-s_3^* + 1/y+s_3 + 1/y+s_3^*) \end{aligned} \quad 1-2$$

where $s_i = y_i + ig_i$ are complex singularity locations - typically y_i is given by the distance from the magnet center to the edge in the y direction, and g_i is related to the transverse magnet dimensions (half the gap, roughly).

Asymptotic convergence of the trajectories requires

$$y_3 B_3 = y_1 g_1 B_1 + g_2 B_2 \quad 1-3$$

The equations of motion are

$$p \, d/dy \, dx/ds = B_z(x, y, z) - dz/dy \, B_y(x, y, z) \quad 1-4$$

$$p \, d/dy \, dz/ds = dx/dy \, B_y(x, y, z) - B_x(x, y, z) \quad 1-5$$

Since $B_z(x, y, 0) = F_1 + F_2 + F_3$, we can analytically integrate $B_z(0, y, 0)$ along the y-axis. The x-dependence of B_z , which arises through the x-dependence of the

parameters B_i and s_i in 1-2, is small and is included as a perturbation. Thus to integrate the equation of motion, neglecting the x dependence and also B_y , we find the exact solution:

$$x(y) = x_0 + (dx_0/ds \cdot y + M(y)/p) \cdot ds/dy(y) + dM(y) \quad 1-6$$

where x_0 , dx_0/ds , and p are the desired parameters.

The functions $M(y)$ and $dM(y)$ are defined by

$$M(y) = \int_0^y dy' \int_0^{y'} dy'' (F(y)),$$

$$dM(y) = - \int_0^y dy' (dx_0/ds \cdot y + M/p) (dx_0/ds + M'/p) M'' \cdot (1 - dx/ds^2 - dz/ds^2)$$

$$dx/ds(y) = dx_0/ds + M'/p \quad 1-7$$

The expression for $dM(y)$ is essentially a small geometrical correction to 1-6 to take into account the fact that the path inside the magnet is curved ; if ds/dy in 1-6 were a constant which changed abruptly at $y=0$, then dM would vanish. $dM(y)$ can be expanded in a power series in the parameters dx_0/ds , dz_0/ds , and p^{-1} with known coefficients given by definite integrals of the quantities $MM''M'^n$ and $yM''M'^n$. The dependence of the field on x can now be taken into account by adding additional perturbative terms to 1-6 which depend on the orbit parameters. The simplification arises from the nature of $F(x, y)$ in 1-2; most of the x -dependent contributions are multiplied by factors which are localized in the high gradient region, namely the functions $1/(y-s_i)^n$. The higher order derivatives in 1-1 which arise from the expansion in ' z ' give rise to higher order pole functions.

Thus, the corrections to 1-6 from the inhomogeneities consist of corrections to $M(y)$ of the type

$$dM(y) = \int \int T(x, z) / (y-s_i)^n$$

From the residue theorem, if $T(x, z)$ is slowly varying in y , only terms with $n=1$ change the outgoing slope and contribute terms like $(y-s_i) \cdot T(s_i)$ to the orbit, asymptotically. Since the functions $T(x, z)$ are known from the x -dependence of the field parameters and the coefficients of the expansion 1-1, we can express the coordinate corrections at any fixed y as a polynomial in the parameters $x_0, z_0, dx_0/ds, dz_0/ds$; concretely, we compute the coordinates x and z at the singularity locations s_i using the approximate orbit 1-6, and express the corrections as polynomials in these variables.

The solution to the vertical orbit equation 1-5 is similar to 1-6:

$$z(y) = z_0 + (dz_0/dy \cdot y + N(y)/p) \cdot ds/dy + dN(y), \text{ where}$$

$$dz/ds(y) = dz_0/ds + N'(y)/p$$

$$N(y) = \int dx z(y) dF/dy, \text{ given to an adequate approximation by}$$

$$N(y) = z(-y_1) \cdot B_1 \cdot dx/dy(-y_1) \cdot \text{Phase}(y+s_1) \cdot (y+y_1) - \quad 1-8$$

$$z(y_1) \cdot B_1 \cdot dx/dy(y_1) \cdot \text{Phase}(y-s_1) \cdot (y+y_1)$$

Knowing $p, x_0, dx_0/ds$ from an approximate fit to the x - y orbit equation 1-6, we determine $z_0, dz_0/ds$, and simultaneously $z(\pm y_1), dz/ds(\pm y_1)$ by iteratively fitting 1-8. Expression 1-8 reduces to the usual thin lens approximation when the width g_1 in $s_1 = y_1 + ig_1$ is small; in that case the phases of $y \pm s_i$ are equal to 0 ($y < y_1$), π ($y > y_1$),

and πB_1 is just $B_z(0, 0, 0)$, neglecting terms F_2 and F_3 in 1-2. These functions do not contribute directly to the focusing - asymptotically for large y they contribute a constant to $z(y)$. Finally the geometrical correction function $dN(y)$ is analogous to $dM(y)$:

$$dN(y) = - \int^y dy' (dz_0/ds + N/p)(dx_0/ds + M'/p)M''. (ds/dy)^3$$

These can be reduced to a polynomial in dx_0/dy , p as above; the final expression is linear in dz_0/ds , and $z(\pm y_1)dx/dy(\pm y_1)$, and

The contribution of $B_x(x, y, z)$ to the vertical focusing can be represented approximately as a polynomial in $x_0, dx_0/ds, z_0, dz_0/ds, p^{-1}$ which is added to $z(y)$ as a perturbation term. To calculate this contribution, we represent B_x approximately by the leading term in F , namely

$$B_x = dB_1/dx \cdot z \cdot (\ln(y-s_1^*/y-s_1) + \ln(y+s_1^*/y+s_1)).$$

Thus, all perturbation terms can be computed as polynomials in the orbit parameters; the coefficients depend on the field function and on y , the chamber location, so that the relevant expansion coefficients can be calculated once for each chamber. The importance of fixing the y coordinate of each measurement is now evident.

To define the measurements in each chamber at fixed y_i , we must swim each measurement in the horizontal plane. Referring to figure 70, if x' is the chamber coordinate, the fixed y cartesian coordinate x is given by:

$$x(y_i) = x'_i (\cos\alpha + \sin\alpha \cdot dx/ds \cdot (1 + dx/ds^2/2)) + y_i \tan\alpha + x_c \quad 1-9$$

where α is the inclination angle of the spectrometer arm, and x_c is the displacement of the beam line at the magnet center as in figure 70.

Finally, we have the following expression for the orbit coordinates in the x-y plane:

$$\begin{aligned} d_i^c = & x_o + M_i p^{-1} + dx_o/ds \cdot y_i + (x'_i \cos\alpha + y_i \tan\alpha + x_c) \\ & + (dM_i p^{-1} + (ds/dy - 1)(M_i p^{-1} + dx_o/ds \cdot y_i) - \\ & (1 + (dx/ds)^2/2)(x'_i \sin\alpha dx/ds) \end{aligned} \quad 1-10$$

In this expression d^c are random errors on the measured coordinates to be minimized; we have broken the expression into a leading term linear in the parameters, and correction terms beginning with dM/p . In the latter we include the perturbation terms due to the field inhomogeneity.

Appendix 2. Fitting the Orbit Parameters.

The general procedure for least squares fitting to a linear problem is given in reference 40, and we restate the results here, with some important observations.

If chisquare (' X^2 ') is defined as

$X^2 = d_c \cdot G^{-1} \cdot d_c$, where d_c is a vector of random errors on the measured coordinates ' x_m ', and if these coordinates must satisfy the linear relations

$$F_1 \cdot a = x_m - d_c,$$

then X^2 is minimized by the choice

$$a = F_c \cdot x_m, \text{ where}$$

$$F_c = H^{-1} \cdot F_1 \cdot G^{-1}, \text{ and}$$

$H = F_1 \cdot G^{-1} \cdot F_1 = \overline{da_i da_j}$ is the parameter error correlation matrix.

Equation lc-3, which relates the true orbit coordinates to the parameters a (x_0 , dx/ds_0 , and p^{-1}) is approximately linear in the parameters; the linearity is broken by the perturbation terms, lumped together in $dM_i(a)$. Thus, F_1 above is given from the linear part of lc-3:

$F_1(j, m)$ is M_j for $m=1$, y_j for $m=2$, and l for $m=3$ with the index ' j ' referring to the j 'th chamber coordinate.

The fit is done iteratively; for each stage of iteration, the correction terms $dM_i(a)$ are calculated from the current values of ' a ', and the residual discrepancy between measured and calculated coordinates, ' d_c ' is used to calculate corrections to a , via the relation

$$da = F_c \cdot d_c = F_c \cdot (x_m - x(a)).$$

Conventionally one redefines the gradient, $F_1 = dx/da$, at each stage of iteration, in this case including the terms $d(dM_i)/da$; also, the error matrix G should be recalculated and inverted at each stage since it depends on 'p' through the multiple scattering terms. In practice, to save computer time, F_c and G are calculated only once for each run of events.

It can be demonstrated that if the solution for a converges (in the sense that the residual corrections, da , go to zero), then no systematic error is introduced by failing to redefine either F_1 or G at each stage. Errors in these quantities do worsen the resolution, \overline{dada} , but only to second order in the errors in F_1 and G . In an experiment in which a wider range in parameter space is available, G would be approximated as a function of p , and inaccuracy in F_1 would require a systematic reduction in the step size (da) taken at each stage of iteration, to assure convergence.

We now consider the study of systematic errors. We assume that the measured coordinates have systematic errors that depend weakly on the orbit parameters. To study these effects and also to check the validity of the calculated error matrix G , we define $N-3$ pull quantities (N is the number of chamber coordinates). Also, we define a matrix V ($N-3 \times N$ dimensional) which is orthogonal to the matrix F_1 , in the sense that each of the $N-3$ rows are orthogonal to the three rows of F_1 .

$$\sum_{m=1}^N F_{1\ a m} V_{m\beta} = 0, \text{ and } \sum_{m=1}^N V_{a m} V_{m\beta} = d_{a\beta}$$

Then we define the pulls, P_a , by

$$P_a = \sum_m V_{a m} x_m^{(\text{measured})} = \sum_m V_{a m} (d_m^s + d_m^c)$$

where d^s and d^c are systematic and random errors on the coordinates, respectively. Except for these errors, the coordinates are given by $(x - d^s - d^c = F_1 \cdot a$, after subtracting the perturbation terms dM); thus, the orthogonality condition on V implies that the pulls depend only on d^c and d^s . The following quantities are of interest:

$$(1) \bar{P}_a = V_{am} \cdot d_m^s, \text{ and}$$

$$(2) \overline{P_a P_\beta} = V_{am} \cdot G_{mn} \cdot V_{\beta n}$$

The second relation gives information on G . Thus, if there are three pull quantities ($N=6$), then there are six independent correlations of pull quantities which can be compared with the R.H.S. of (2) above. For example, if $G_{ij} = g^2 d_{ij}$, then

$$\overline{P_a P_\beta} - \bar{P}_a \bar{P}_\beta = g^2 d_{a\beta}$$

Relation (1) is used to study the systematic errors. We can examine the correlation of the pull quantities with the orbit parameters as follows: let

$$P_a = \sum_1 A_a^a(l) \phi_1, \text{ where } \phi_1 \text{ is some kinematic quantity.}$$

Then

$$A_a^a(l) = Q^{-1} l_m \cdot R_a(m), \text{ where}$$

$$Q_{lm} = \overline{\phi_1 \phi_m} - \bar{\phi}_1 \bar{\phi}_m, \text{ and}$$

$$R_a(m) = \overline{P_a \phi_m} - \bar{P}_a \bar{\phi}_m$$

To determine the systematic errors d^s directly, assuming that the parameter dependence is understood, we need to impose a constraint equation; it is reasonable to minimize

the mean square deviation, or $\sum_m (d_m^s)^2$. Then it is possible to derive a matrix Z which is N X N-3 dimensional such that

$$d_n^s = Z_{na} \bar{P}_a$$

Then all estimated orbit parameters found by the methods described above are corrected by the terms

$$da_i = F_c \cdot d^s = F_c \cdot Z \cdot \bar{P}_a = F_c \cdot Z \cdot \left(\sum_I A_{I1} \phi_I \right)$$

To sum up, the arrays V and Z above are deduced directly from F_1 by orthogonality requirements. Then, for each bundle of rays in parameter space, we invert the relation between pull quantities and systematic errors, assuming for simplicity that the estimated errors are to be minimized in the mean square sense. Finally, parameter dependent corrections to a from these errors may be estimated directly.

Appendix 3: Beam Optics

Our purpose is to resolve the following uncertainties in the focusing properties of the beam elements: (1) the effective length of the quadrupole lenses, or equivalently, the gap between the lenses; (2) the vertical focusing power of the M1 and M2 magnet fringe fields. An upper limit on the strength of a magnet fringe field is gotten by treating the field as a step function with a delta function for a gradient; the horizontal ('x') field component defocuses the beam vertically to an unknown extent. For example, careful analysis of the spectrometer magnet M3 (which is similar in dimensions to M1) shows that the x component completely cancels the vertical focusing of rays that enter on the positive side of the beam line. In the M2 and M3 magnets, the x coordinates of the tracks are correlated with the relative momentum, dP , so that the defocusing is momentum dependent; in the M1 magnet the beam is sufficiently collimated to make this effect negligible. To arrange a tractable calculation, we introduce a focusing parameter for the M1 and M2 magnets defined as the ratio of actual to maximum focal strength. Since the maximum focusing in the M1 magnet is 5X greater than in the M2, we simply set the latter parameter to unity. The detailed equations governing the optical elements is given in table 2, to first order in $(1-(dy/ds)^2)$.

The measurements that determine the optical parameters include: (1) the correlation of position with direction at the

spectrometer entrance, and the dependence of this correlation on dP; (2) the extrapolated size of the vertical image at the collimator entrance. This latter should be close to the size of the collimator entrance. However, as discussed in the text, there is reason to believe that the vertical acceptance is not 100%, owing to systematic effects which cannot be disentangled- collimator misalignment, high vertical targeting, and additional vertical steering caused by M1 and quadrupole misalignment.

We start with equation IV-2:

$$\begin{aligned} \xi_s &= a^x/A^x x_s + (b^x - B^x \cdot a^x/A^x) x_t + (c^x - C^x a^x/A^x) dP + \delta_s^x \\ \lambda_s &= a^z/A^z z_s + (b^z - B^z \cdot a^z/A^z) z_t + (c^z - C^z a^z/A^z) dP + \delta_s^z \end{aligned} \quad \text{IV-2}$$

We define the correlation functions $a^x = -a^x/A^x$, $a^z = -a^z/A^z$; also we denote the quadrupole calibration uncertainty by dQ, the magnet focusing powers by X_1, X_2 , and the effective gap separation in the quadrupole by G. Calculation shows that the correlation functions are degenerate in their parameter dependence: a^x depends on the linear combination $G_x = G + 83dQ$; a^z depends on the combination $G_z = G + 4X_1 + 25dQ + .8X_2$; also, the magnification of the vertical image from the collimator entrance to the spectrometer depends on the combination $G_z' = G + 6X_1 + 120dQ$.

By minimizing a suitable likelihood function, we arrive at the following set of parameters: $G=1''$, $X_1=.25$, $X_2=1$ (by assumption), and $dQ=0$. The differences between measured correlations and the functions calculated with these parameters are shown in figure 22 (a_x) and 23 (a_z), together with the

functions themselves. In each figure we also show the differences obtained by changing the parameters G_x and G_z by $\pm 2''$. To see how much we can actually vary the parameters, we determine G_x and G_z from measurements at $dP=0$ (where systematic biases are negligible); then, regarding G as the free parameter, we fix dQ and X_1 to preserve agreement at $dP=0$, as a function of G . The correlation α^x is insensitive to variations of G ; however, the vertical correlation is upset drastically by an increase of $1''$ in G - the curve in figure 23 shows the effect of changing the gap G to $2''$.

We note that the measured correlations become weaker than the predicted values away from $dP=0$; the explanation for this is (1) there is an increase in the number of rescattered rays detected at the spectrometer entrance (these appear as a halo around the central beam position and exhibit little correlation between position and direction, and (2) escape losses in the spectrometer cause directional biases for rays with large dP .

Figure 24 shows the measured size of the vertical image at the spectrometer entrance for different sets of data. The predicted curve, ' $G_z=2'$ ', which assumes that the collimator entrance is 100% filled, exceeds the observed size by 10%. If we increase the gap G as above, keeping G_z fixed according to the correlation α^z , the variations in G_z' cause the predicted image size to increase also; the reason is that the gap must be increased at the expense of X_1 and dQ in order to maintain agreement with α^x . There is no way to decrease the predicted image size and still preserve agreement with α^x and α^z .

We now consider the systematic errors in the magnification. We have shown that if G_x and G_z are fixed, the remaining parameter G , or equivalently, G_z' , is well determined. Since G_x and G_z are known from the measurements in figures 22 and 23 to within $\pm .75''$, the resulting magnification uncertainty is 5% at $dP=0$. As G_z' is increased over the allowed range, the expected image size decreases and the dependence on dP increases, resulting in a magnification uncertainty that is linear in dP , given by $\pm .32 dP$.

The remaining terms in the transport equation IV-2 which are uncorrelated with the coordinates x_s, z_s are shown in figure 25; specifically, the measurements give the deviations from the expected slopes calculated by assuming a target location of $(-.3'', 0'')$. There are small differences between the horizontal and vertical steering from run to run that can be attributed to shifts in the primary beam coordinates. The vertical steering may be attributed to high vertical targeting as shown by the smooth curve ($z_t=.4''$), or to additional steering in the beam elements. What is important is to obtain a reliable description of this residual steering in order to calculate the spectrometer detection efficiency; explaining the steering to further accuracy is unnecessary. For each run of data, we measure the average residual steering of the central momentum rays, which are almost unbiased, to obtain equivalent average target coordinate shifts from run to run; the statistics alone allow a measurement accuracy of $\pm .1$ mr. for each run. Finally, judging from figures 22-24, the consistency of the measurements over the whole range of experimental

data, and the high statistics available, it appears that the incoming track directions are predictable to within at least .3 mr.

One final issue remains: higher harmonics in the quadrupole can perturb the linearity of the transport equations in x_s, z_s . To test this, we plot the slope deviations of central momentum rays against their coordinates x_s, z_s (these are linearly related to the coordinates at the quadrupole exit); figure 28 shows no evidence for any correlation in either plane.

Appendix 4. Acceptance

We summarize here the relevant considerations in the mathematical treatment of the acceptance problem. The observed cross-section in a momentum bin of width dP can be written

$$d\sigma/d\Omega = \int dP' dx' d\Omega' \frac{e^{-(p-p')^2/2\gamma_p^2}}{(2\pi)^{1/2}} W(x') D(\Omega', x', p') \sigma(p', \Omega') \quad 4-1$$

where $W(x)$ is the target distribution, normalized to unity, $\Omega', x', p', \sigma(p', \Omega')$ are production angles, coordinates, momentum, and cross-section,

$D(\Omega', x', p')$ is the step function that defines the acceptance;

$\bar{\Omega}(p') = \int W(x') D(\Omega', x', p') d\Omega' dx'$ is the average solid angle available.

Ignoring the dependence of $\sigma(p)$ on production angle, the simplest estimate of the differential cross-section is

$$\begin{aligned} d^2\sigma/dp d\Omega &= 1/\bar{\Omega}(p) d\sigma/dp = 1/\bar{\Omega}(p) \int dp' \frac{e^{-(p-p')^2/2\gamma_p^2}}{(2\pi)^{1/2}} \bar{\Omega}(p') \sigma(p') \\ &= \sigma(p) + \gamma_p^2/2\bar{\Omega}(p) (\bar{\Omega}(p) \sigma'' + \bar{\Omega}' \sigma' + \bar{\Omega}'' \sigma) \end{aligned} \quad 4-2$$

The error in the estimate due to the resolution is most serious at $dP=0$, where the contribution from the $\bar{\Omega}''$ term is about -1%.

Since $W(x)$ is not well known, we redefine the observed cross-section 4-1 above as

$$d\sigma'/dp = \int dp' dx' d\Omega' \frac{e^{-(p-p')^2/2\gamma_p^2}}{(2\pi)^{1/2}} W(x') D(\Omega', x', p') D_s(\Omega', p) \sigma(p', \Omega') \quad 4-3$$

where the term $D_s(\Omega', p)$ is the step function describing the cut on Ω' imposed by the fiducial requirements on the spectrometer entrance coordinates. This must be defined so that $D_s \cdot D = D_s$ everywhere, that $W(x)$ and the gaussian are large. Then the observed cross-section is

$$d\sigma'/dp = \bar{\Omega}'(p) \int dp' \frac{e^{-(p-p')^2/2\gamma_p^2}}{(2\pi)^{1/2}} \sigma(p'), \quad \text{where}$$

$$\bar{\Omega}'(p) = \int d\Omega' D_s(\Omega', p)$$

Thus the cross-section estimate becomes :

$$d^2\sigma'/dpd\Omega = 1/\bar{\Omega}(p) d\sigma/dp = \sigma(p) + \gamma_p^2/2 \sigma'',$$

and we avoid the systematic biases implicit in equation 4-2.

Appendix 5. Cerenkov Efficiency Corrections

Deuterons can trigger the cerenkov counter through the production of fast electrons by wide angle coulomb scattering in the water, and this produces a momentum dependent correction to the observed momentum spectrum. The photon production rate for an incident particle with v/c (β') greater than n' , the index of refraction, is given by:

$$d^2N_\gamma/d\lambda dL = 2\pi/137 \cdot 1/\lambda^2 \cdot (1 - 1/n^2\beta^2)$$

The total number produced in the 3" path through the counter is:

$$N_\gamma = .35 (1 - \beta_{\min}^2/\beta^2) \cdot \int_{\lambda_{\max}}^{\lambda_{\min}} 1/\lambda \cdot \bar{E}(\lambda)$$

where \bar{E} is the overall efficiency for creating photoelectrons in the R. C. A. 8575 phototubes. Taking the wavelengths between 4000 and 5000 \AA , we get:

$$N_\gamma = \bar{E}(4500 \text{ \AA}) \cdot 1750 \cdot (1 - .563/\beta^2), \beta > .75$$

The rate for the process $d + e \rightarrow e' + d + \gamma + e' + d$, where e' has $\beta > .75$, is given by

$$d^4N_\gamma/d\lambda dL_e dL_d dQ_e = 2\pi/137 \cdot (1 - \beta_{\min}^2/\beta_e^2) \cdot N_e \cdot d\sigma/dQ_e.$$

Writing $y = Q_e/m_e = 1/(1 - \beta_e^2)^{1/2}$, (Q_e is the total electron energy), we have

$$d\sigma/dy = 4\pi/137^2 \cdot 1/m_e^2 \beta_d^2 \cdot (1 - y_0(1 - \beta_d^2)/2)/(y_0 - 1)^2$$

where $y_0 = y(L_e = 0)$ is Q_e/m_e at the electron's birthplace.

We have ignored the effects of deuteron spin. To an adequate approximation, in the region of the electron energy where β_e is greater than .75, we can write

$$dy(L_e)/dL_e = I_0/\beta_e^2 = I_0 y^2 / y^2 - 1 \text{ cm}^{-1},$$

where $I_0 = 2 \text{ mev/cm} / .511 \text{ mev}$, or

$$dL_e = -dy (1 - 1/y^2) / I_0$$

Thus,

$$\frac{dN_\gamma/d\lambda}{m_e^2 \beta_d^2} = \frac{4\pi/137^2}{\lambda^2} \cdot \frac{2\pi/137 \cdot N_e L_d}{I_0} \times \int_{y_{\min}}^{y_{\max}} dy_0 \frac{(1 - y_0 (\frac{1 - \beta_d^2}{2}))}{(y_0^2 - 1)^2} \cdot \int_{y_{\min}}^{y_0} dy (1 - 1/y^2) (1 - \beta_{\min}^2 / \beta^2(y))$$

The integral over dy is really the integral over electron path length L_e , and the integral over dy_0 is over the initial energy spectrum of the electrons. The integrals over photon wave length and over deuteron path length L_d are trivial- the latter is done explicitly. In the above expression the integration boundaries are: y_{\min} is the minimum electron E/m corresponding to $\beta_e = .75$; y_{\max} is the maximum value of y_0 from the kinematics; numerically $y_{\min} = 1.51$, $y_{\max} = (1 + \beta_d^2) / (1 - \beta_d^2)$. The inner integral can be done explicitly and gives:

$$\frac{dN_\gamma/d\lambda}{m_e^2 \beta_d^2 \lambda^2 I_0} = \frac{8\pi^2 a^3 N_e L_d}{\lambda^2 I_0} \cdot \int_{y_{\min}}^{y_{\max}} dy_0 (1 - y_0 \cdot \frac{1 - \beta_d^2}{2}) \cdot \frac{(y_0 - y_{\min})^2}{y_0 \cdot (y_0 - 1)^2}$$

The remaining integral can be gotten by substituting $x = y_0 - y_{\min}$, and is:

$$I(\beta_d) = \int_0^{y_{\max} - y_{\min}} dx \left(\frac{x}{x+1.51} \right)^2 \left(\frac{1}{x+1.51} - \frac{(1-\beta_d^2)}{2} \right)$$

The final result for the integral is:

$$I(\beta_d) = -.95 - 1.34\beta_d^2 - .065(1/\beta^2 - \beta^2) - \ln\left(\frac{2\beta^2}{1-\beta^2}\right)(.77 + .51\beta^2) + 2.28 \ln(1 + \beta^2/1 - \beta^2)$$

The corresponding photon production, averaged over photon wave length, is

$$\begin{aligned} dN_\gamma/d\lambda \, d\lambda &= .029 \int_{\lambda_{\max}}^{\lambda_{\min}} \bar{E}(\lambda) / \lambda \cdot I(\beta_d) / \beta_d^2, \text{ or approximately,} \\ &= 146 I(\beta_d^2) / \beta_d^2 \cdot \bar{E} \end{aligned}$$

Finally, the probability of producing at least one electron in the photocathode is given by Poisson statistics:

$$P(\beta_d) = 1 - \text{Exp} \left(- \bar{E} \cdot 146 I(\beta_d^2) / \beta_d^2 \right)$$

Here we have lumped the photocathode conversion efficiency in the parameter \bar{E} .

Using pure water in the cerenkov counter, the rate at which deuterons were detected was measured by comparing the time of flight spectra with the cerenkov counter in coincidence with the corresponding spectrum with no such trigger requirement. The resulting percentages are shown in figure 6 together with the probability function computed for various values of the efficiency. The corresponding probability functions for seeing protons in the counter is also calculated. For our final correction factor to the raw data, we take the efficiency $\bar{E} = 1.75\%$, from figure 6.

Appendix 6. Kinematic Reflections

Pion production may proceed through intermediate states containing one or two baryonic resonances, as in the diagrams of figure 65. However, the N^* widths are too large to produce structure in the final state missing mass. Ignoring the deuteron binding energy, the momentum 4-vector of any intermediate state nucleon which occurs in a d-P-N vertex can be identified with half the deuteron momentum, i. e. $P=N=d/2$.

In the case of a two pion final state, we can write:

$$(A) \quad s_{\pi\pi} = s_t + 4m_\pi^2 - 2(s_{n\pi_1} + s_{n\pi_2}), \text{ or equivalently,}$$

$$(B) \quad s_{\pi\pi} = -s_t + 2s_{n\pi\pi} + 2M_n^2,$$

where s_t is the total C. M. energy squared; the first term is appropriate for a double N^* intermediate state (65-a), and the second to an N^*N intermediate state in which $N^* \rightarrow N\pi\pi$ (65-b). For 3π final states the appropriate diagram involves $PP \rightarrow N^*N^* \rightarrow N\pi\pi + N\pi \rightarrow d + 3\pi$ (65-c). Here we find

$$(C) \quad s_{3\pi} = s_t + s_{\pi_1\pi_2} + 2M_\pi^2 - 2(s_{n\pi_1\pi_2} + s_{n\pi_3}).$$

Thus, in the 3π final state, we must constrain not only the resonance masses $s_{n\pi\pi}$ and $s_{n\pi}$, but also we require a constraint on the 2π mass, for example, by the decay process $N^* \rightarrow N\rho$. The respective widths for kinematic reflections from these processes is the given by:

$$(A) \quad \gamma_{\pi\pi} = 2(\gamma_{n\pi_1}^2 + \gamma_{n\pi_2}^2)^{1/2}$$

$$(B) \quad \gamma_{\pi\pi} = 2 \gamma_{n\pi\pi}$$

$$(C) \quad \gamma_{3\pi} = 2(\gamma_{n\pi\pi}^2 + \gamma_{n\pi}^2 + \gamma_{\pi\pi}^2/4)^{1/2}$$

The least favorable intermediate states for these cases are N(1236)N(1236) for (A) with $\gamma_{\pi\pi} = .9 \text{ gev}^2$; NN*(1520) for (B) with $\gamma_{\pi\pi} = .72 \text{ gev}^2$, and N(1236)N*(1520) for (C), with $\gamma_{\pi\pi} = .9 \text{ gev}^2$.

Thus, the narrowest structure that can be generated in the pion mass spectrum is of the order $.7 \text{ gev}^2$, whereas the observed 'delta' full width is about $.1$ to $.15 \text{ gev}^2$. It is amusing to note that the position of the peak in the 2π mass distribution due to (B), with the intermediate state NN*(1520), occurs at $.95 \text{ gev}^2$ at $4.5 \text{ gev}/c$. Other peak positions do not coincide with the 'delta' mass region and can be ignored.

TABLE 1-Event Tallies

	EXP#1 T.Full	EXP#1 T.Empty	EXP#2 T.Full	EXP#2 T.EMPTY
<u>3.8 Gev/c</u>	62,174	29,121	106,590	35,673
<u>4.5 Gev/c</u>	64,742	31,059	125,614	50,208
<u>6.2 Gev/c</u>	42,673	15,877	55,902	9,929

TOTAL NUMBER
OF RAW EVENTS

<u>3.8 Gev/c</u>	305,000	333,000
<u>4.5 Gev/c</u>	389,000	538,000
<u>6.2 Gev/c</u>	207,000	257,000

TOTAL TARGET
FULL EVENTS USED (BOTH EXPERIMENTS)

<u>3.8 Gev/c</u>	168,674
<u>4.5 Gev/c</u>	190,356
<u>6.2 Gev/c</u>	98,575

TOTAL NUMBER OF RAW EVENTS	2,030,000
TOTAL NUMBER OF USEFUL EVENTS	629,600
TOTAL USEFUL TARGET FULL.....	457,695
TOTAL USEFUL TARGET EMPTY.....	171,876
AVERAGE RECOVERY RATE ¹	31%

¹ Useful events are events that pass all fiducial criteria, including cuts in spectrometer entrance angles and coordinates, cuts in chamber positions, cuts in confidence level of fit, and cuts in time of flight, as discussed in the text.

TABLE 2. - Beam Optics

A. Quadrupole Doublet

$$\begin{pmatrix} x_f \\ \xi_f \end{pmatrix} = \begin{pmatrix} c_2 & s_2 \\ -k_2^2 s_2 & c_2 \end{pmatrix} \begin{pmatrix} 1 & G \\ 0 & 1 \end{pmatrix} \begin{pmatrix} c_1' & s_1' \\ k_1^2 s_1' & c_1' \end{pmatrix} \begin{pmatrix} x_0 \\ \xi_0 \end{pmatrix}$$

$$\begin{pmatrix} z_f \\ \lambda_f \end{pmatrix} = \begin{pmatrix} c_2' & s_2' \\ k_2^2 s_2' & c_2' \end{pmatrix} \begin{pmatrix} 1 & G \\ 0 & 1 \end{pmatrix} \begin{pmatrix} c_1 & s_1 \\ -k_1^2 s_1 & c_1 \end{pmatrix} \begin{pmatrix} z_0 \\ \lambda_0 \end{pmatrix}$$

$$s_1' = \sinh(w_1 L) / w_1$$

$$s_1 = \sin(w_1 L) / w_1$$

$$c_1' = \cosh(w_1 L)$$

$$c_1 = \cos(w_1 L)$$

$$w_1 = k_i(1-dP)^{-1/2}$$

$$k_i = \text{Field Index (Kg/in)} \cdot .3/2.54 / P_0 \text{ (Mev/c)}$$

G = Effective gap

L = Effective length

x_0, z_0 = incident coordinates,

x_f, z_f = exit coordinates

B. Bending Magnet

$$\begin{pmatrix} x_f \\ \xi_f \end{pmatrix} = \begin{pmatrix} \cos(\theta_f) / \cos(\theta_0) & Y_{\text{eff}} \\ 0 & 1 \end{pmatrix} \begin{pmatrix} x_0 \\ \xi_0 \end{pmatrix} + (\theta_f - \theta_0) \cdot dP \cdot \begin{pmatrix} Y_{\text{eff}} \\ 1 \end{pmatrix}$$

$$\begin{pmatrix} z_f \\ \lambda_f \end{pmatrix} = \begin{pmatrix} 1 & Y_{\text{eff}} \\ (\theta_f - \theta_0)^2 (1-dP)^2 / Y_{\text{eff}} & 1 \end{pmatrix} \begin{pmatrix} z_0 \\ \lambda_0 \end{pmatrix}$$

Y_{eff} = Length of magnet element

θ_0 = entrance angle for $dP=0$

θ_f = exit angle for $dP=0$

DEUTERON MOMENTUM (MEV/c)

DEUTERON MOMENTUM (MEV/c)	Column 2	Column 3	Column 4	Column 5	Column 6	Column 7
1395*	0	0	0	0	19	0
1405*	0	0	-13	0	13	0
1415*	0	0	-8	0	9	0
1425*	0	0	-25	0	24	0
1435*	0	0	-8	0	8	0
1445*	0	4	-8	0	6	0
1455*	0	17	15	0	-23	0
1465*	0	13	2	0	-19	0
1475*	0	6	1	0	-6	0
1485*	0	7	13	0	-7	0
1495*	0	11	13	0	-12	0
1505*	0	0	1	0	0	0
1515*	0	8	7	0	0	0
1525*	0	5	-1	0	0	-4
1535*	0	15	6	0	0	-18
1545*	0	8	7	0	0	-12
1555*	0	0	-10	0	0	15
1565*	0	25	19	0	0	12
1575*	0	15	0	0	0	14
1585*	0	21	0	0	0	21
1595*	0	0	0	0	0	-3
1605*	0	9	0	2	0	1
1615*	0	0	0	-4	0	6
1625*	0	0	0	22	0	-22
1635*	0	0	0	2	0	2
1645*	0	0	0	11	0	-11
1655*	0	0	0	9	0	9
1665*	0	0	0	13	0	-13
1675*	0	0	0	-19	0	19
1685*	0	0	0	-4	0	4
1695*	0	0	0	-10	0	10
1705*	0	0	0	-16	0	16
1715*	0	0	0	9	0	0
1725*	0	0	0	0	0	0

RUNS - 3.8 Gev/c #1

TABLE 3-A

P_d (mev/c)	M.M. ² (gev ²)	χ^2	Deg. F.	Confidence	$d^2\sigma/dM^2d\Omega$	Error
1405.000*	.563*	1.831*	1.000*	.176*	41.712*	1.874*
1415.000*	.582*	.774*	1.000*	.379*	44.448*	1.831*
1425.000*	.599*	6.538*	1.000*	.011*	39.614*	1.709*
1435.000*	.617*	.670*	2.000*	.715*	40.844*	1.758*
1445.000*	.634*	.922*	2.000*	.631*	37.231*	1.686*
1455.000*	.651*	6.485*	2.000*	.039*	34.972*	1.664*
1465.000*	.668*	2.139*	2.000*	.343*	36.229*	1.737*
1475.000*	.685*	.583*	2.000*	.747*	38.610*	1.834*
1485.000*	.701*	1.971*	2.000*	.373*	32.594*	1.789*
1495.000*	.717*	2.078*	2.000*	.354*	37.718*	2.036*
1505.000*	.733*	.015*	1.000*	.904*	34.802*	2.200*
1515.000*	.749*	.816*	1.000*	.366*	31.836*	2.082*
1525.000*	.764*	.363*	2.000*	.834*	32.728*	1.976*
1535.000*	.779*	3.874*	2.000*	.144*	34.402*	1.927*
1545.000*	.794*	1.649*	2.000*	.438*	32.783*	1.772*
1555.000*	.808*	2.535*	2.000*	.282*	33.590*	1.709*
1565.000*	.823*	9.456*	2.000*	.009*	33.742*	1.645*
1575.000*	.837*	2.562*	1.000*	.109*	37.957*	1.604*
1585.000*	.851*	4.430*	1.000*	.035*	34.638*	1.569*
1595.000*	.864*	.027*	1.000*	.870*	34.850*	1.429*
1605.000*	.878*	.974*	2.000*	.614*	35.458*	1.367*
1615.000*	.891*	.267*	1.000*	.605*	37.088*	1.358*
1625.000*	.904*	5.144*	1.000*	.023*	38.976*	1.354*
1635.000*	.917*	.049*	1.000*	.825*	42.162*	1.336*
1645.000*	.929*	1.216*	1.000*	.270*	42.200*	1.295*
1655.000*	.942*	.941*	1.000*	.332*	41.676*	1.284*
1665.000*	.954*	1.800*	1.000*	.180*	41.033*	1.255*
1675.000*	.966*	3.833*	1.000*	.050*	38.980*	1.240*
1685.000*	.977*	.237*	1.000*	.626*	39.877*	1.284*
1695.000*	.989*	1.043*	1.000*	.307*	41.276*	1.320*
1705.000*	1.000*	2.761*	1.000*	.097*	39.054*	1.363*

TABLE 3-B (3.8 GEV/C #1)

DEUTERON MOMENTUM (MEV/C)

1395*	0	0	1	0	0	0	0	0	0	0	0	-2	2
1405*	0	0	3	0	0	0	0	0	0	0	0	-7	5
1415*	0	0	20	0	0	0	0	0	0	0	0	3	-8
1425*	0	0	-23	0	0	0	0	0	0	0	0	15	10
1435*	0	0	23	0	0	0	0	0	0	0	0	-20	-11
1445*	0	0	-9	0	0	0	0	0	0	0	0	0	12
1455*	0	0	6	0	0	0	-17	0	0	0	0	0	7
1465*	0	0	0	0	0	0	6	0	0	0	0	0	-4
1475*	0	0	-16	0	0	0	10	0	0	0	0	0	7
1485*	0	0	4	0	0	0	5	0	0	0	0	0	-10
1495*	0	0	1	0	0	0	-5	0	0	0	0	0	4
1505*	0	0	7	0	0	0	-7	0	0	0	0	0	1
1515*	0	0	4	0	0	0	-4	0	0	0	0	0	1
1525*	0	0	0	0	0	0	16	0	0	0	0	0	-10
1535*	0	0	0	5	0	0	8	0	0	0	0	0	-8
1545*	0	0	0	12	0	0	13	0	0	0	-24	0	6
1555*	0	0	0	-1	0	0	10	0	0	0	-12	0	2
1565*	0	0	0	2	0	0	-11	0	0	0	9	0	0
1575*	0	0	0	-1	0	0	3	0	0	0	5	0	0
1585*	0	0	0	8	0	0	-6	0	0	0	1	0	0
1595*	0	0	0	4	-14	0	-9	0	0	0	11	0	0
1605*	0	0	0	15	-10	0	5	0	0	0	1	0	0
1615*	0	0	0	-9	2	0	-4	0	0	0	12	0	0
1625*	0	0	0	11	-13	0	3	0	0	0	1	0	0
1635*	0	0	0	-6	0	0	0	0	0	0	11	0	0
1645*	0	0	0	2	-0	0	0	0	0	0	-4	0	0
1655*	0	0	0	-10	-14	0	0	0	0	0	1	0	0
1665*	0	0	0	-6	-8	0	0	0	0	0	8	0	0
1675*	0	0	0	-0	9	0	0	0	0	0	-15	0	0
1685*	0	0	0	7	6	0	6	0	0	0	0	0	0
1695*	0	0	0	-9	7	-9	0	0	0	0	12	0	0
1705*	0	0	0	-9	-3	5	0	0	0	0	0	0	0
1715*	0	0	0	-17	22	4	0	0	0	0	-14	4	0
1725*	0	0	0	0	19	-13	0	0	0	0	8	-20	0
1735*	0	0	0	0	-15	22	0	0	0	0	7	0	0
1745*	0	0	0	0	-2	1	0	0	0	0	0	0	0
1755*	0	0	0	0	3	12	0	0	0	0	0	0	0
1765*	0	0	0	0	7	-8	0	0	0	0	0	0	0
1775*	0	0	0	0	-2	3	0	0	0	0	0	0	0
1785*	0	0	0	0	0	-5	0	0	0	0	0	0	0
1795*	0	0	0	0	0	9	0	0	0	0	0	0	0
1805*	0	0	0	0	0	0	0	0	0	0	0	0	0
1815*	0	0	0	0	0	0	0	0	0	0	0	0	0
1825*	0	0	0	0	0	12	0	0	0	0	0	0	0
1835*	0	0	0	0	0	-4	0	4	0	0	0	0	0
1845*	0	0	0	0	0	-16	0	16	0	0	0	0	0
1855*	0	0	0	0	0	10	0	-10	0	0	0	0	0
1865*	0	0	0	0	0	17	0	-17	0	0	0	0	0
1875*	0	0	0	0	0	-7	0	7	0	0	0	0	0
1885*	0	0	0	0	0	8	0	-8	0	0	0	0	0

RUNS - 3.8 Gev/c #2

TABLE 4-A

P_d (mev/c)	MW^2 (gev ²)	χ^2	Deg. F.	Confidence	$d^2\sigma/dW^2 d\Omega$	Error
1375.000*	.507*	.570*	1.000*	.450*	36.371*	2.046*
1385.000*	.526*	1.039*	1.000*	.308*	39.255*	1.965*
1395.000*	.545*	.139*	2.000*	.933*	33.770*	1.747*
1405.000*	.563*	.747*	2.000*	.688*	36.006*	1.690*
1415.000*	.582*	.842*	2.000*	.657*	37.759*	1.635*
1425.000*	.599*	4.324*	2.000*	.115*	36.931*	1.599*
1435.000*	.617*	6.761*	2.000*	.034*	36.157*	1.581*
1445.000*	.634*	1.602*	1.000*	.206*	35.117*	1.529*
1455.000*	.651*	3.104*	2.000*	.212*	36.394*	1.536*
1465.000*	.668*	.452*	2.000*	.798*	30.522*	1.365*
1475.000*	.685*	2.647*	2.000*	.266*	32.229*	1.390*
1485.000*	.701*	1.076*	2.000*	.584*	32.587*	1.404*
1495.000*	.717*	.338*	2.000*	.845*	31.331*	1.365*
1505.000*	.733*	.794*	2.000*	.672*	30.228*	1.373*
1515.000*	.749*	.249*	2.000*	.883*	33.358*	1.463*
1525.000*	.764*	1.875*	1.000*	.171*	30.747*	1.407*
1535.000*	.779*	1.183*	2.000*	.554*	32.236*	1.377*
1545.000*	.794*	7.270*	3.000*	.064*	31.033*	1.307*
1555.000*	.808*	1.942*	3.000*	.584*	29.590*	1.223*
1565.000*	.823*	1.461*	2.000*	.482*	34.069*	1.257*
1575.000*	.837*	.361*	2.000*	.835*	32.313*	1.214*
1585.000*	.851*	.887*	2.000*	.642*	33.053*	1.130*
1595.000*	.864*	3.568*	4.000*	.468*	31.312*	1.012*
1605.000*	.878*	5.205*	4.000*	.267*	35.059*	1.032*
1615.000*	.891*	1.839*	4.000*	.765*	35.641*	.983*
1625.000*	.904*	2.575*	4.000*	.631*	36.463*	.973*
1635.000*	.917*	1.385*	3.000*	.709*	36.929*	.970*
1645.000*	.929*	.307*	3.000*	.959*	36.027*	.941*
1655.000*	.942*	6.095*	3.000*	.107*	37.400*	.946*
1665.000*	.954*	1.608*	3.000*	.657*	35.395*	.913*
1675.000*	.966*	4.079*	3.000*	.253*	39.573*	.943*
1685.000*	.977*	2.495*	4.000*	.646*	37.317*	.925*
1695.000*	.989*	3.416*	4.000*	.491*	38.969*	.957*
1705.000*	1.000*	2.391*	4.000*	.664*	39.461*	.989*
1715.000*	1.011*	8.443*	4.000*	.077*	37.348*	1.003*
1725.000*	1.022*	8.494*	3.000*	.037*	38.873*	1.064*
1735.000*	1.032*	5.996*	2.000*	.050*	38.393*	1.109*
1745.000*	1.043*	.056*	2.000*	.972*	38.119*	1.155*
1755.000*	1.053*	2.657*	2.000*	.265*	36.887*	1.160*
1765.000*	1.063*	.793*	2.000*	.673*	35.572*	1.181*
1775.000*	1.072*	.128*	2.000*	.938*	37.030*	1.255*
1785.000*	1.082*	.309*	2.000*	.857*	36.759*	1.344*

TABLE 4-B 3.8 Gev/c #2

P_d (mev/c)	MM^2 (gev ²)	χ^2	Deg. F.	Confidence	$d^2\sigma/dM^2dR$	Error
1405.000*	.608*	.003*	1.500*	.956*	29.066*	2.154*
1415.000*	.632*	6.630*	1.500*	.010*	23.767*	2.034*
1425.000*	.655*	1.014*	1.500*	.314*	25.604*	2.017*
1435.000*	.678*	.105*	1.500*	.746*	31.421*	2.098*
1485.000*	.789*	6.197*	2.000*	.045*	27.612*	1.504*
1495.000*	.810*	.099*	2.000*	.952*	25.687*	1.378*
1505.000*	.831*	2.054*	3.000*	.561*	27.350*	1.319*
1515.000*	.852*	4.741*	3.000*	.192*	29.142*	1.294*
1525.000*	.872*	6.154*	3.000*	.104*	29.916*	1.240*
1535.000*	.892*	3.329*	3.000*	.344*	30.686*	1.202*
1545.000*	.912*	5.025*	3.000*	.170*	30.005*	1.150*
1555.000*	.932*	2.329*	3.000*	.507*	32.986*	1.158*
1565.000*	.951*	5.440*	3.000*	.142*	32.629*	1.142*
1575.000*	.970*	1.438*	4.000*	.838*	33.992*	1.157*
1585.000*	.989*	1.894*	4.000*	.755*	35.540*	1.151*
1595.000*	1.008*	2.386*	4.000*	.665*	33.683*	1.131*
1605.000*	1.026*	1.830*	4.000*	.767*	35.582*	1.167*
1615.000*	1.044*	6.398*	4.000*	.171*	33.311*	1.125*
1625.000*	1.062*	1.069*	6.000*	.983*	34.810*	1.153*
1635.000*	1.079*	3.649*	6.000*	.724*	32.086*	1.123*
1645.000*	1.096*	2.823*	6.000*	.831*	35.824*	1.183*
1655.000*	1.113*	5.174*	6.000*	.522*	36.500*	1.237*
1665.000*	1.130*	4.444*	5.000*	.487*	35.217*	1.228*
1675.000*	1.146*	7.772*	3.000*	.051*	35.533*	1.307*
1685.000*	1.163*	2.294*	3.000*	.514*	36.717*	1.308*
1695.000*	1.179*	8.849*	3.000*	.031*	38.139*	1.327*
1705.000*	1.194*	.170*	3.000*	.982*	34.051*	1.257*
1715.000*	1.210*	4.610*	3.000*	.203*	35.698*	1.323*
1725.000*	1.225*	1.572*	3.000*	.666*	33.342*	1.295*
1735.000*	1.240*	.136*	3.000*	.987*	36.655*	1.417*
1745.000*	1.255*	3.951*	3.000*	.267*	33.122*	1.403*
1755.000*	1.270*	.608*	1.000*	.436*	31.916*	1.483*
1765.000*	1.284*	4.014*	1.000*	.045*	30.018*	1.647*
1775.000*	1.298*	.140*	1.000*	.708*	32.099*	1.608*
1785.000*	1.312*	.363*	1.000*	.547*	29.097*	1.876*
1795.000*	1.326*	.173*	1.000*	.677*	30.183*	2.066*

TABLE 5-B (4.5 gev/c #1)

P_d (mev/c)	M^2 (gev ²)	χ^2	Deg. F.	Confidence	$d\sigma/dp^2 d\Omega$	Error
1335.000*	.435*	.492*	1.000*	.483*	16.504*	1.820*
1345.000*	.460*	.752*	1.000*	.386*	20.380*	1.701*
1355.000*	.486*	3.710*	2.000*	.156*	19.934*	1.556*
1365.000*	.511*	1.350*	2.000*	.509*	22.503*	1.481*
1375.000*	.536*	.097*	3.000*	.992*	23.593*	1.385*
1385.000*	.560*	4.654*	3.000*	.199*	24.216*	1.277*
1395.000*	.584*	2.495*	4.000*	.646*	23.836*	1.185*
1405.000*	.608*	1.460*	4.000*	.834*	23.352*	1.113*
1415.000*	.632*	1.128*	4.000*	.890*	25.701*	1.108*
1425.000*	.655*	5.431*	4.000*	.246*	24.856*	1.045*
1435.000*	.678*	2.203*	3.000*	.531*	23.756*	1.008*
1445.000*	.701*	.821*	4.000*	.936*	22.890*	.992*
1455.000*	.723*	6.004*	4.000*	.199*	24.644*	.999*
1465.000*	.746*	2.402*	5.000*	.791*	23.063*	.973*
1475.000*	.767*	8.515*	5.000*	.130*	22.896*	.943*
1485.000*	.789*	6.103*	6.000*	.412*	21.740*	.929*
1495.000*	.810*	2.975*	5.000*	.704*	24.138*	.945*
1505.000*	.831*	2.936*	6.000*	.817*	26.228*	.942*
1515.000*	.852*	7.643*	8.000*	.469*	25.366*	.886*
1525.000*	.872*	7.906*	7.000*	.341*	25.932*	.851*
1535.000*	.892*	16.006*	7.000*	.025*	28.766*	.858*
1545.000*	.912*	2.992*	6.000*	.810*	28.753*	.835*
1555.000*	.932*	5.846*	7.000*	.558*	28.551*	.809*
1565.000*	.951*	1.957*	6.000*	.924*	29.571*	.801*
1575.000*	.970*	5.644*	6.000*	.464*	30.999*	.815*
1585.000*	.989*	12.507*	7.000*	.085*	31.702*	.801*
1595.000*	1.008*	5.254*	9.000*	.812*	29.475*	.779*
1605.000*	1.026*	8.881*	9.000*	.448*	29.321*	.780*
1615.000*	1.044*	6.586*	9.000*	.680*	30.277*	.799*
1625.000*	1.062*	7.656*	8.000*	.468*	30.766*	.813*
1635.000*	1.079*	3.635*	8.000*	.888*	29.991*	.836*
1645.000*	1.096*	10.649*	8.000*	.222*	31.308*	.864*
1655.000*	1.113*	2.496*	7.000*	.927*	30.698*	.889*
1665.000*	1.130*	1.884*	5.000*	.865*	32.989*	.956*
1675.000*	1.146*	3.296*	5.000*	.655*	28.342*	.951*
1685.000*	1.163*	2.710*	5.000*	.745*	33.796*	1.074*
1695.000*	1.179*	.751*	3.000*	.861*	32.999*	1.111*
1705.000*	1.194*	4.177*	4.000*	.383*	32.028*	1.188*
1715.000*	1.210*	.881*	4.000*	.927*	30.911*	1.227*
1725.000*	1.225*	3.397*	3.000*	.334*	34.882*	1.367*
1735.000*	1.240*	.423*	3.000*	.936*	31.922*	1.397*
1745.000*	1.255*	2.174*	3.000*	.537*	33.585*	1.502*
1755.000*	1.270*	.537*	3.000*	.911*	30.757*	1.528*

TABLE 6-8 (4.5 Gev/c #2)

DEUTERON MOMENTUM (MEV/C)	0	0	-2	0	0	0	1	0
1395*	0	0	-2	0	0	0	2	0
1405*	0	0	15	0	0	0	-6	0
1415*	0	0	16	-8	0	0	-12	1
1425*	0	0	14	-10	0	0	8	3
1435*	0	0	-3	0	0	0	-0	4
1445*	0	0	0	3	0	0	9	-4
1455*	0	0	0	3	0	0	3	-6
1465*	0	0	0	0	0	0	-9	6
1475*	0	0	0	-9	0	0	-15	22
1485*	0	0	0	15	0	0	2	-14
1495*	0	0	0	14	0	0	2	-14
1505*	0	0	0	-16	0	0	0	15
1515*	0	0	0	21	0	0	3	-21
1525*	0	0	0	12	0	0	10	-19
1535*	0	0	0	-5	0	0	0	0
1545*	0	0	0	-4	0	0	0	4
1555*	0	0	0	-6	0	0	0	6
1565*	0	0	0	-14	0	0	0	14
1575*	0	0	0	-9	0	0	0	9
1585*	0	0	0	0	0	0	0	9
1595*	0	0	0	0	0	0	0	9

RUNS 6.2 GeV/c #1

TABLE 7-A

P_d (mev/c)	MM^2 (gev ²)	χ^2	Deg. F.	Confidence	$d^2\sigma/dM^2 d\Omega$	Error
1335.000*	.405*	1.063*	1.000*	.303*	8.609*	1.431*
1345.000*	.446*	.128*	1.000*	.720*	9.177*	1.328*
1355.000*	.487*	.107*	1.000*	.744*	10.392*	1.303*
1365.000*	.527*	3.091*	1.000*	.079*	8.588*	1.168*
1375.000*	.567*	.157*	1.000*	.692*	10.013*	1.164*
1385.000*	.606*	3.015*	1.000*	.082*	10.531*	1.159*
1395.000*	.645*	.042*	1.000*	.838*	8.980*	1.080*
1405.000*	.683*	.060*	1.000*	.807*	8.722*	1.070*
1415.000*	.722*	1.600*	1.000*	.224*	9.496*	1.019*
1425.000*	.759*	3.072*	3.000*	.381*	6.884*	.920*
1435.000*	.797*	1.613*	3.000*	.577*	9.123*	.936*
1445.000*	.833*	.241*	3.000*	.971*	9.149*	.882*
1455.000*	.870*	.717*	2.000*	.699*	10.280*	.894*
1465.000*	.906*	.471*	2.000*	.790*	9.332*	.881*
1475.000*	.942*	.926*	2.000*	.630*	11.014*	.887*
1485.000*	.977*	5.295*	2.000*	.071*	12.633*	.878*
1495.000*	1.012*	2.989*	2.000*	.224*	7.300*	.776*
1505.000*	1.047*	2.694*	2.000*	.260*	8.822*	.810*
1515.000*	1.081*	3.031*	2.000*	.220*	9.125*	.855*
1525.000*	1.115*	5.573*	2.000*	.062*	8.417*	.861*
1535.000*	1.149*	3.657*	2.000*	.161*	9.896*	.968*
1545.000*	1.182*	.208*	1.000*	.648*	8.800*	1.001*
1555.000*	1.215*	.190*	1.000*	.663*	11.347*	1.212*
1565.000*	1.247*	.472*	1.000*	.492*	9.566*	1.281*
1575.000*	1.279*	2.108*	1.000*	.146*	8.765*	1.372*
1585.000*	1.311*	.929*	1.000*	.335*	10.187*	1.701*

TABLE 7-B (6.2 Gev/c #1)

DEUTERON MOMENTUM (MEV/C)

1395*	0	0	0	0	0	0	0
1405*	0	0	0	0	0	0	0
1415*	0	0	0	0	0	0	0
1425*	0	0	0	0	0	4	0
1435*	0	0	0	0	1	2	0
1445*	0	0	0	0	10	3	6
1455*	0	0	0	0	5	4	13
1465*	0	0	0	0	14	14	2
1475*	0	0	0	0	2	1	1
1485*	0	0	0	0	1	10	9
1495*	0	0	0	0	0	7	7
1505*	0	0	0	0	15	9	7
1515*	0	0	0	0	2	7	3
1525*	0	0	0	0	2	10	11
1535*	0	0	0	0	9	7	14
1545*	0	0	0	0	12	10	5
1555*	0	0	0	0	14	4	17
1565*	0	0	0	0	3	0	3
1575*	0	0	0	0	3	0	3
1585*	0	0	0	0	3	0	3
1595*	0	0	2	0	6	0	6
1605*	0	0	1	0	0	0	2
1615*	0	0	9	0	0	0	2
1625*	0	4	13	0	0	0	0
1635*	0	7	7	0	0	0	0
1645*	0	9	10	0	0	0	0
1655*	0	3	3	0	0	0	0
1665*	0	4	3	0	0	0	0
1675*	0	8	8	16	0	0	0
1685*	0	5	9	9	0	0	0
1695*	0	1	7	25	0	0	0
1705*	0	1	4	19	0	0	0
1715*	0	4	16	22	0	0	0
1725*	0	1	1	3	0	0	0
1735*	0	8	18	9	0	0	0
1745*	0	3	9	11	0	0	0
1755*	0	5	5	10	0	0	0
1765*	0	9	5	14	0	0	0
1775*	0	4	6	10	0	0	0
1785*	0	9	0	11	0	0	0
1795*	0	8	0	18	0	0	0
1805*	0	22	0	22	0	0	0
1815*	0	4	0	4	0	0	0
1825*	0	6	0	16	0	0	0

RUNS 6.2 GeV/c #2

TABLE 8-A

P_d (mev/c)	MM^2 (gev ²)	χ^2	Deg. F.	Confidence	$d^2\sigma/dM^2 d\Omega$	Error
1425.000*	.759*	.035*	1.000*	.851*	14.731*	2.207*
1435.000*	.797*	.049*	2.000*	.976*	13.523*	1.324*
1445.000*	.833*	1.205*	3.000*	.752*	13.722*	1.162*
1455.000*	.870*	1.961*	3.000*	.581*	11.998*	.983*
1465.000*	.906*	2.517*	3.000*	.472*	12.755*	.910*
1475.000*	.942*	.079*	3.000*	.994*	13.668*	.862*
1485.000*	.977*	1.362*	3.000*	.714*	14.244*	.831*
1495.000*	1.012*	.826*	3.000*	.843*	13.425*	.785*
1505.000*	1.047*	2.545*	3.000*	.467*	12.870*	.750*
1515.000*	1.081*	.588*	3.000*	.899*	13.503*	.746*
1525.000*	1.115*	1.794*	3.000*	.616*	13.996*	.756*
1535.000*	1.149*	2.311*	3.000*	.510*	11.911*	.748*
1545.000*	1.182*	1.883*	3.000*	.597*	10.995*	.764*
1555.000*	1.215*	3.206*	3.000*	.361*	11.818*	.838*
1565.000*	1.247*	.102*	2.000*	.950*	11.151*	.886*
1575.000*	1.279*	.122*	2.000*	.941*	10.947*	.955*
1585.000*	1.311*	.846*	3.000*	.838*	10.136*	.978*
1595.000*	1.343*	.785*	3.000*	.853*	12.573*	1.088*
1605.000*	1.374*	.059*	3.000*	.996*	10.705*	1.079*
1615.000*	1.404*	.512*	2.000*	.774*	11.771*	1.109*
1625.000*	1.435*	2.148*	2.000*	.342*	12.436*	1.185*
1635.000*	1.465*	.570*	2.000*	.752*	10.931*	1.050*
1645.000*	1.495*	1.013*	2.000*	.603*	12.216*	.971*
1655.000*	1.524*	.143*	2.000*	.931*	10.597*	.873*
1665.000*	1.553*	.176*	2.000*	.916*	10.526*	.791*
1675.000*	1.582*	5.053*	3.000*	.168*	11.265*	.745*
1685.000*	1.610*	2.733*	3.000*	.435*	10.750*	.703*
1695.000*	1.638*	6.626*	3.000*	.085*	12.683*	.707*
1705.000*	1.666*	3.765*	3.000*	.288*	10.904*	.654*
1715.000*	1.693*	5.993*	3.000*	.112*	11.016*	.647*
1725.000*	1.721*	.154*	3.000*	.985*	10.676*	.628*
1735.000*	1.747*	3.505*	3.000*	.320*	10.602*	.627*
1745.000*	1.774*	1.651*	3.000*	.648*	11.425*	.641*
1755.000*	1.800*	1.164*	3.000*	.762*	11.951*	.669*
1765.000*	1.826*	.979*	3.000*	.806*	11.081*	.668*
1775.000*	1.852*	.549*	3.000*	.908*	10.698*	.676*
1785.000*	1.877*	1.143*	2.000*	.565*	13.537*	.772*
1795.000*	1.902*	3.488*	2.000*	.175*	11.965*	.808*
1805.000*	1.927*	5.026*	2.000*	.081*	11.987*	.848*
1815.000*	1.951*	.171*	2.000*	.918*	12.063*	.903*
1825.000*	1.976*	2.855*	2.000*	.240*	13.696*	1.018*

TABLE 8-B (6.2 Gev/c #2)

TABLE 9- Overlap Chisquares

EXPERIMENT	OVERLAP CHISQUARED ¹	DEGREES OF FREEDOM ²
3.8 Gev/c #1	126	99 (6 Runs)
3.8 Gev/c #2	177	186 (12 Runs)
4.5 Gev/c #1	217	203 (10 Runs)
4.5 Gev/c #2	409	413 (22 Runs)
6.3 Gev/c #1	76	96 (8 Runs)
6.3 Gev/c #2	81	111 (7 Runs)

¹The overlap chisquared between the runs is calculated over the momentum range $1400 < P_d < 1720$ mev/c

²The degrees of freedom are counted as the number of 5 mev/c bins in the overlapping runs minus the number of 5 mev/c bins in the momentum range 1400 to 1720 mev/c.

TABLE 10- FIT PARAMETERS

	3.8 Gev	4.5 Gev	6.3 Gev
σ_T (Mbarns/sr) (See table 11 for mass and width)	21.0 \pm .5	9.4 \pm .3	4.6 \pm .5
σ_p (Mbarns/sr)	3.2 \pm .5	2.0 \pm .4	.5 \pm .5
$\Gamma_p/2$ (Gev ²)	.10 \pm .01	.10 \pm .02	.09 (fixed)
M_p^2 (Gev ²)	.572 \pm .008	.574 \pm .012	.59 (fixed)
δ_{963} , $M^2=.927$, and width fixed by resolution.	.043 \pm .023	.019 \pm .032	.069 \pm .074
σ_f (Mbarns/sr.) ⁽¹⁾	.5 $^{+.7}_{-.15}$.48 $^{+.28}_{-.15}$.35 $^{+.10}_{-.15}$
M_f^2 (Gev ²)	.952 (fixed)	.952 \pm .012	.952 (fixed)
$\Gamma_f/2$ (Gev ²)	.06 (fixed)	.060 $^{+.016}_{-.010}$.055 $^{+.016}_{-.015}$
χ^2 , with $\sigma_f = 0$.	147 (4 Param)	111 (3 Param)	65 (1 Param)
Same, with 1 more B.G. Parameter	140	103	65
χ^2 , best fit to σ_f	137.5	92.4	51.8
Same, with 1 more B.G. Parameter	135.5	92.2	51.0
χ^2 Difference ⁽²⁾	9.5	18.6	15.0
Same, with 1 more B.G. Parameter	4.5	10.8	14.8
Number of bins in fit	127	78	38

¹ The cross section fits are based on a 4 parameter BG. at 3.8 Gev, 3 parameters at 4.5 Gev, and 1 at 6.3 Gev.

² The χ^2 differences should be distributed as for 1 degree of freedom, since the fits differ in the fixed parameter chosen for σ_f .

TABLE 11-- PION MASSES AND WIDTHS

	3.8#1	3.8#2	4.5#1	4.5#2	6.3#1	6.3#2
M_{π}^2	.0193±	.0183±	.0245±	.0177±	.0271±	.0256±
	.0004	.0004	.0012	.0007	.0020	.0039
Γ_{π}	.0235±	.0225±	.0269±	.0268±	.043±	.038±
	.0004	.0004	.0011	.0006	.002	.004
$M_{\pi}^2 - .0196$	-.0003	-.0013	.0049	-.0019	.0075	.0060
Spectrometer Calibration Uncertainty	*****		2 Mev/c	*****		
Equivalent Calibration Error (mev)	-.12	-.50	1.55	-.61	1.69	1.34
Equivalent δ Mass Error (mev)	-.1	-.5	1.6	-.6	3.4	2.7
Equivalent Beam Momentum Error (mev)	2	9	-36	14	75	58
Equivalent δ Mass Error (mev)	.3	1.3	-3.3	1.3	-3.4	-2.7

The "equivalent" calibration errors and beam momentum errors are defined to correspond to the pion mass² deviation from .0196 gev²; these deviations are larger than the errors on the fitted values of M_{π}^2 . The "equivalent" mass errors for δ^+ are the corresponding errors at 1 Gev in the missing mass.

TABLE 12-KINEMATICS

P_p (Gev)	S (Gev ²)	M^2 (Gev ²)	P_d (Mev)	dM^2/dP_d	dM^2/dP_p	u	t	s'
3.8	9.13	.02	1153	$2.52 \cdot 10^{-3}$	$-1.47 \cdot 10^{-4}$.27	-.31	3.25
		.59	1422	$1.73 \cdot 10^{-3}$	$9.63 \cdot 10^{-5}$	-.02	-.45	3.54
		.95	1675	$1.13 \cdot 10^{-3}$	$2.89 \cdot 10^{-4}$	-.32	-.60	3.72
4.5	10.50	.02	1190	$3.12 \cdot 10^{-3}$	$-1.33 \cdot 10^{-4}$.23	-.33	3.94
		.59	1397	$2.43 \cdot 10^{-3}$	$5.06 \cdot 10^{-5}$.01	-.43	4.22
		.95	1561	$1.96 \cdot 10^{-3}$	$1.80 \cdot 10^{-4}$	-.18	-.53	4.41
6.3	13.56	.02	1243	$4.43 \cdot 10^{-3}$	$-1.08 \cdot 10^{-4}$.18	-.35	5.47
		.59	1381	$3.85 \cdot 10^{-3}$	$1.18 \cdot 10^{-5}$.03	-.43	5.75
		.95	1479	$3.47 \cdot 10^{-3}$	$9.06 \cdot 10^{-5}$	-.08	-.48	5.93
21.0	41.3	.02	1355	$11.5 \cdot 10^{-3}$	$-3.81 \cdot 10^{-5}$.08	-.40	19.33
		.59	1391	$15.8 \cdot 10^{-3}$	$-9.04 \cdot 10^{-6}$.02	-.43	19.62
		.95	1414	$15.6 \cdot 10^{-3}$	$9.38 \cdot 10^{-6}$	-.01	-.44	19.80

"t" means the invariant momentum transfer squared to a single nucleon in the deuteron.

"u" means the momentum transfer to the deuteron.

M^2 is the missing mass.

S is the total invariant square mass.

"s'" is the invariant square mass of the recoiling meson system plus one nucleon in the deuteron.

Thus, denoting $V = d \cdot P_1$, the scalar product of the deuteron momentum 4-vector with the incoming proton,

$$u = M_n^2 - 2(V - 2M_n^2)$$

$$t = (u - M_n^2)/2$$

$$s' = (S + M^2 - 3M_n^2)/2$$

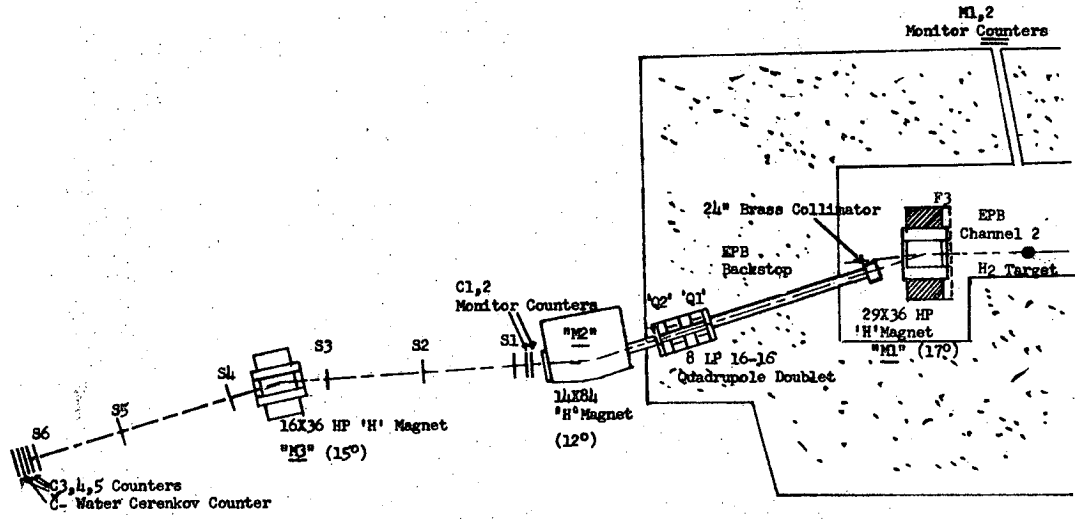


FIGURE 1

XBL 701-22

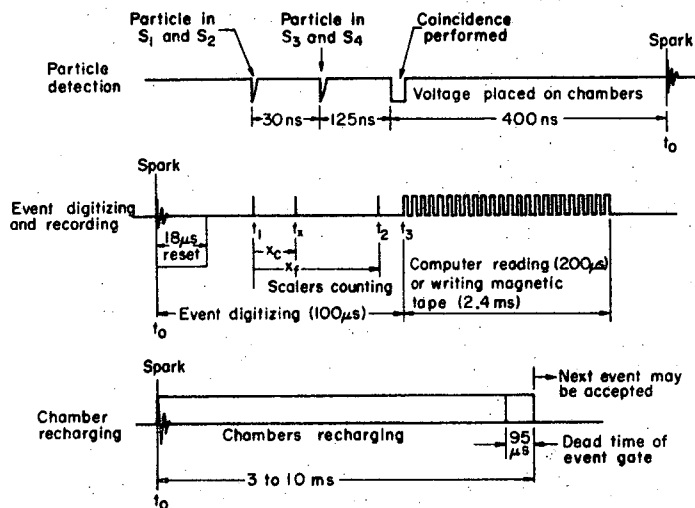


Fig. 2-A Event timing sequence, showing particle detection (nanosecond scale), event digitizing and recording (micro-second scale), and chamber recharging (millisecond scale) separately.

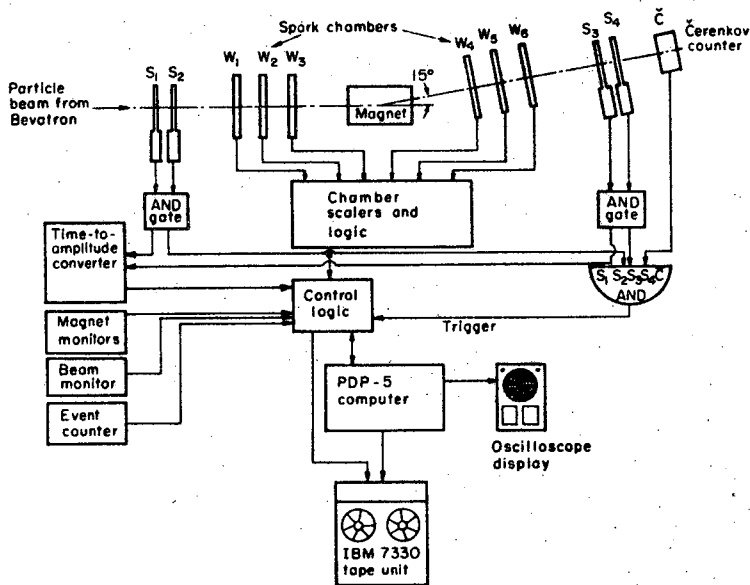


Fig.2-B Block Diagram of the Experimental Layout

FIGURE 2

XBL 701-23

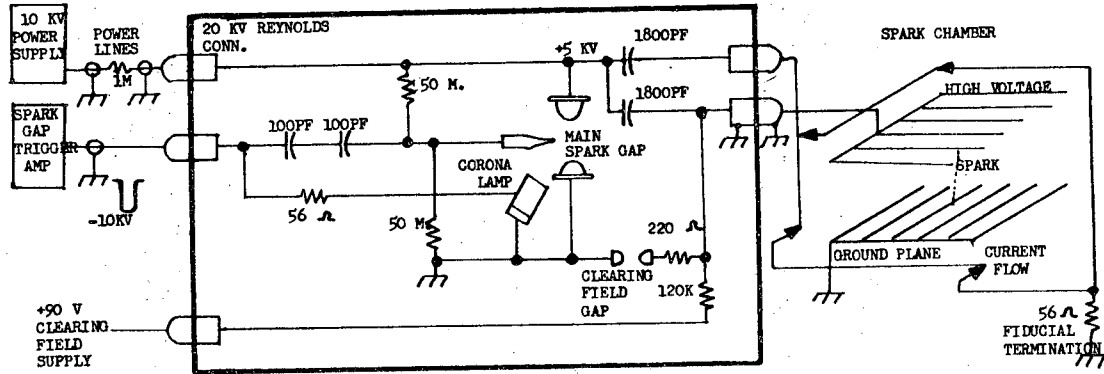
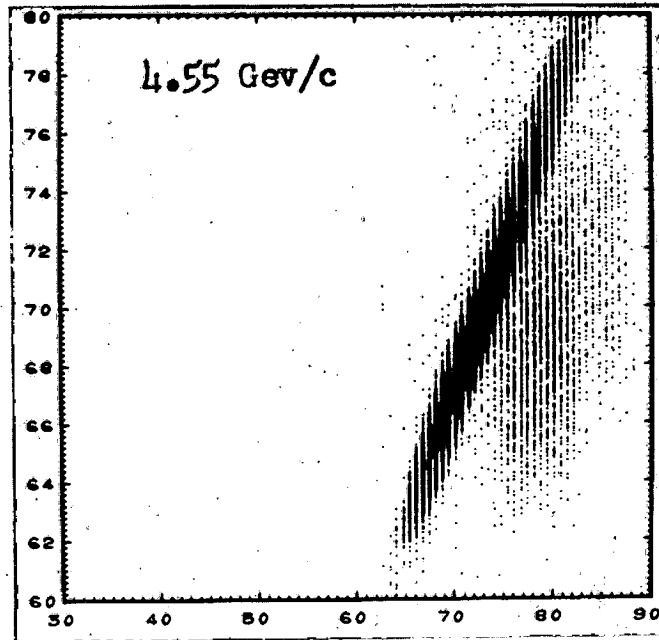
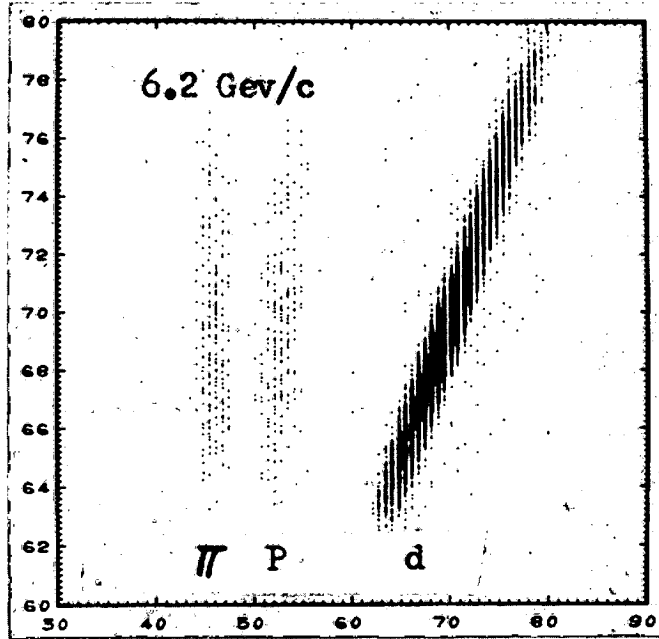


FIGURE 4

XBL 701-25

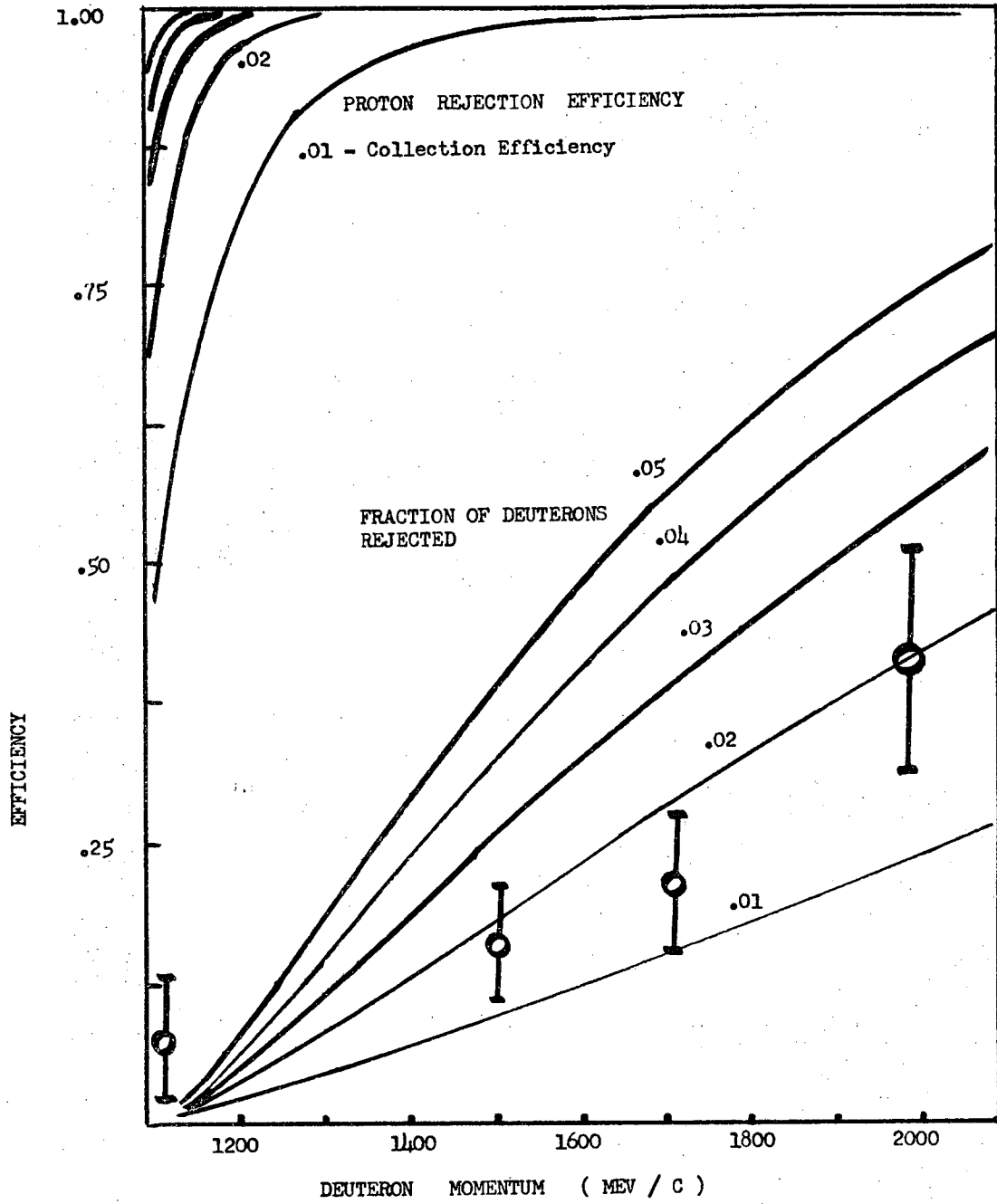
TIME OF FLIGHT FROM MOMENTUM (NS.)



MEASURED TIME OF FLIGHT (NS.)

XBB 6911-7522

Fig. 5



XBL 6911-6614

FIGURE 6

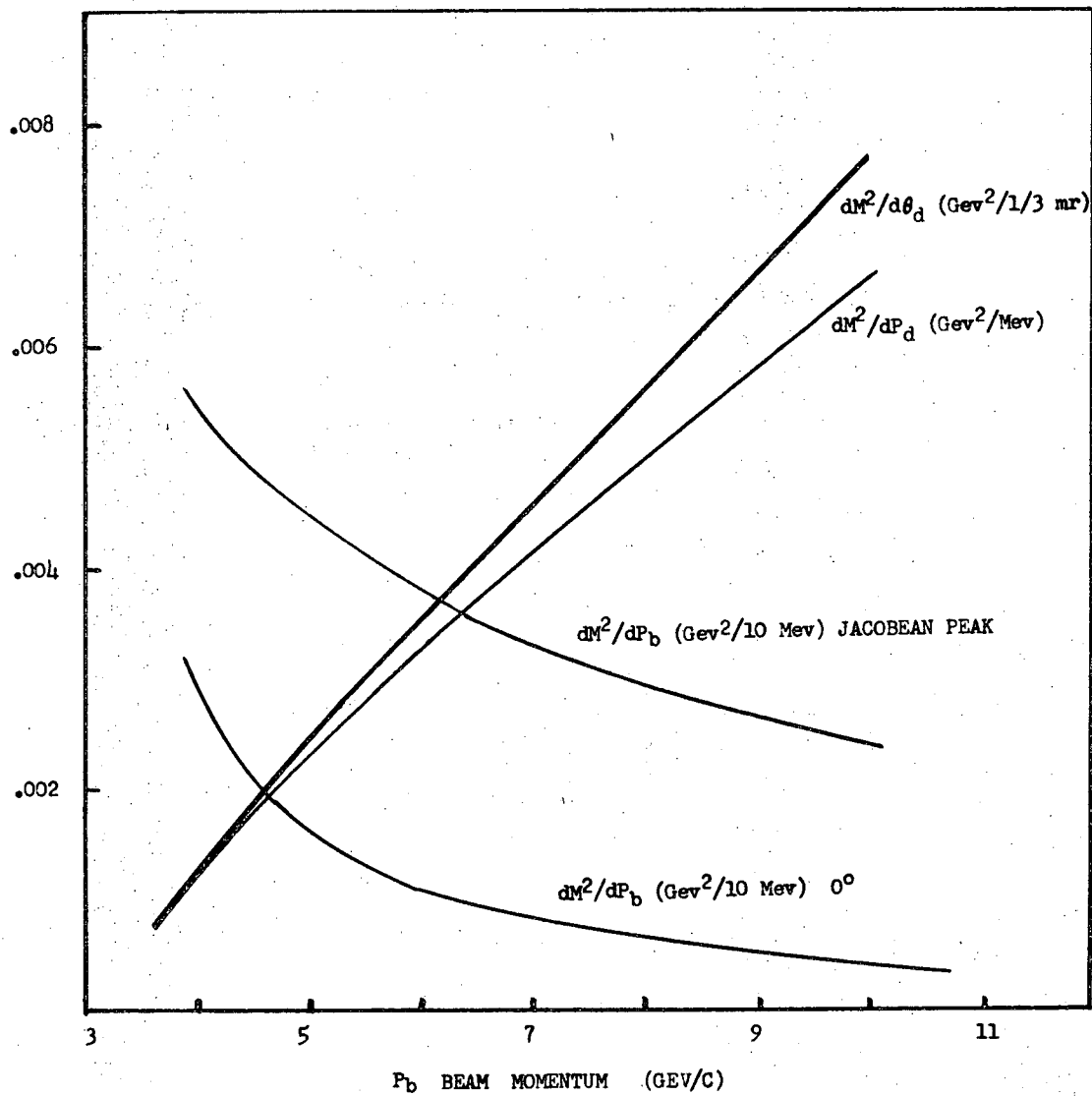


FIGURE 7

XBL 701-26

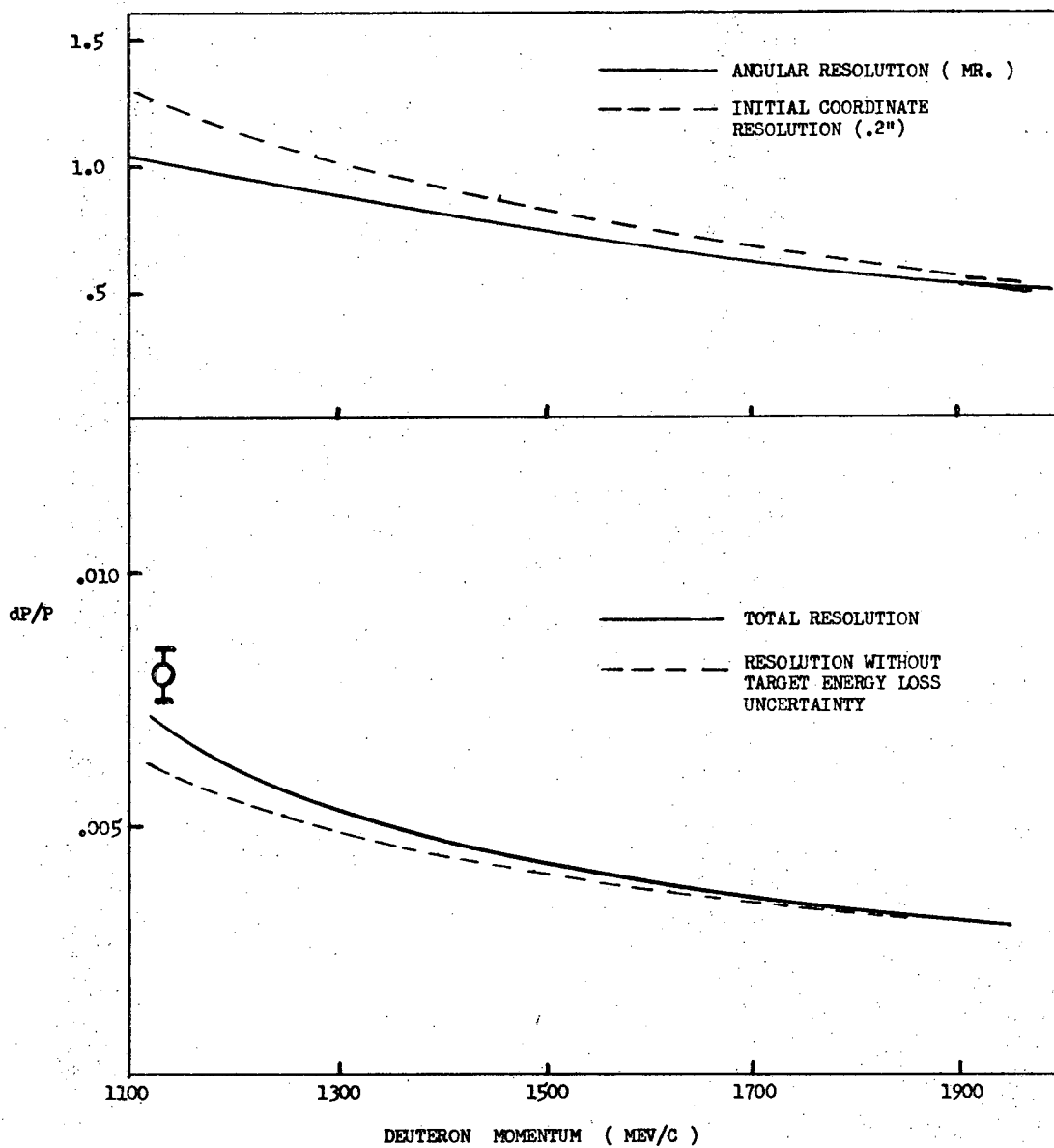


FIGURE 8

XBL 701-27

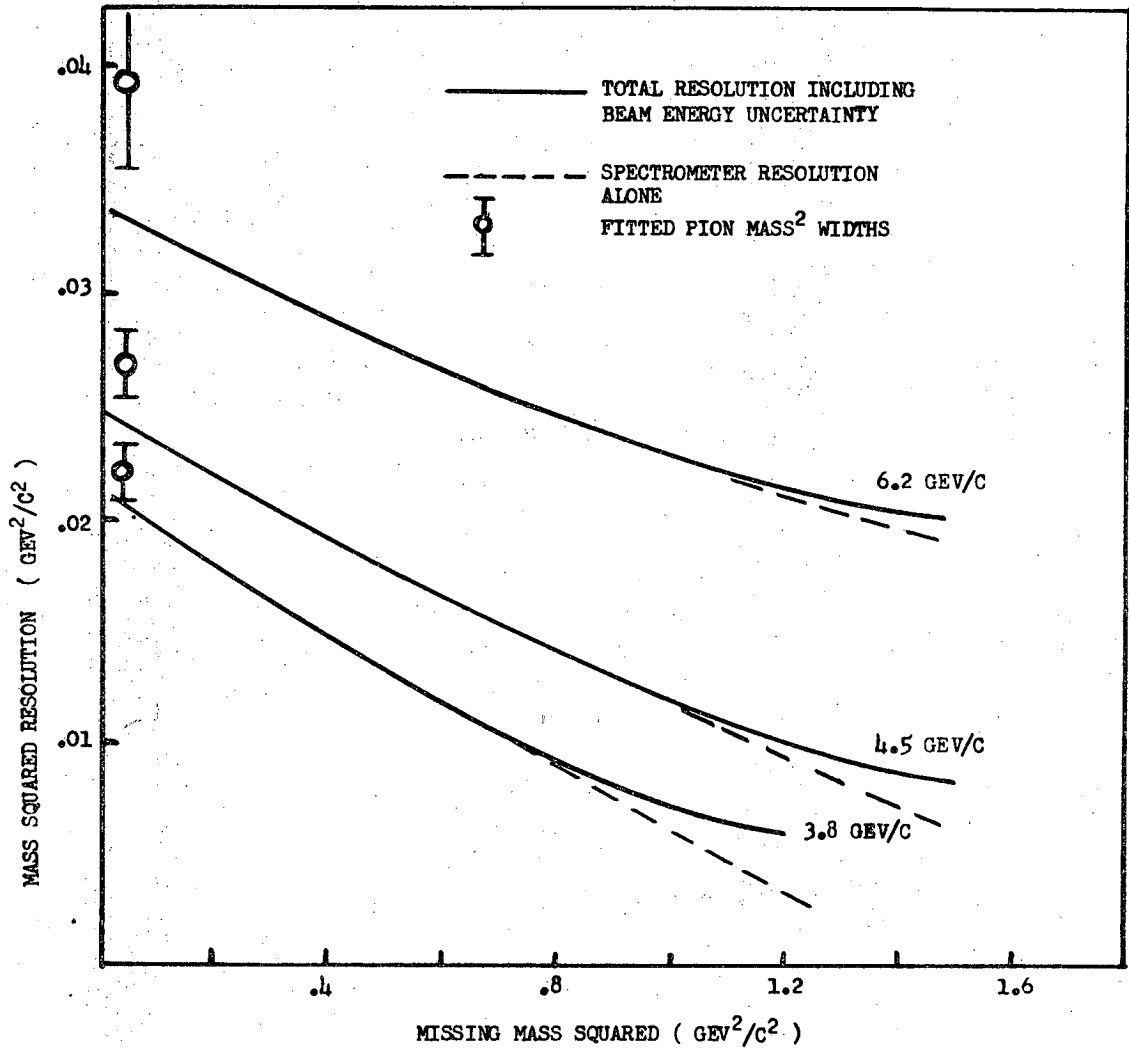
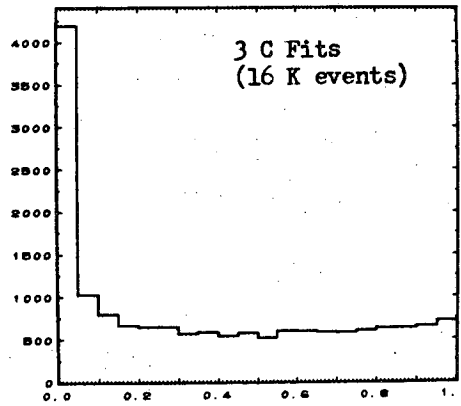
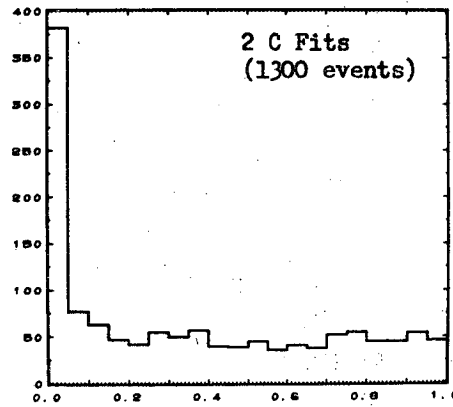
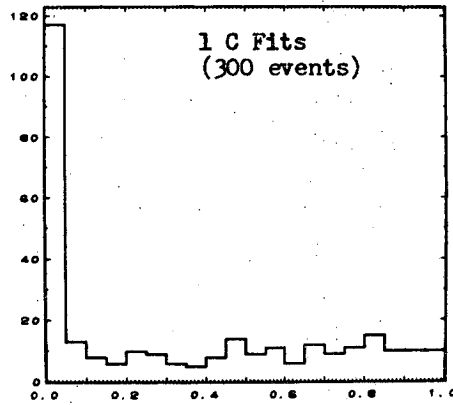


FIGURE 9

XBL 701-28

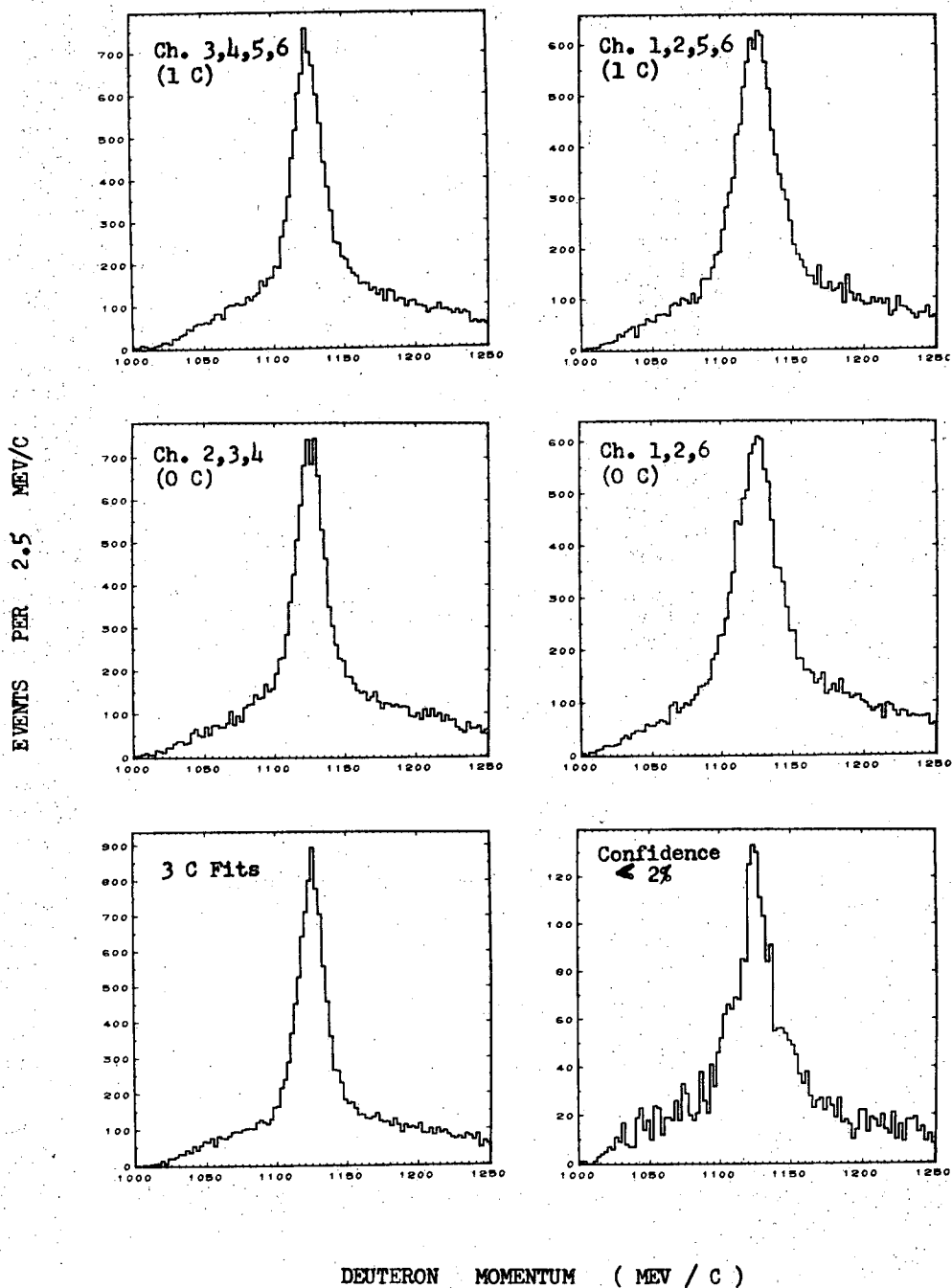
EVENTS PER .05



CONFIDENCE LEVEL

XBL 6911-6611

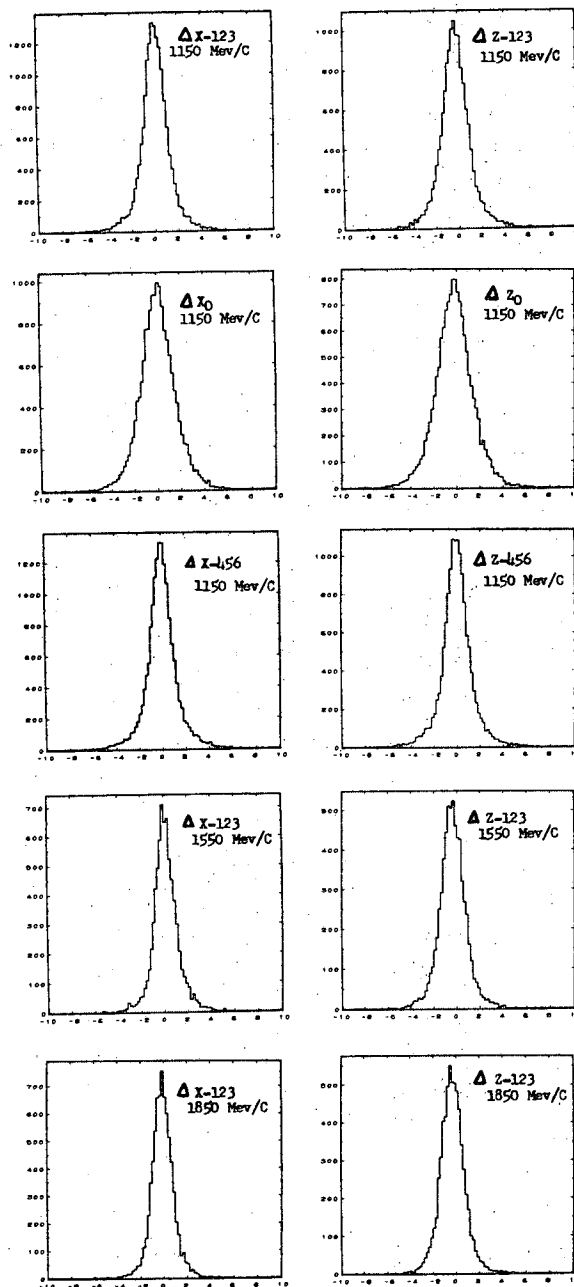
FIGURE 10



XBL 6911-6612

FIGURE 11

EVENTS PER .2



NUMBER OF STANDARD DEVIATIONS

XBL 6911-6621

FIGURE 12

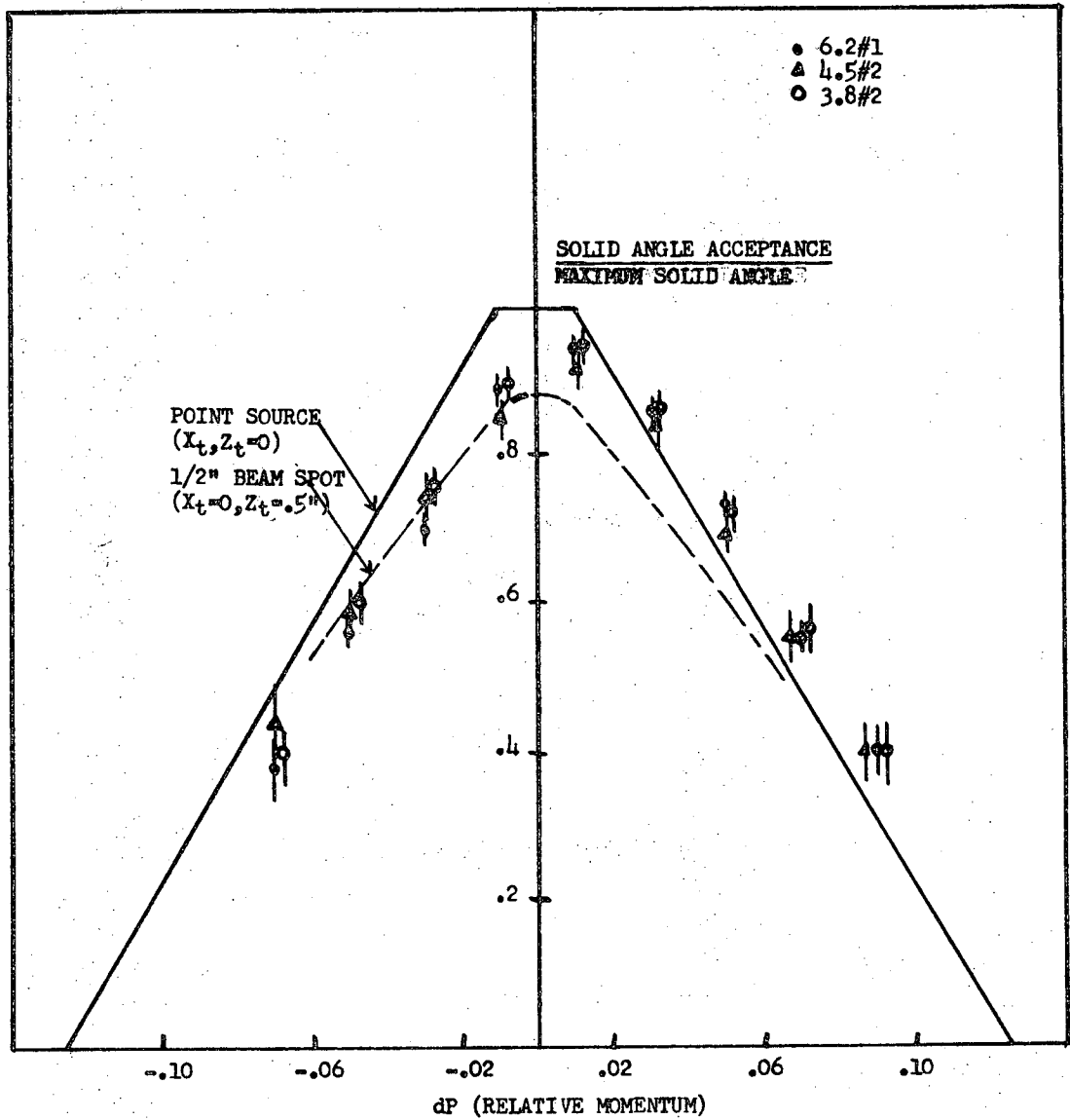
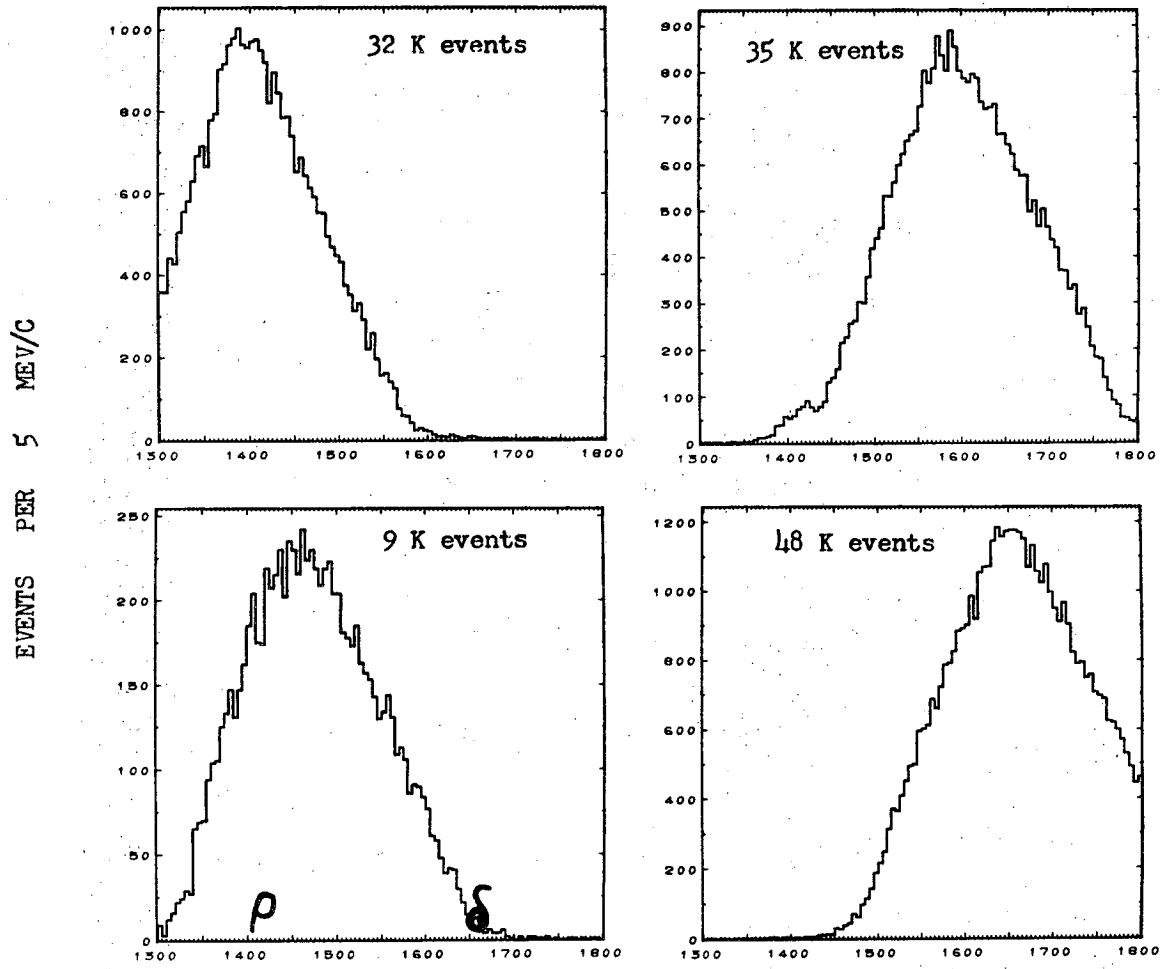


FIGURE 13

XBL 701-29



(3.8 GeV/c, EXPERIMENT # 1)

XBL 6911-6613

FIGURE 14

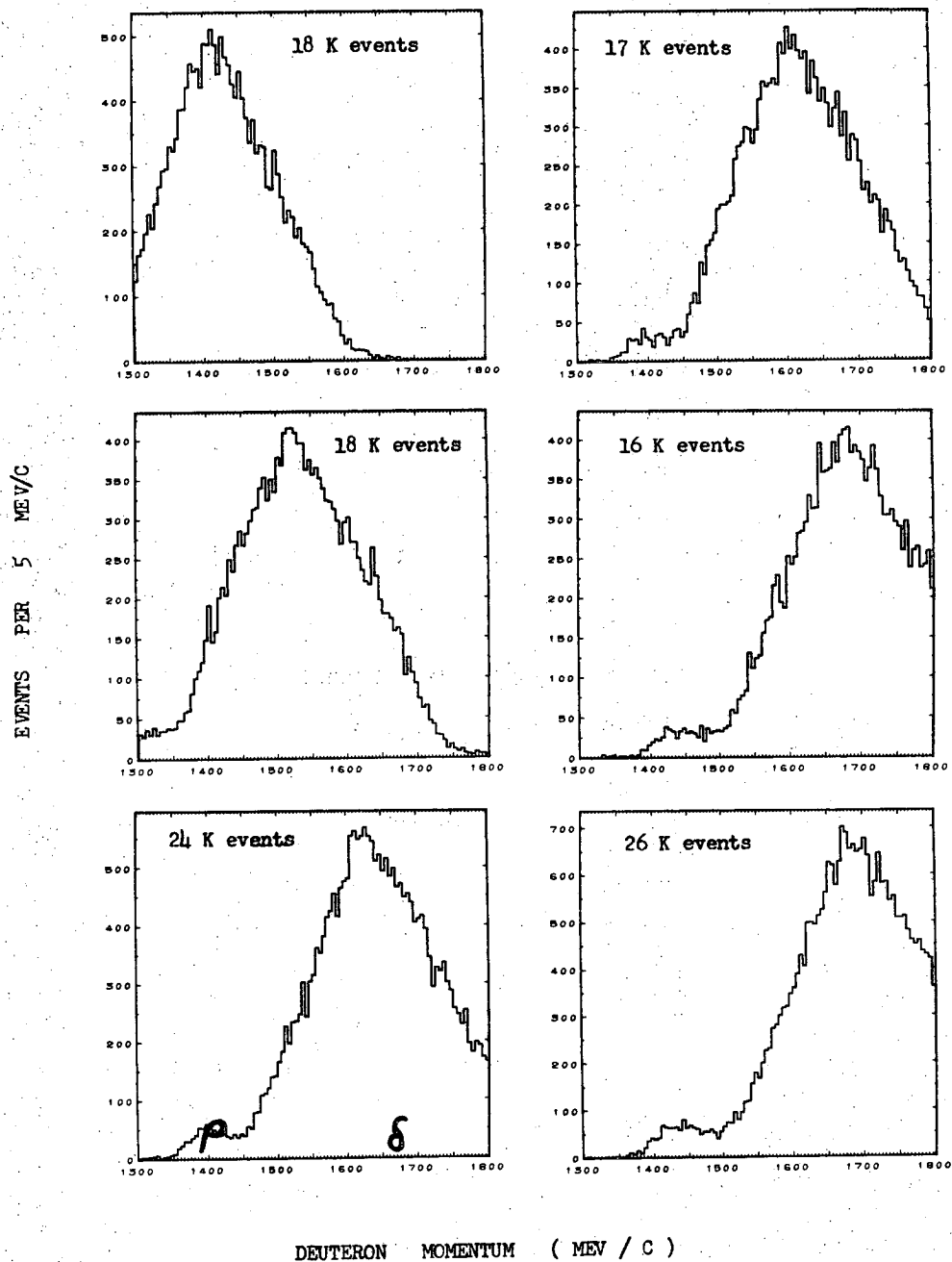


FIGURE 15

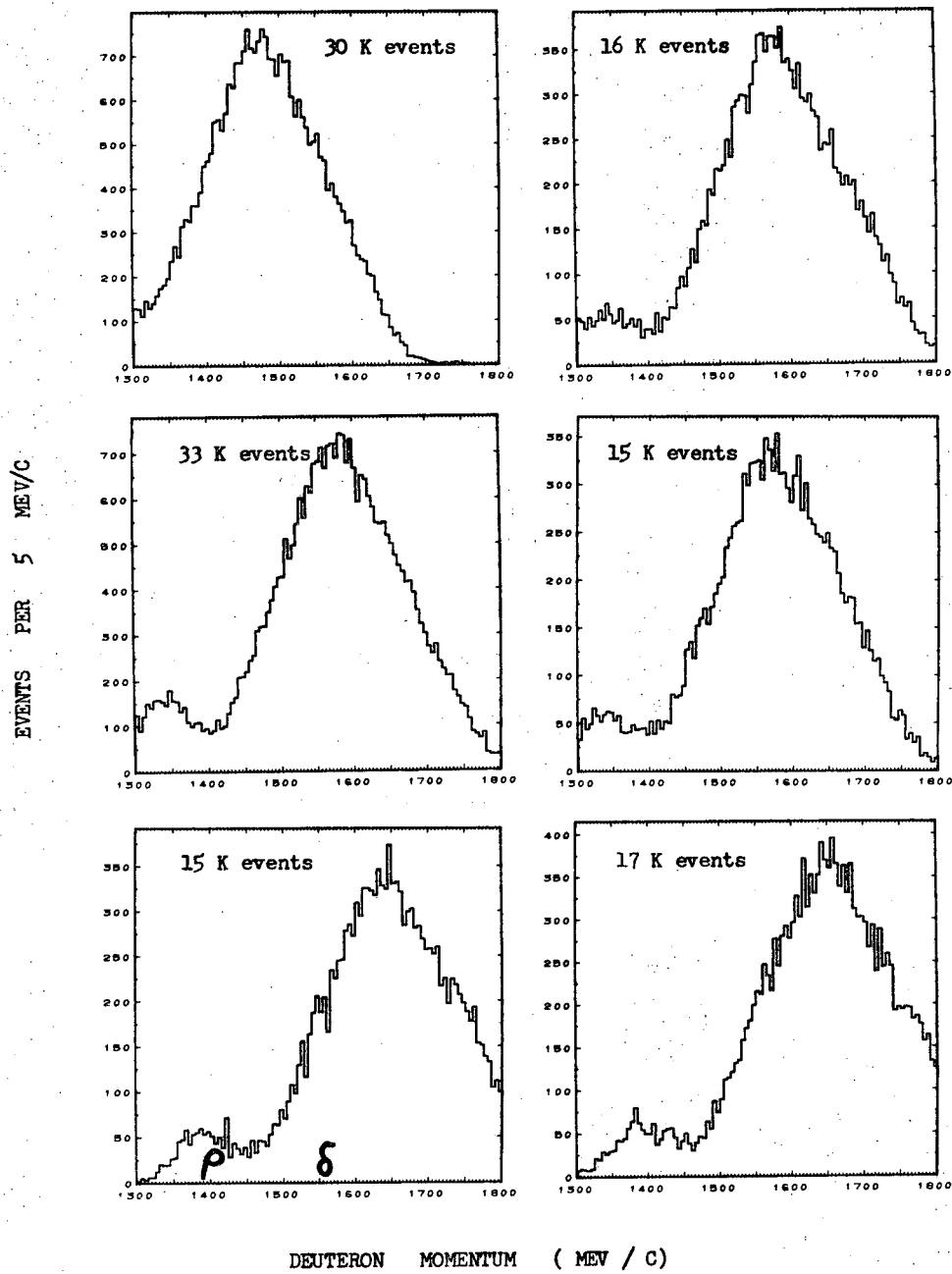
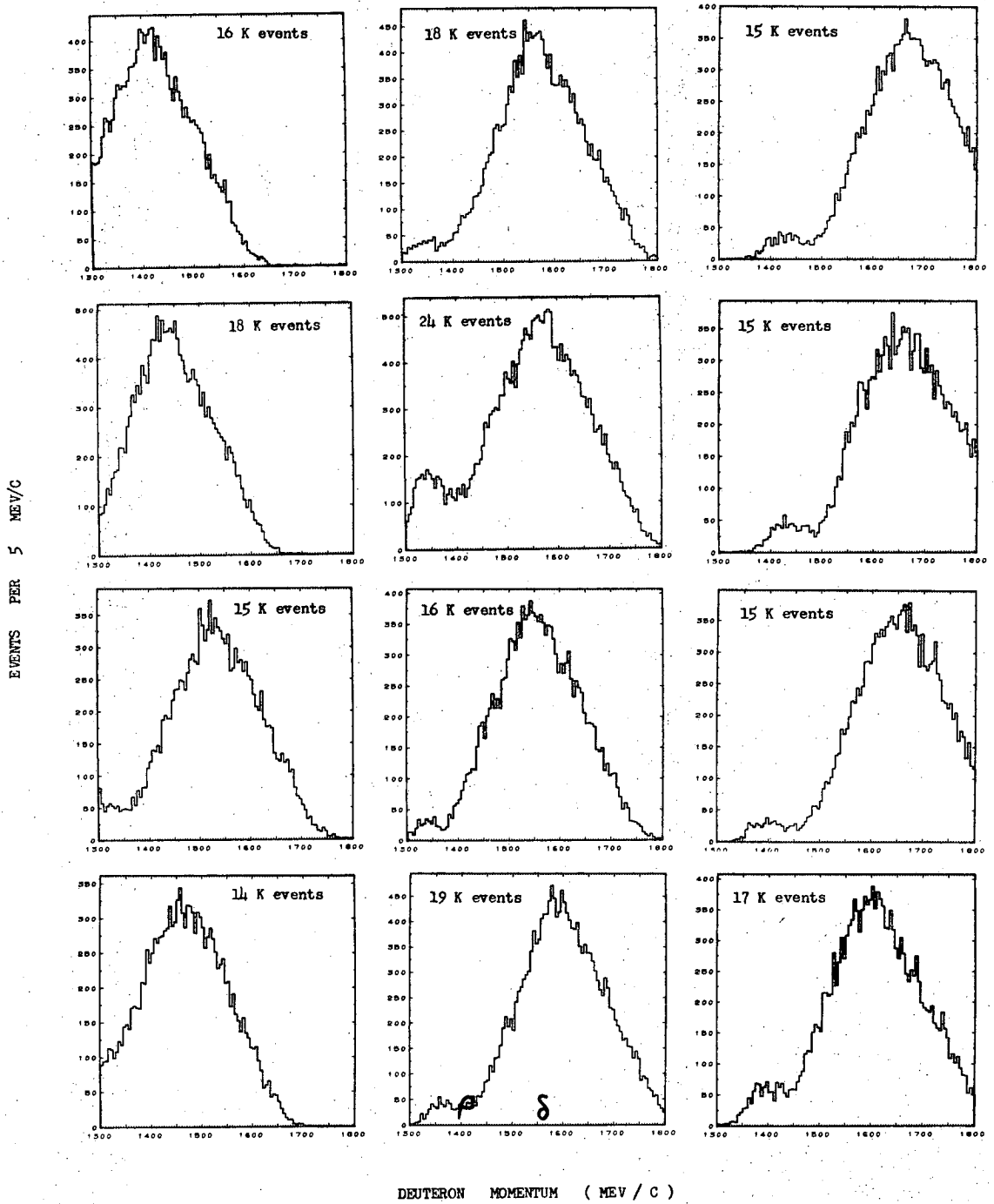


FIGURE 16



(4.5 GeV/c, EXPERIMENT #2) XBL 6911-6620

FIGURE 17

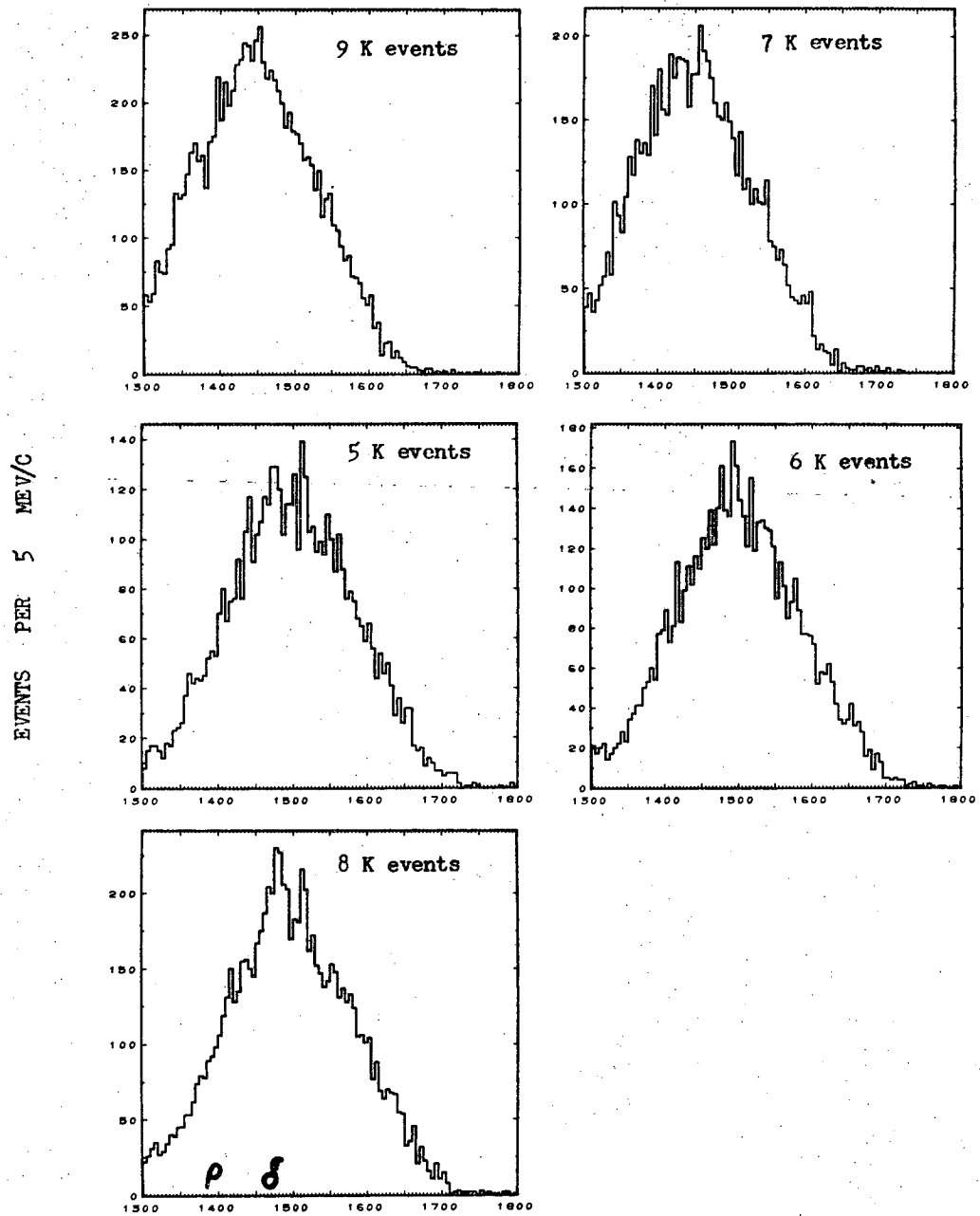
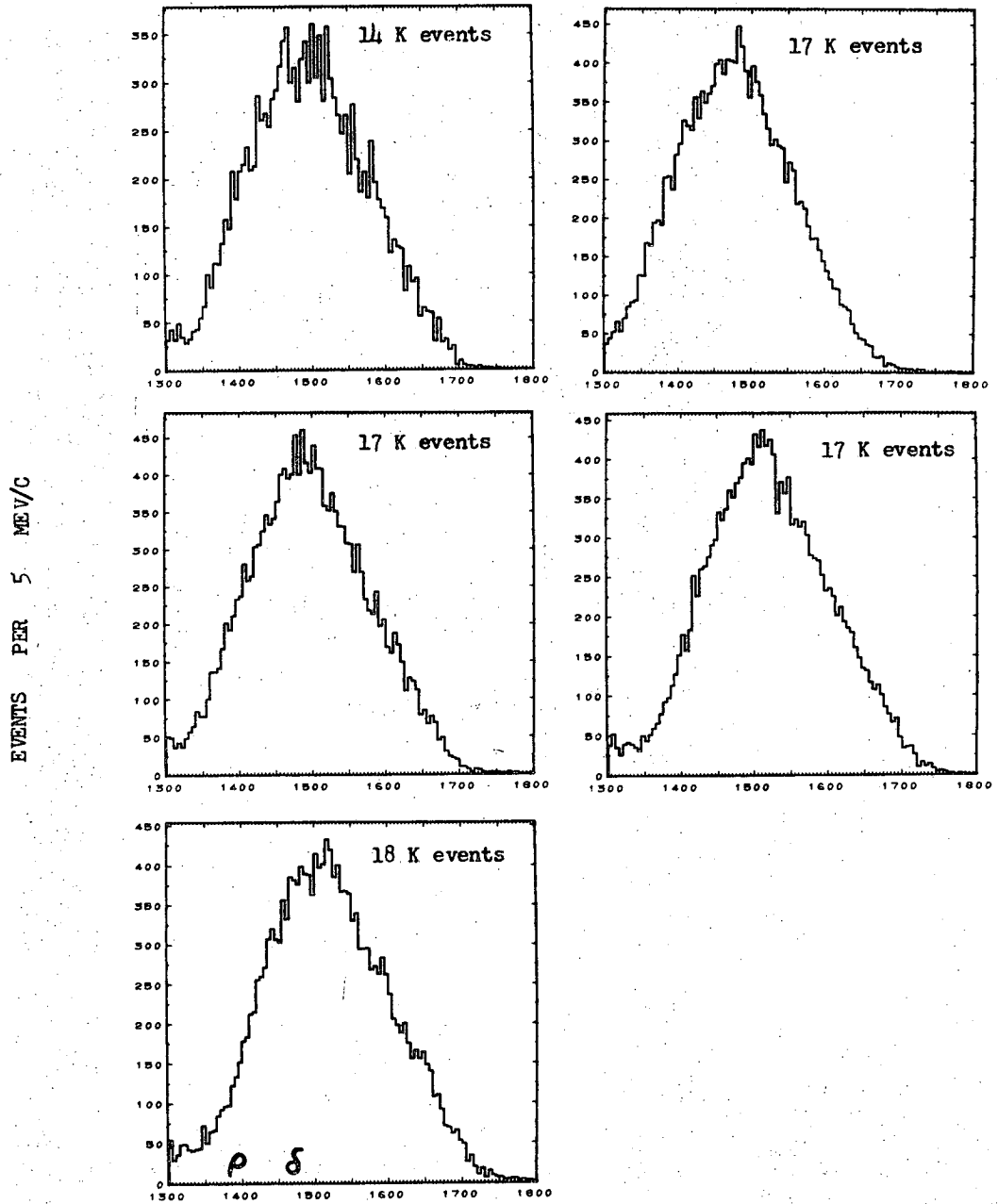


FIGURE 18



DEUTERON MOMENTUM (MEV / C)

(6.2 GeV/c, EXPERIMENT #2)

XBL 6911-6618

FIGURE 19

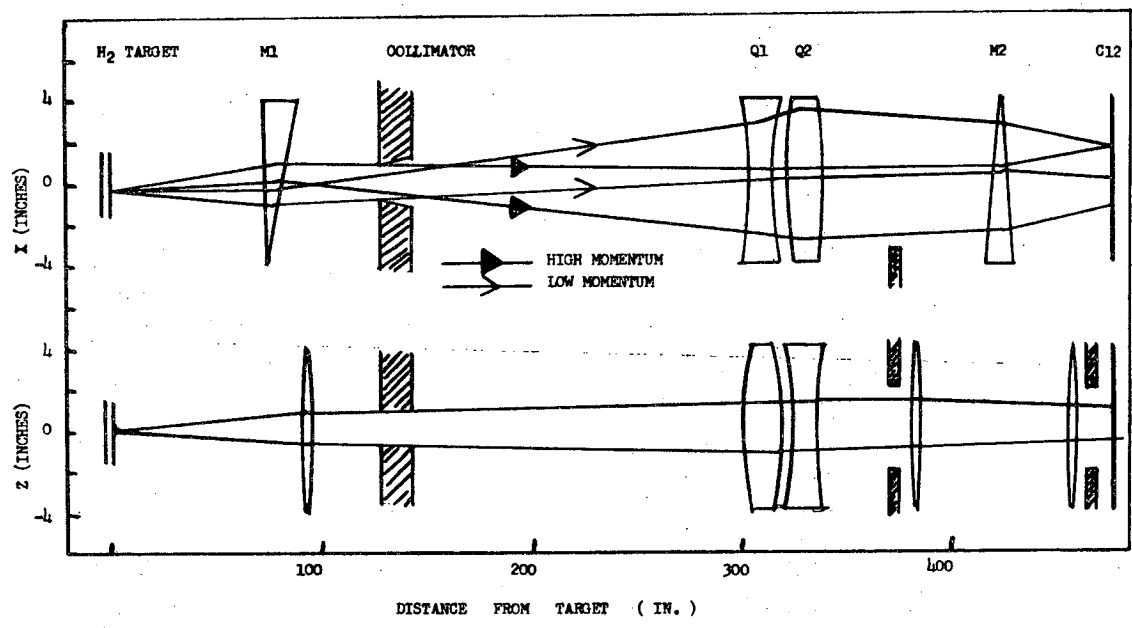
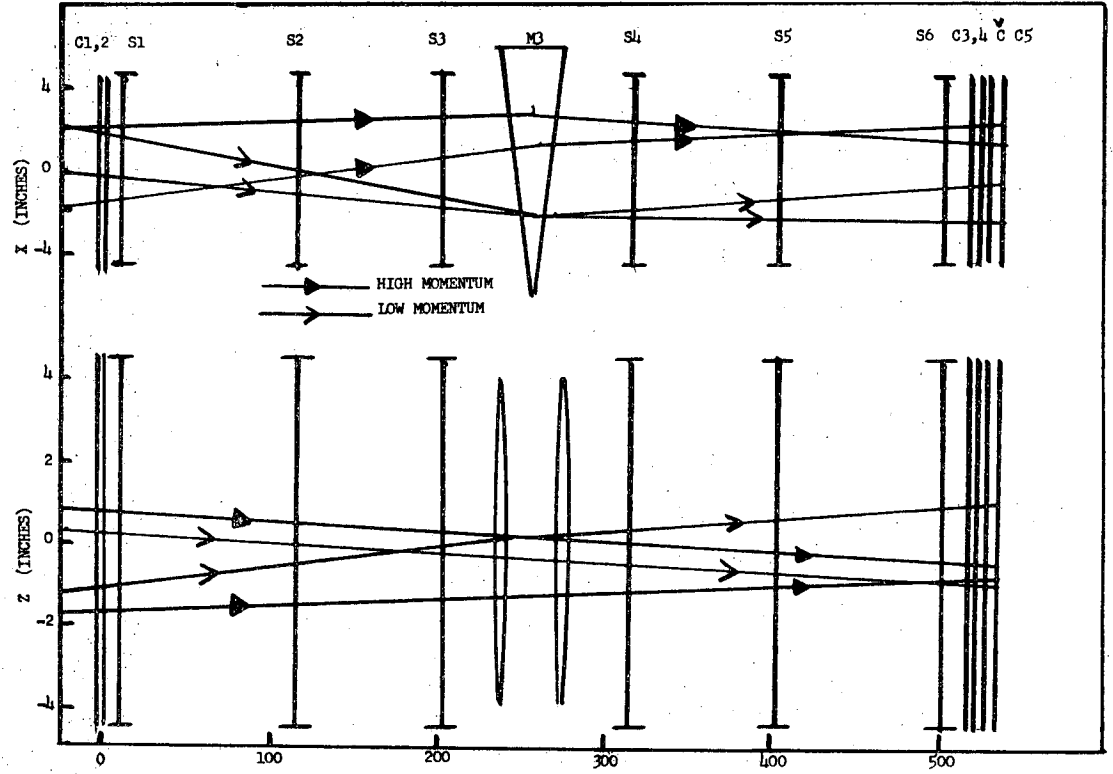


FIGURE 20

XBL 701-30



DISTANCE FROM C1-C2

FIGURE 21

XBL 701-31

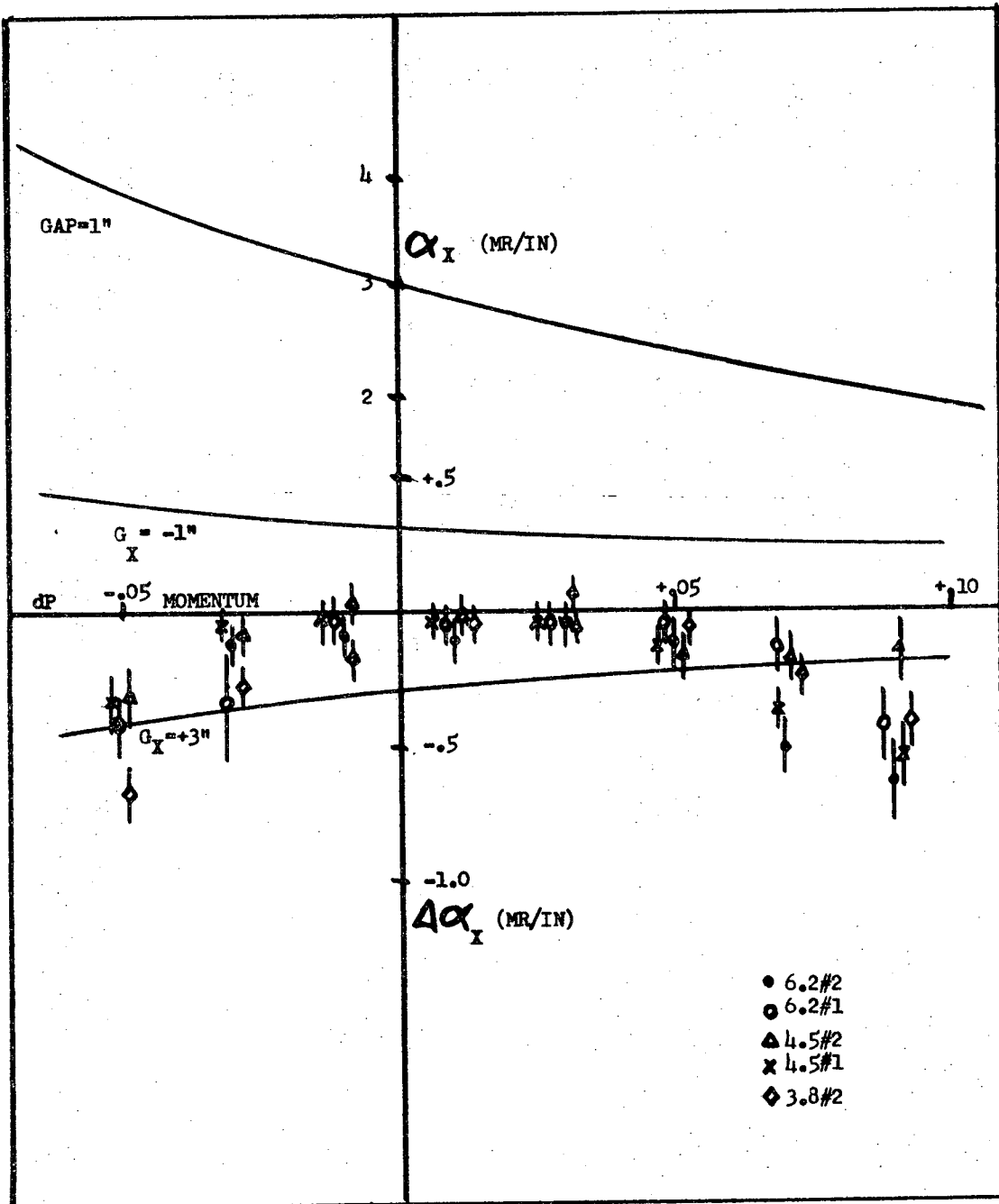


FIGURE 22

XBL 701-32

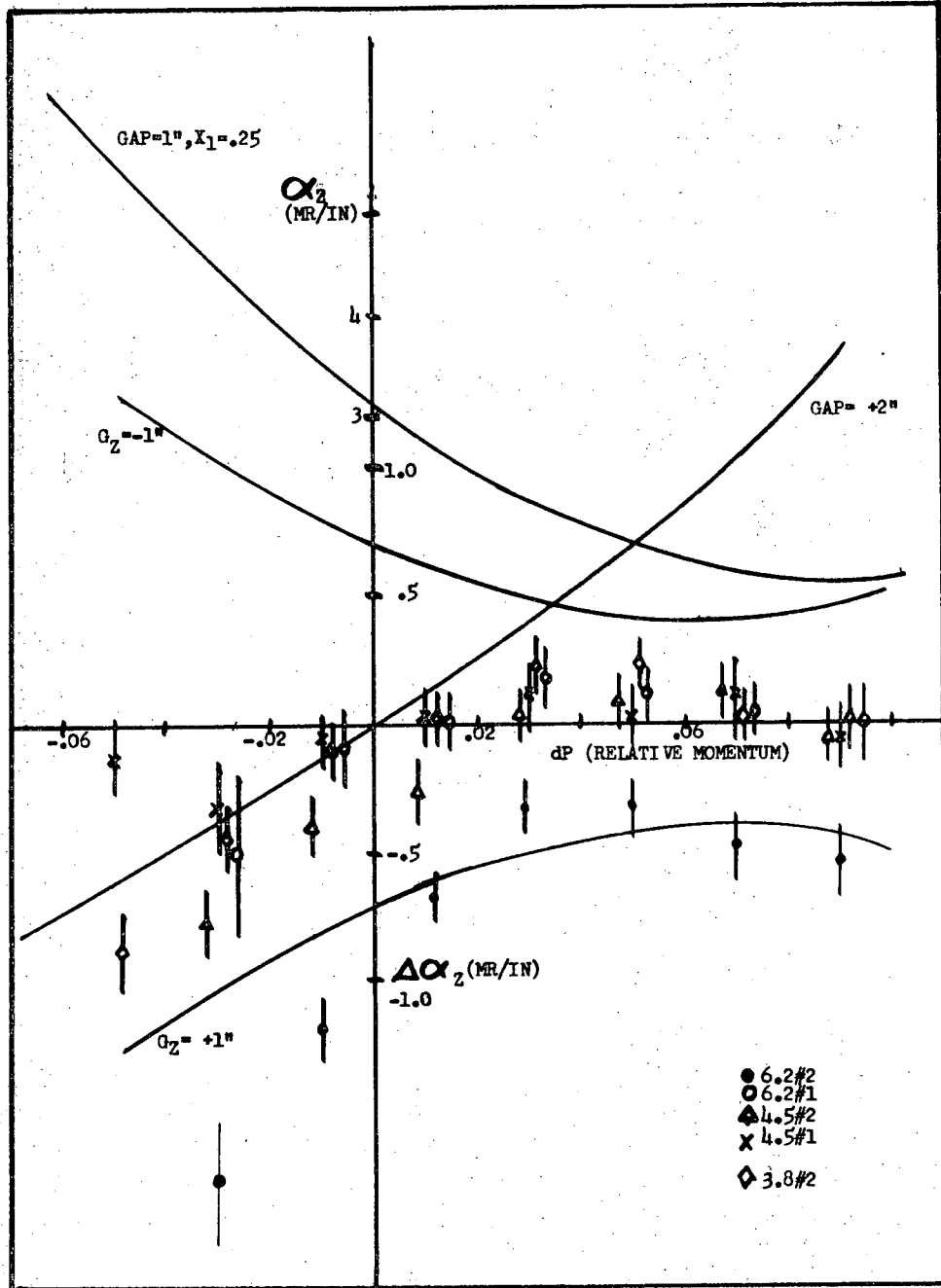


FIGURE 23

XBL 701-33

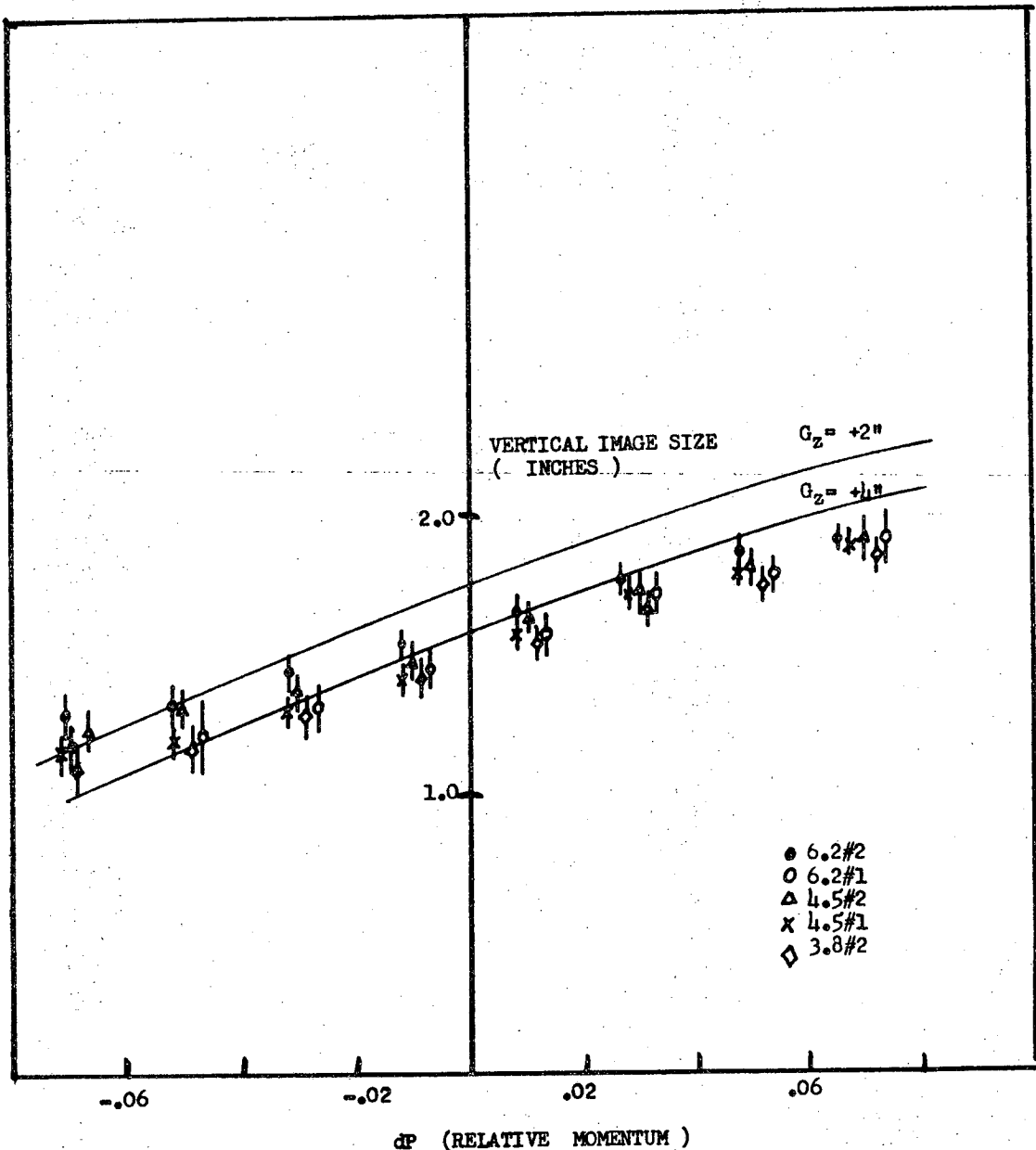


FIGURE 24

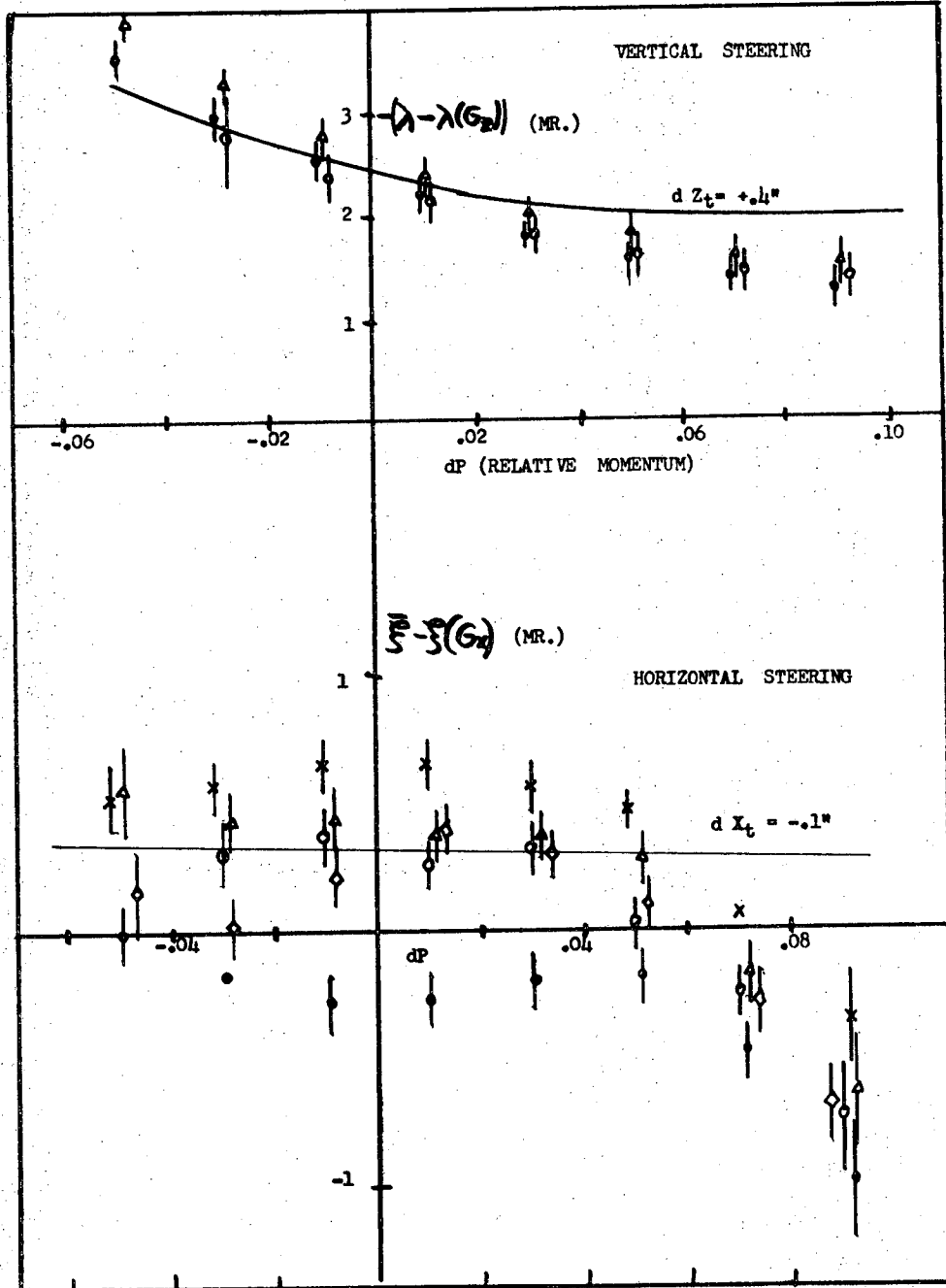


FIGURE 25

XBL 701-35

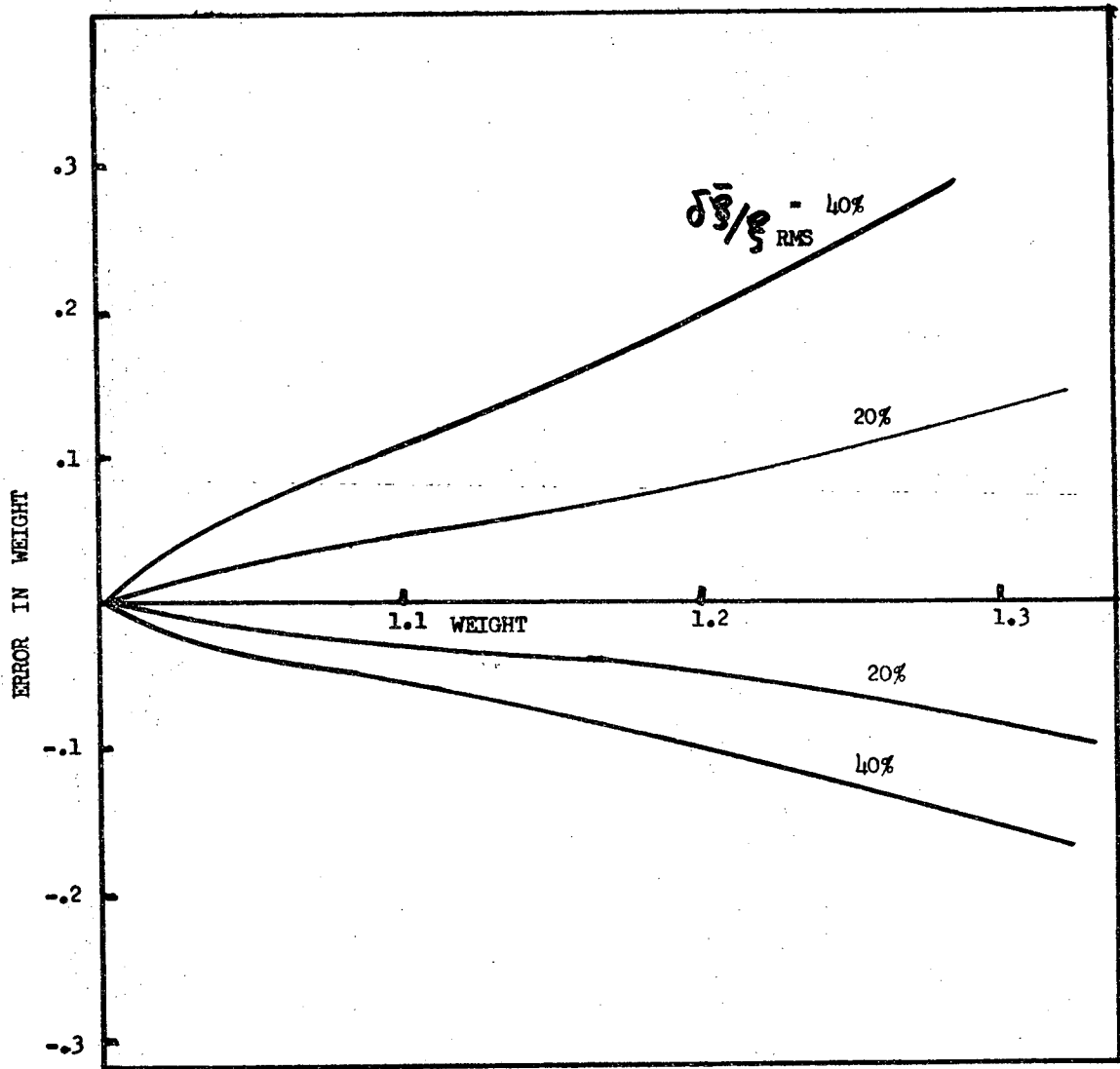


FIGURE 26

XBL 701-36

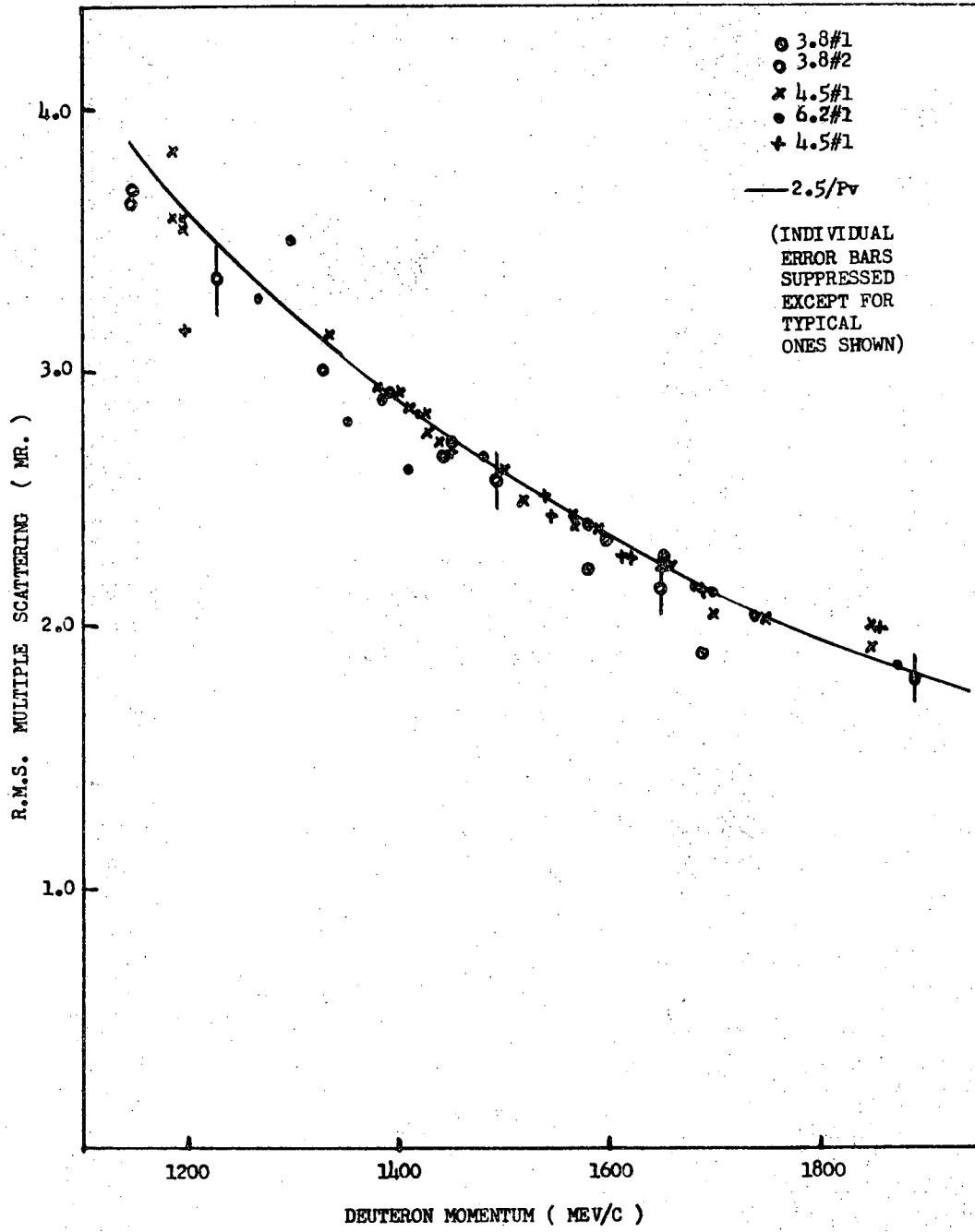
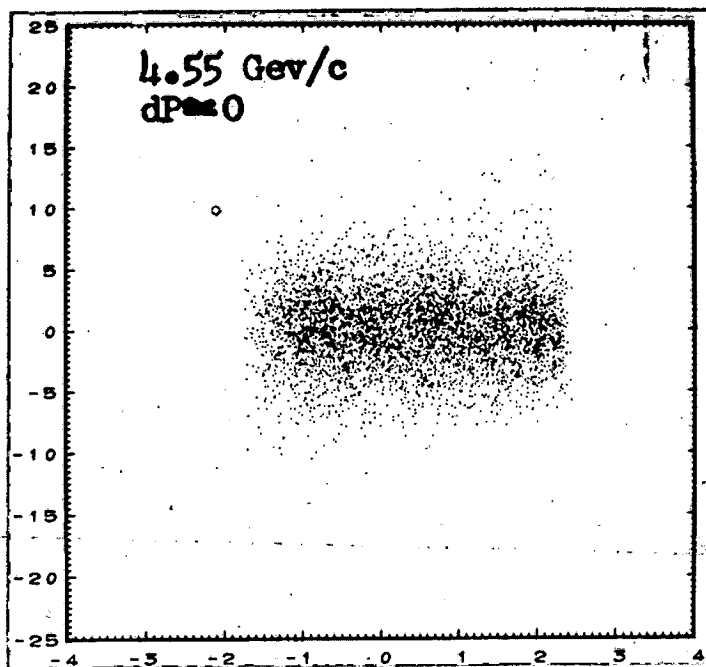


FIGURE 27

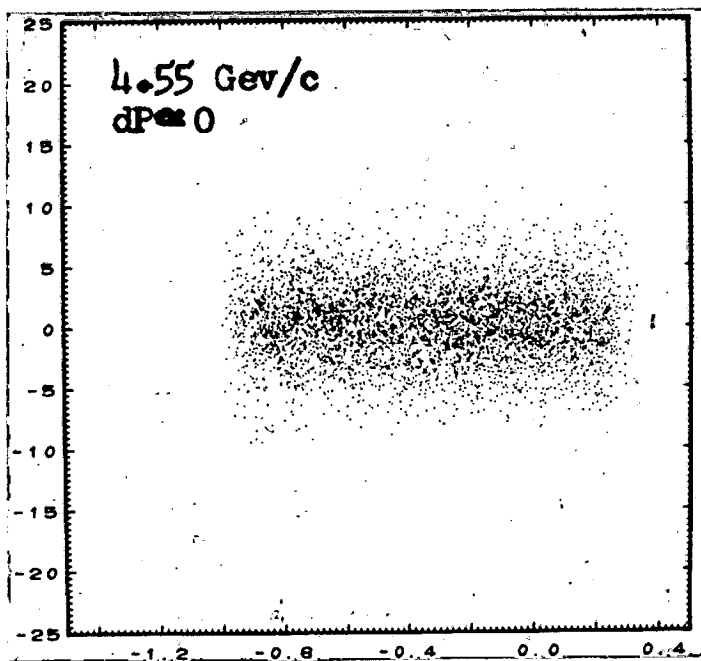
XBL 701-37

Hor. Slope Deviation (mr.)



X_s (inches)

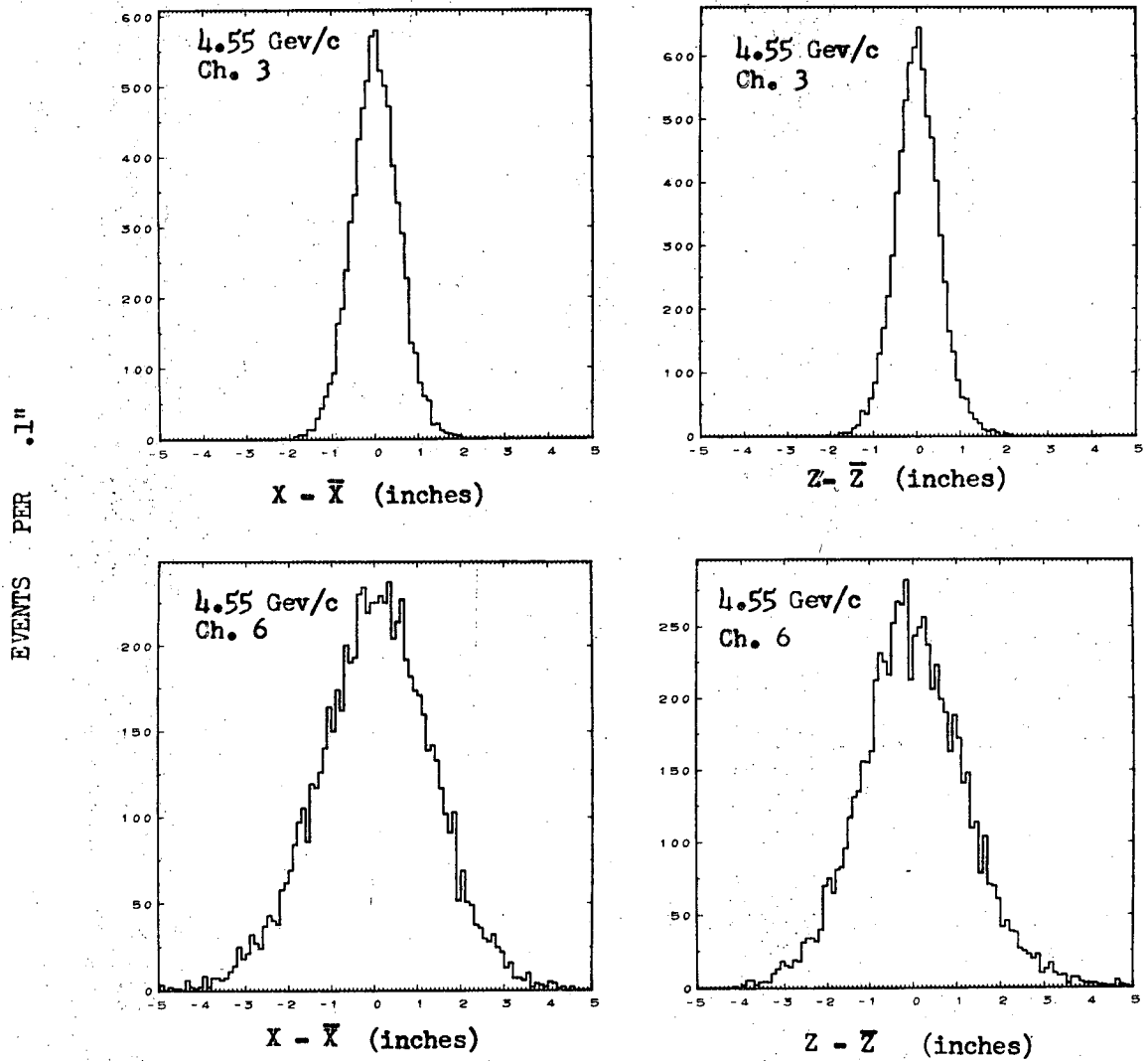
Vert. Slope Deviation (mr.)



Z_s (inches)

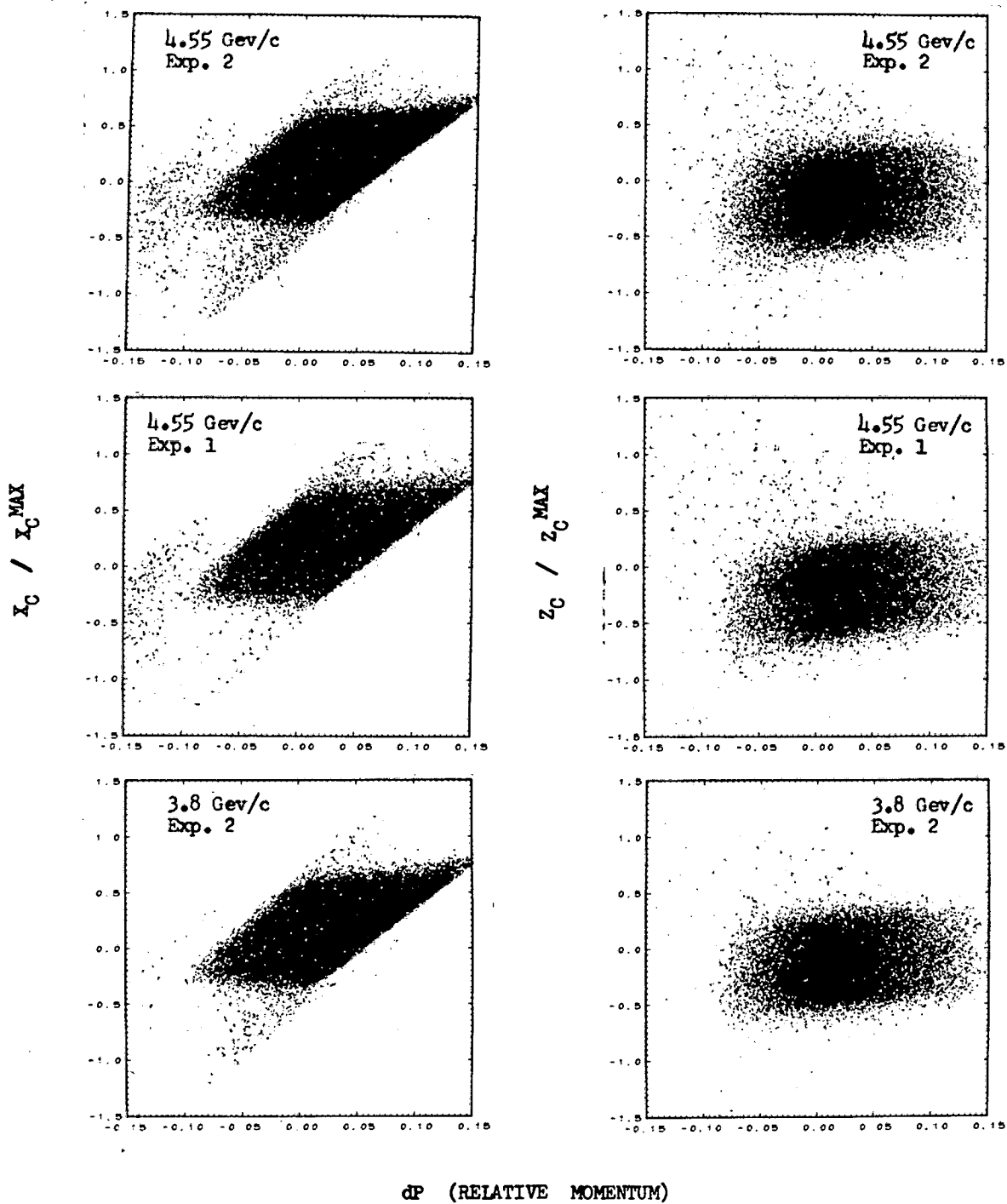
XBB 6911-7524

Fig. 28



XBL 6911-6619

FIGURE 29

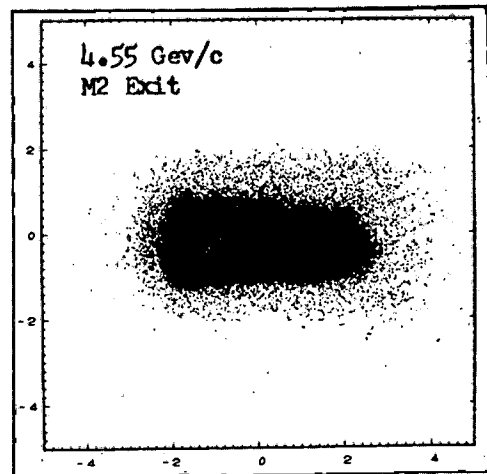
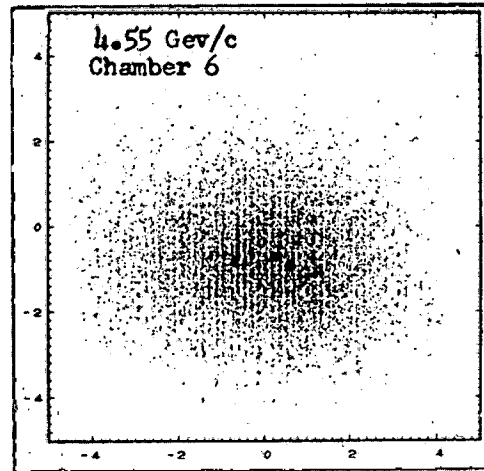
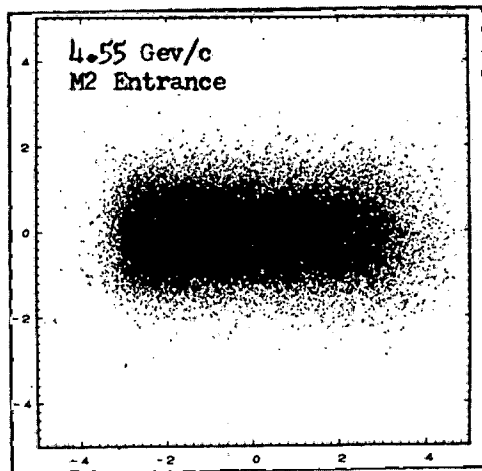
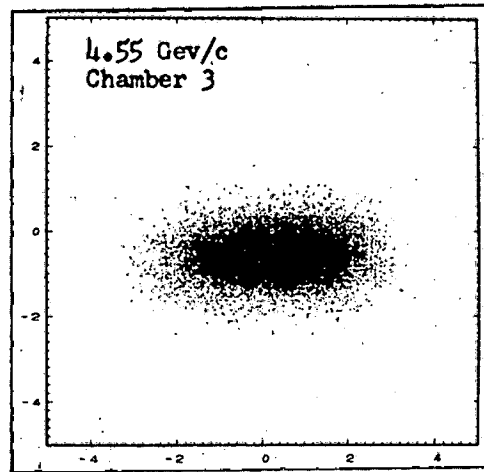
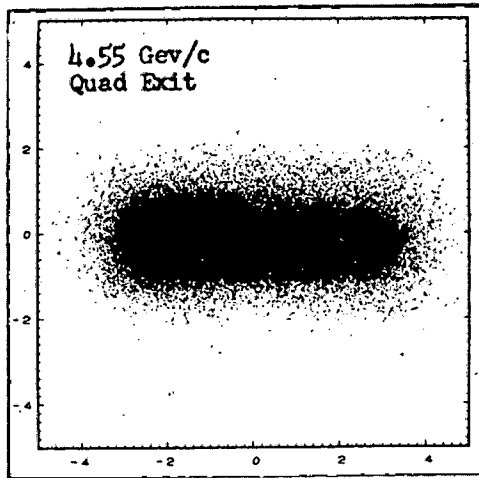


dP (RELATIVE MOMENTUM)

XBB 6911-7523

Fig. 30

Z COORDINATE (INCHES)

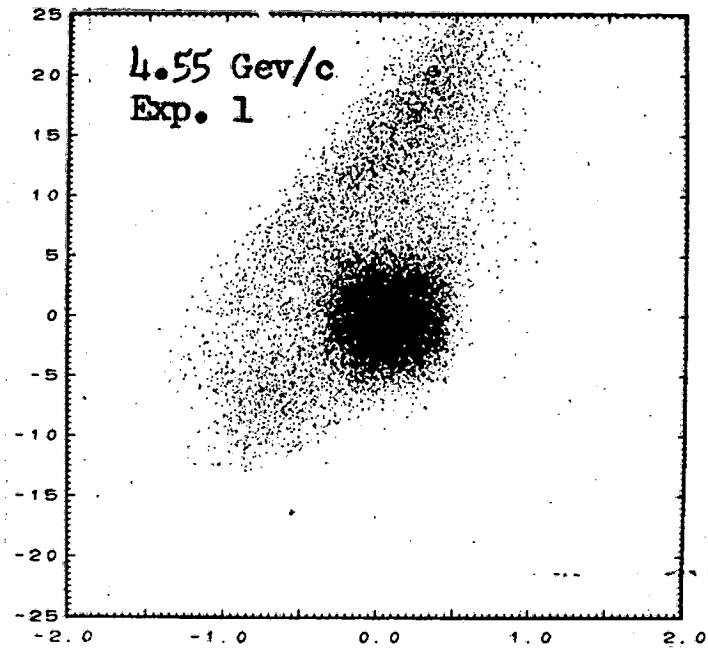
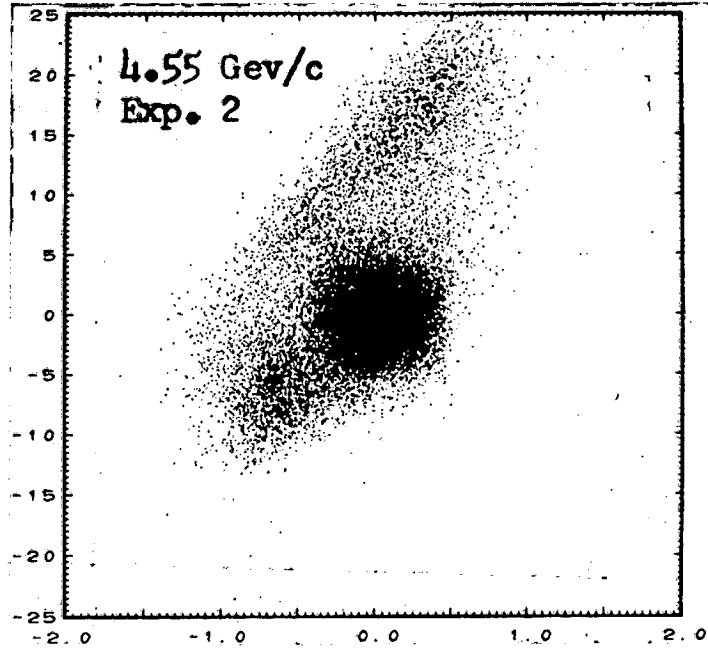


X COORDINATE (INCHES)

XBB 6911-7521

Fig. 31

HORIZONTAL SLOPE DEVIATION (MR.)



x_C/x_C^{MAX}

XBB 6911-7520

Fig. 32

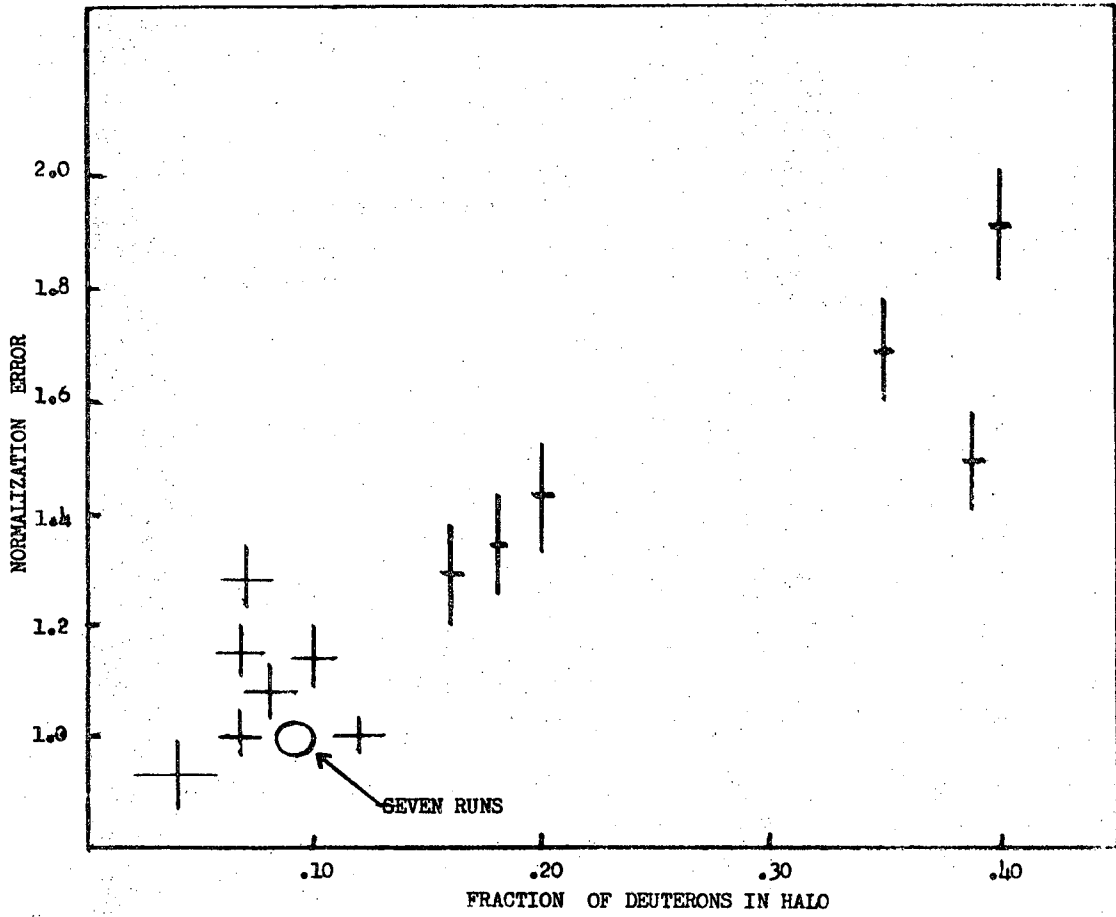


FIGURE 33

XBL 701-38

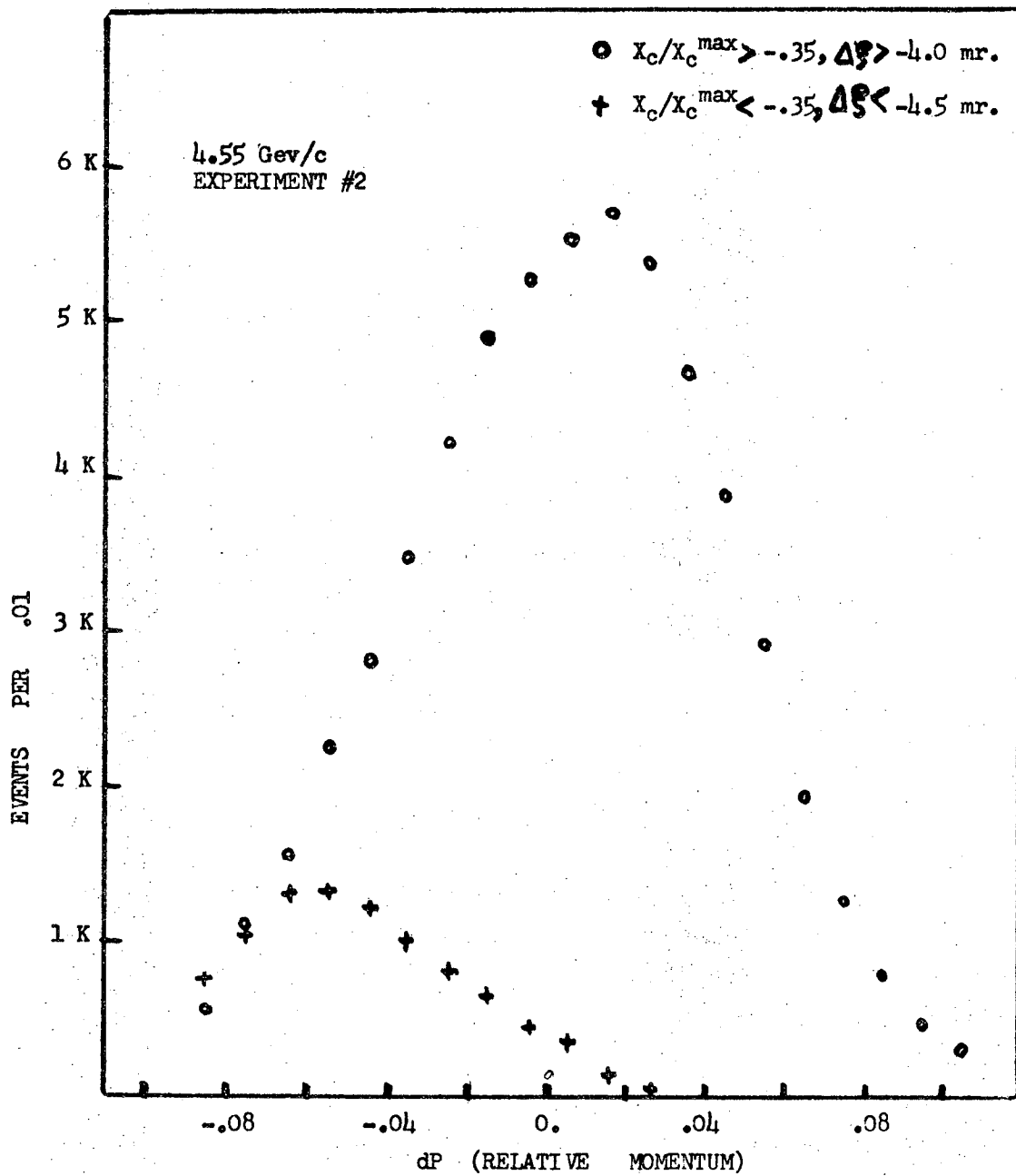


FIGURE 34

XBL 701-39

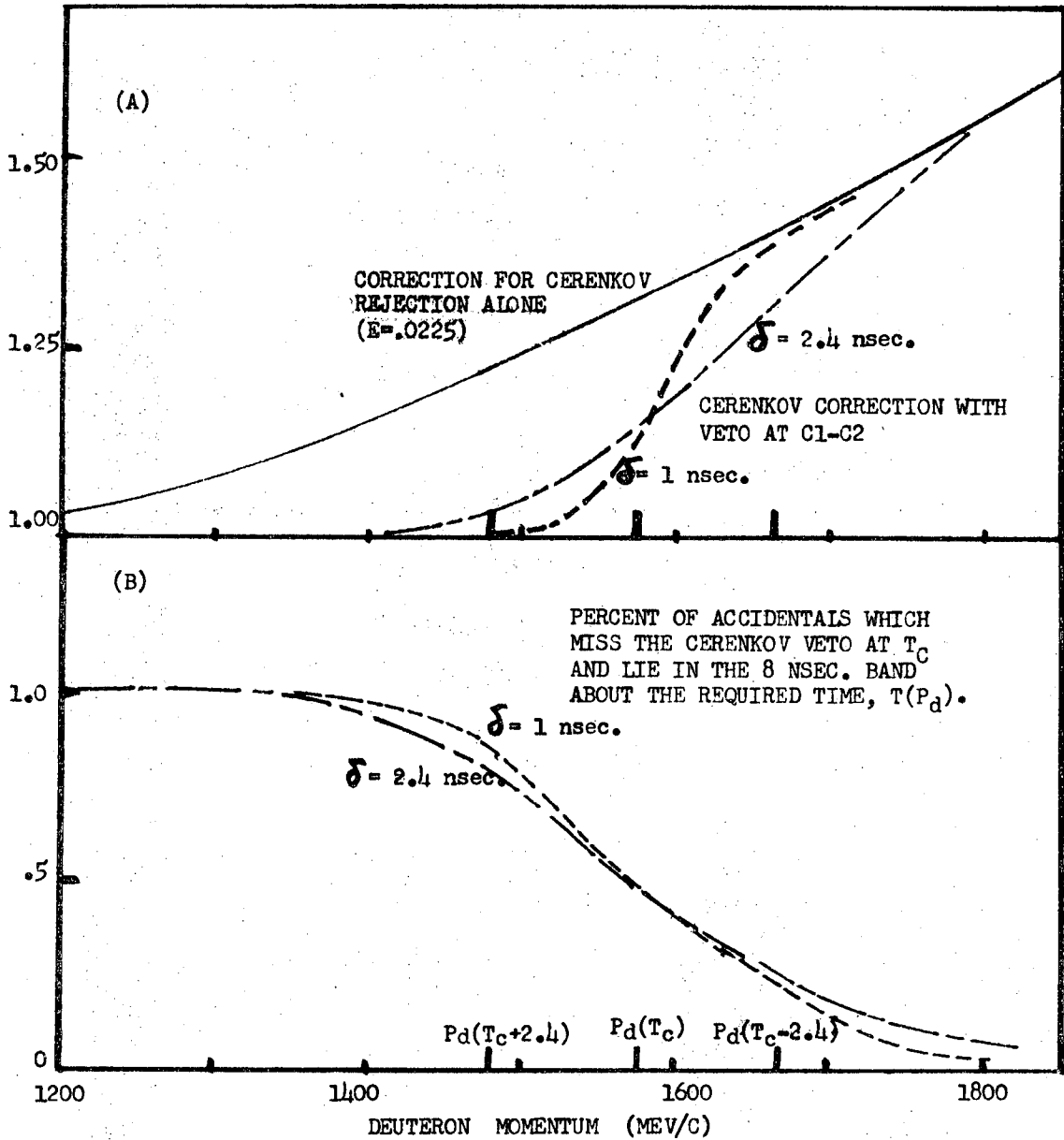


FIGURE 35

XBL 701-40

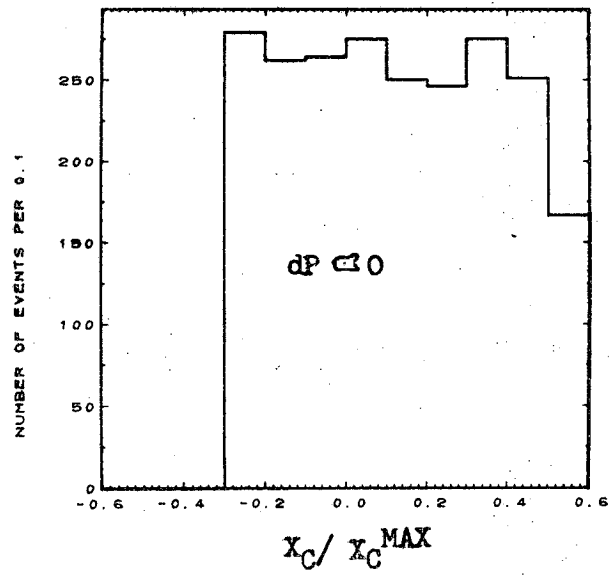


FIGURE 36

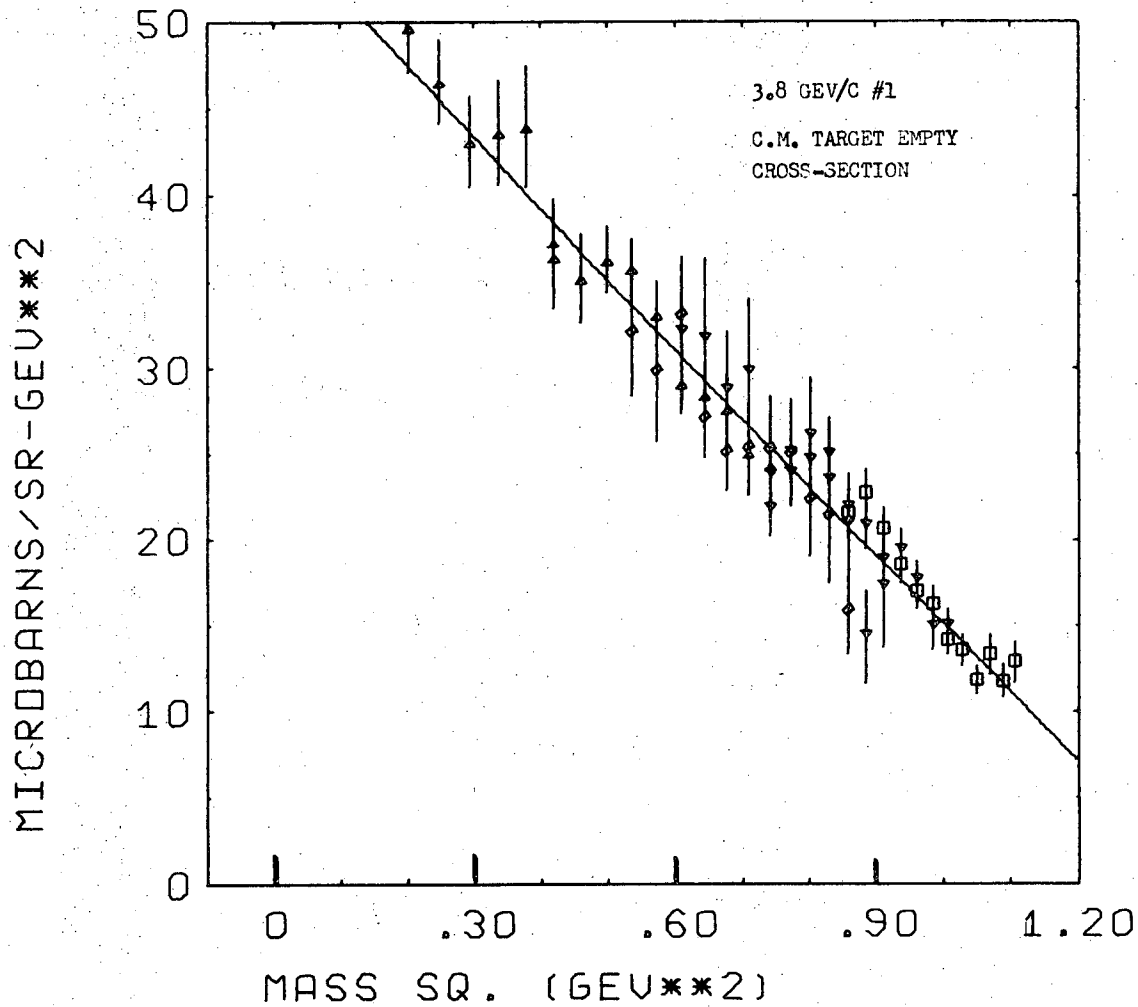


FIGURE 37

XBL 701-41

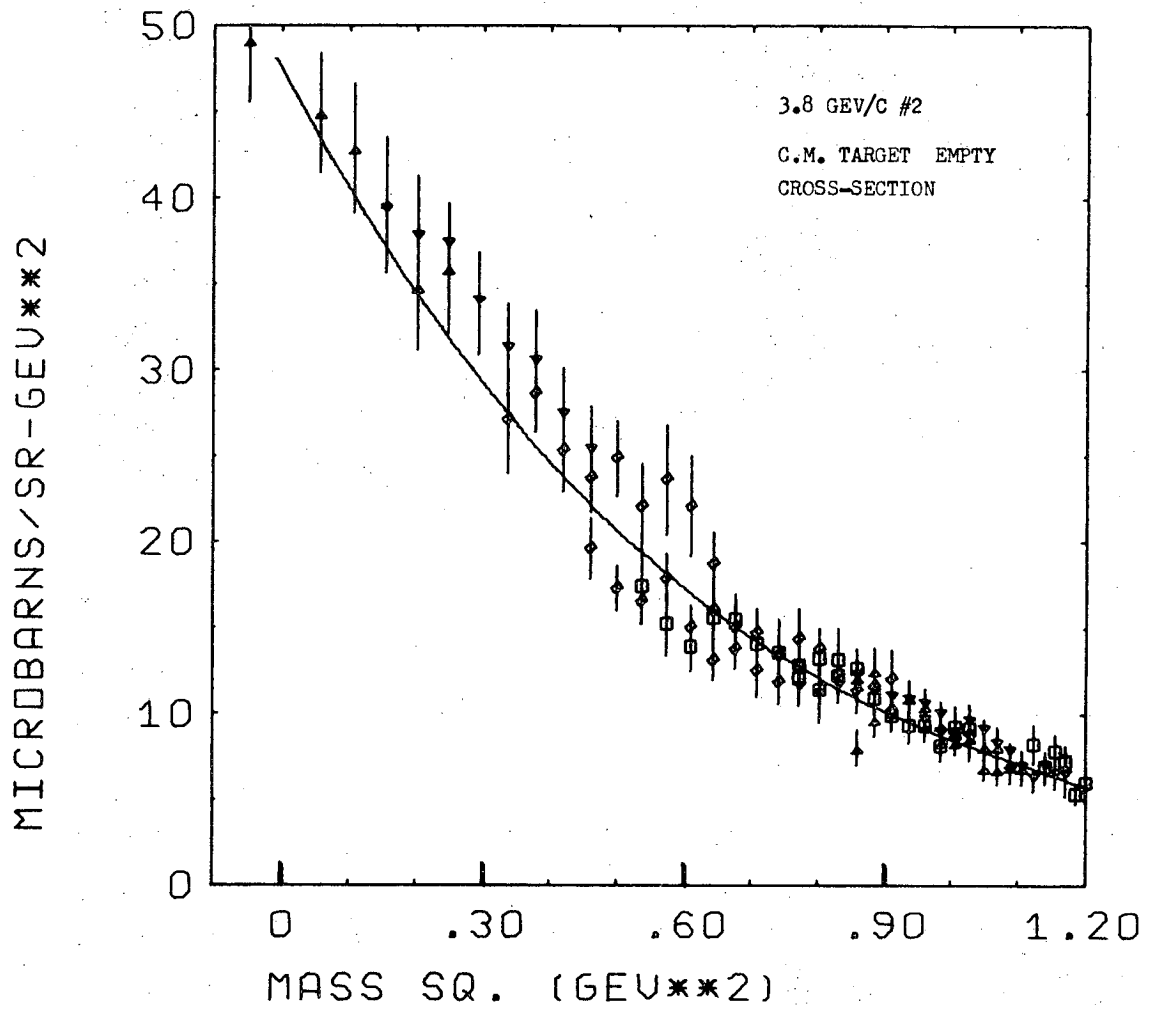


FIGURE 38

XBL 701-42

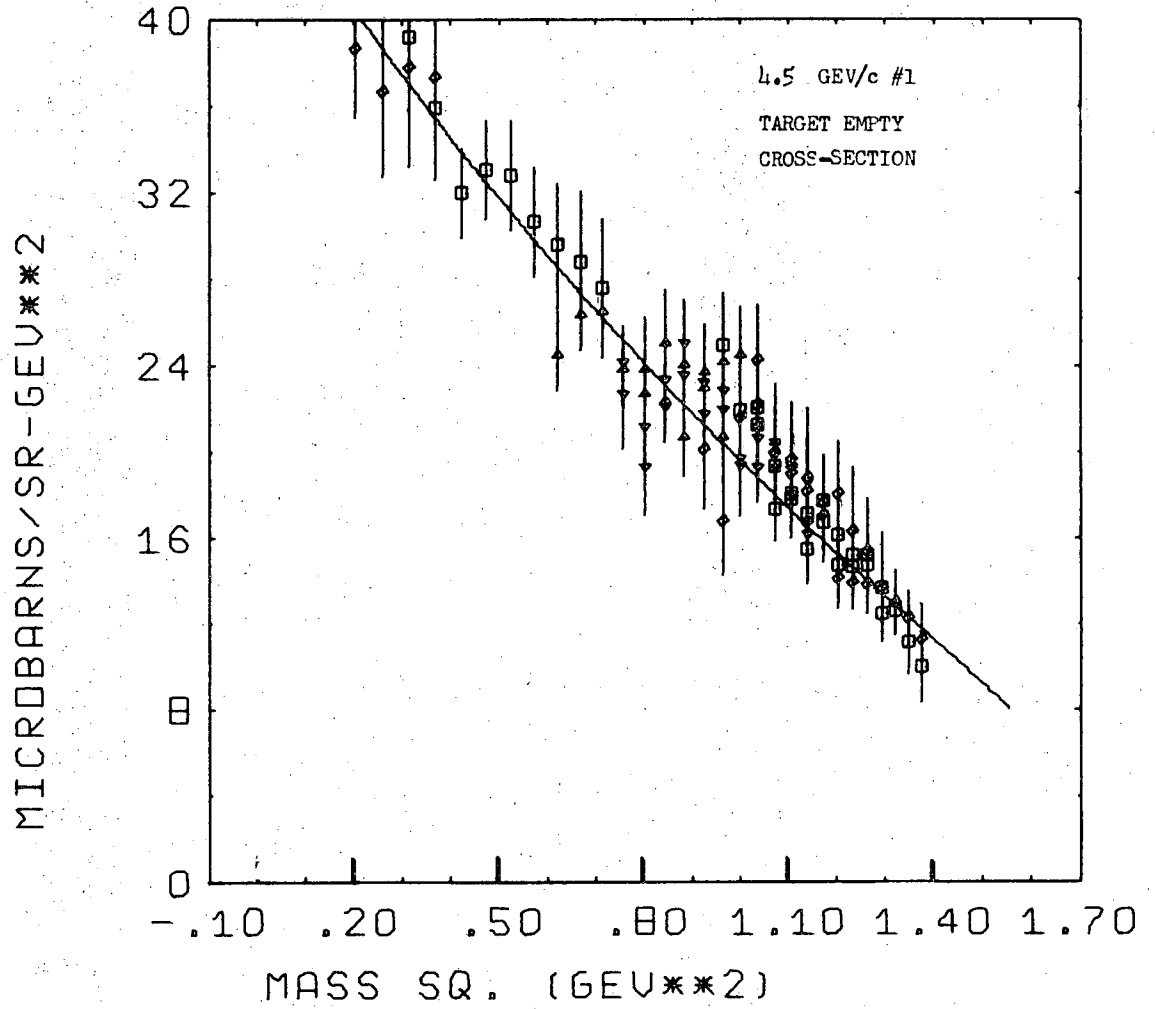


FIGURE 39

XBL 701-43

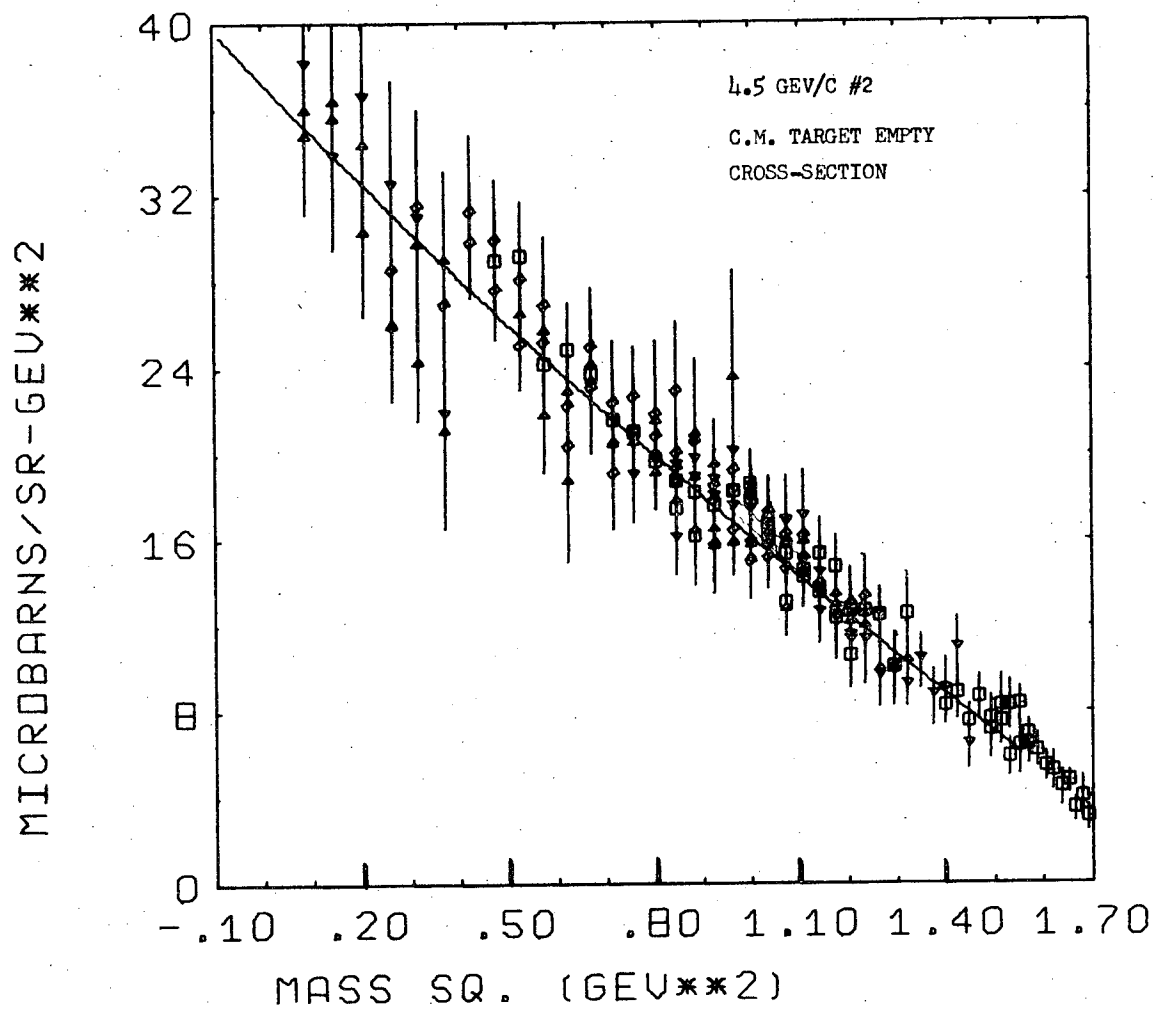


FIGURE 40

XBL 701-44

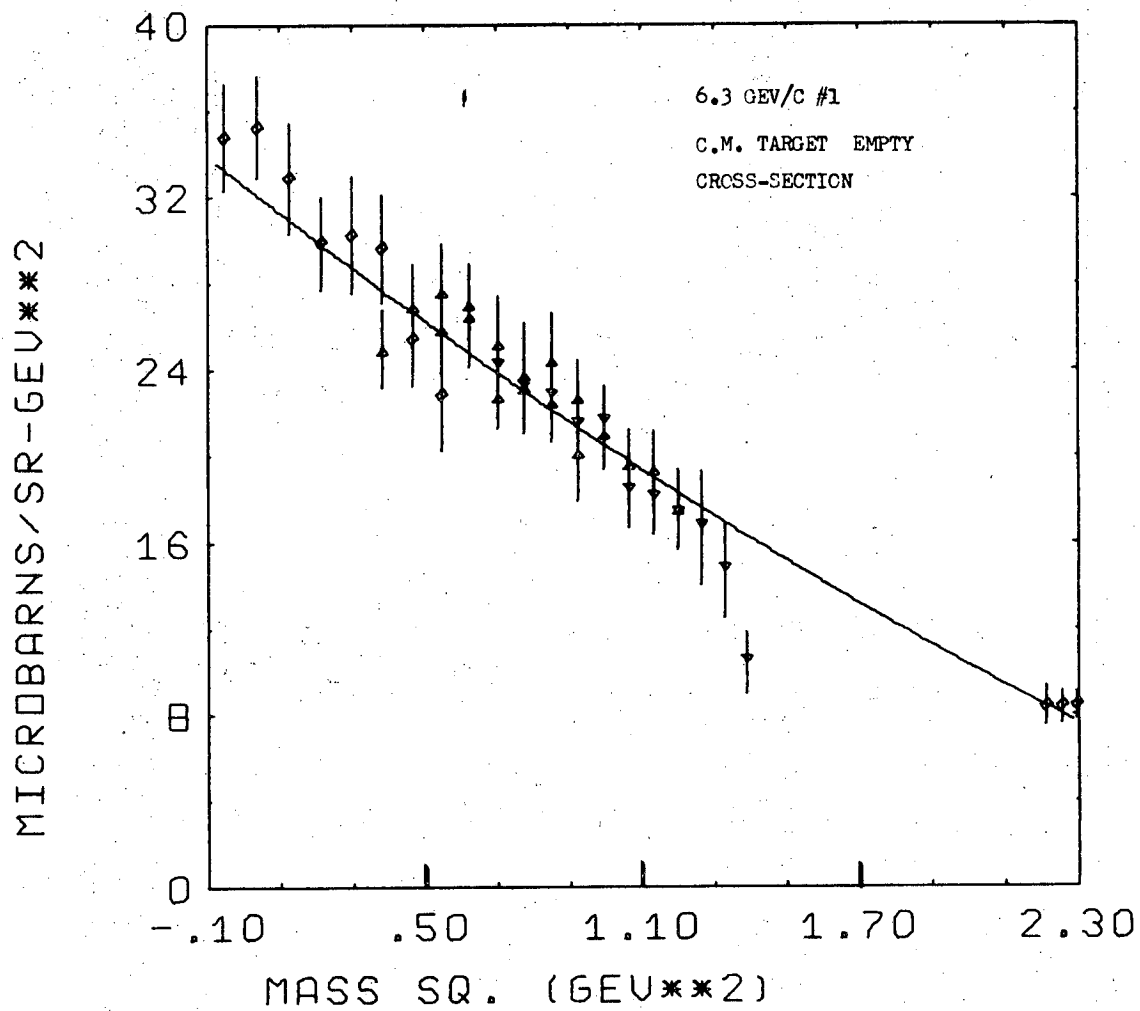


FIGURE 41

XBL 701-45

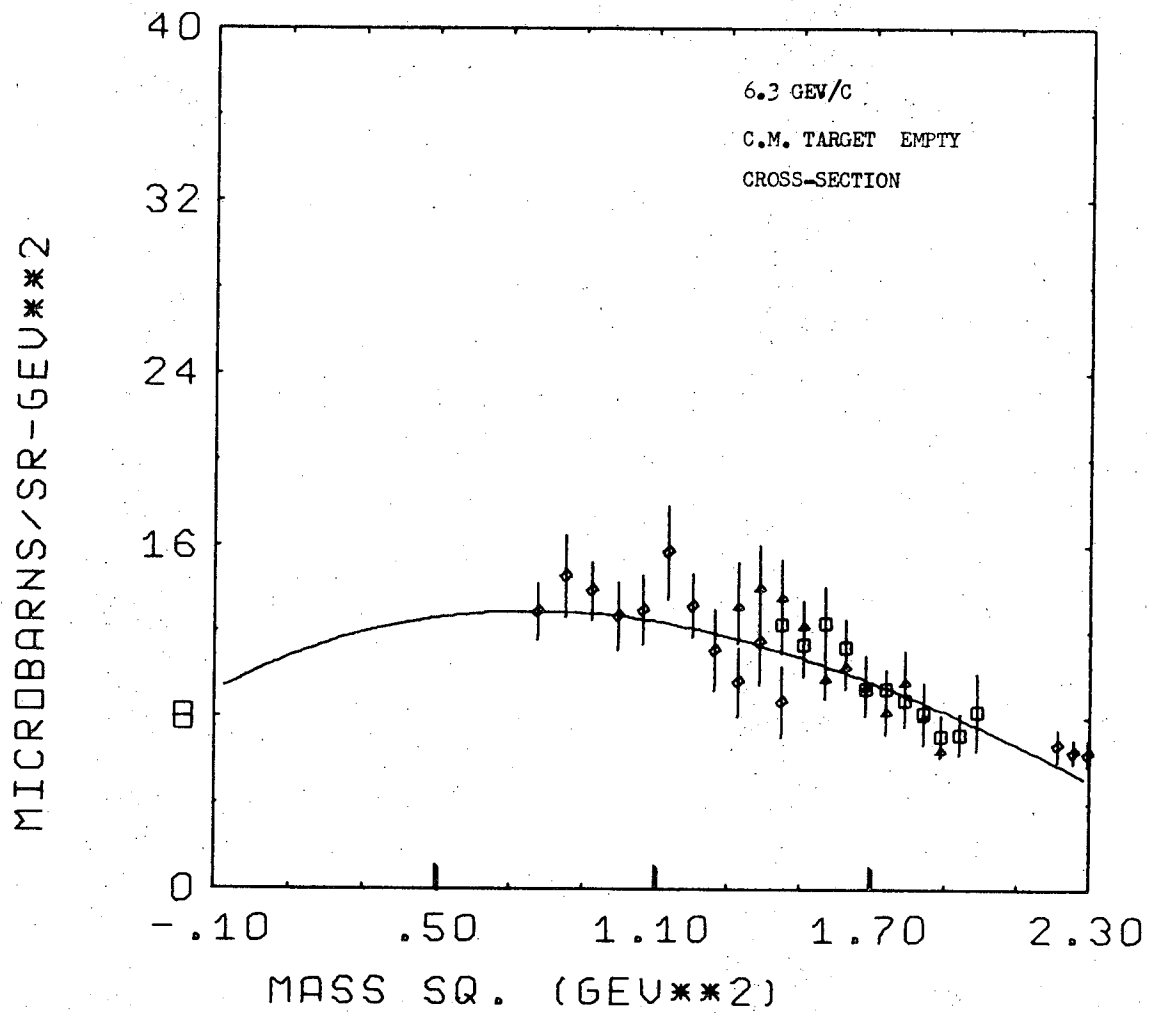


FIGURE 42

XBL 701-46

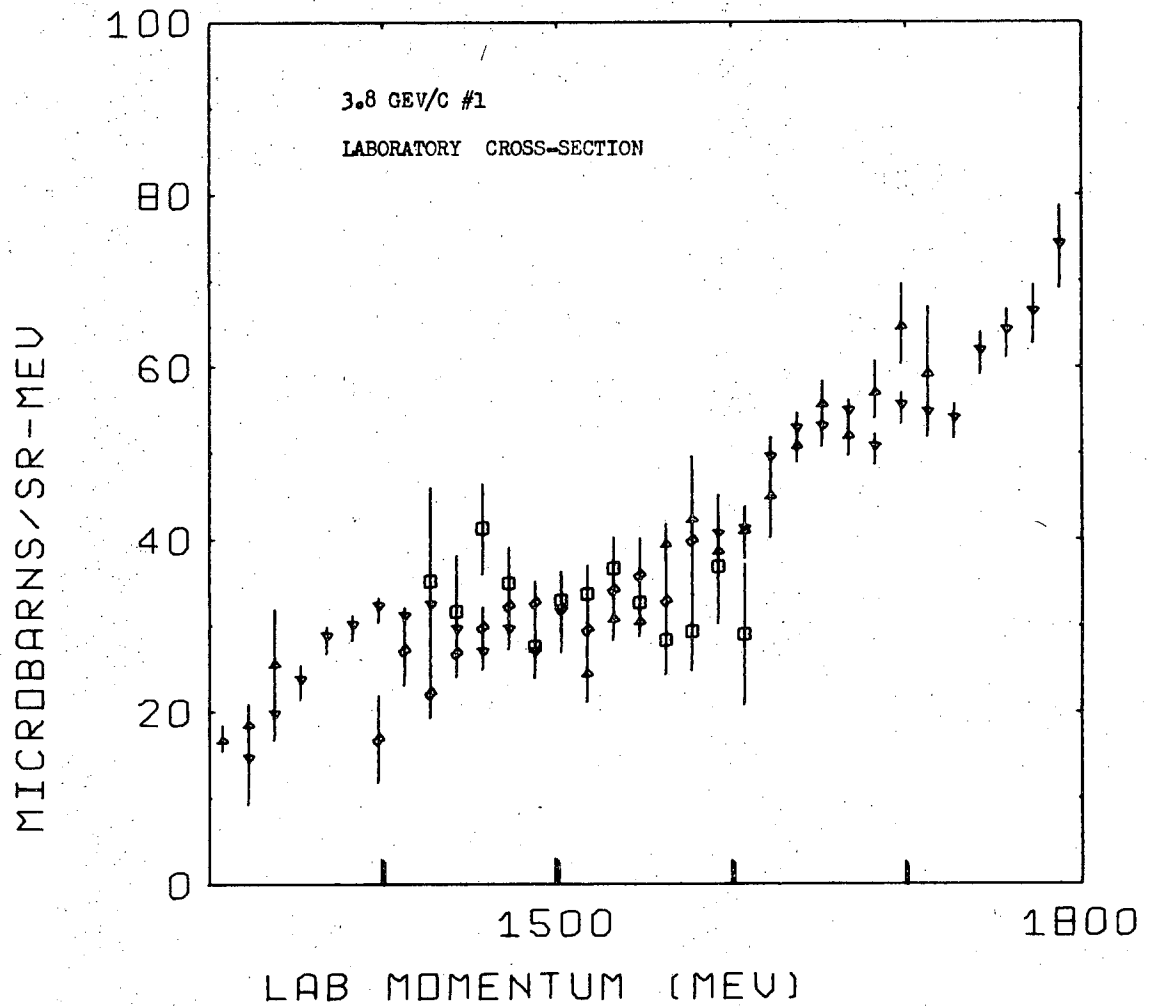


FIGURE 43

XBL 701-47

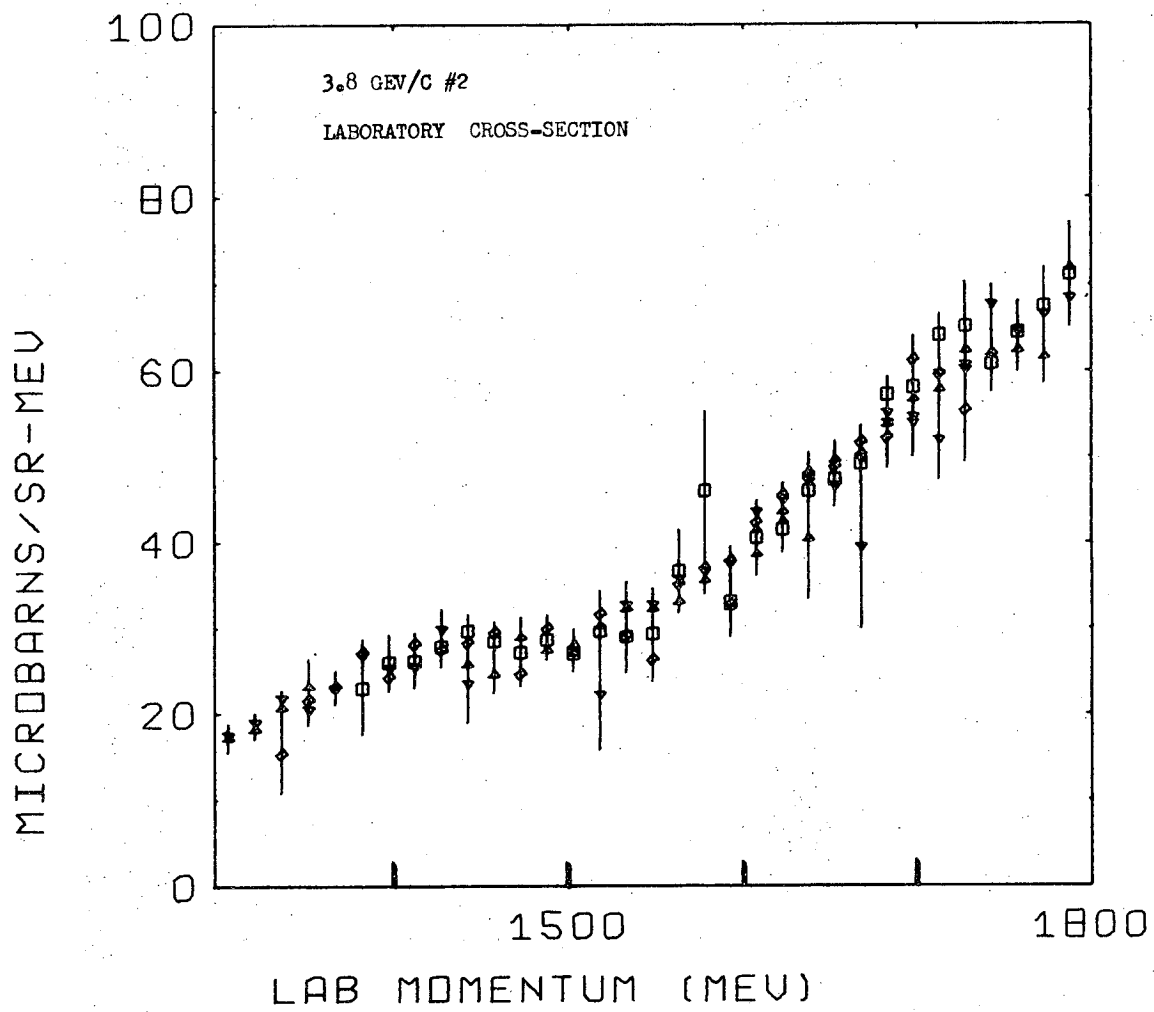


FIGURE 44

XBL 701-48

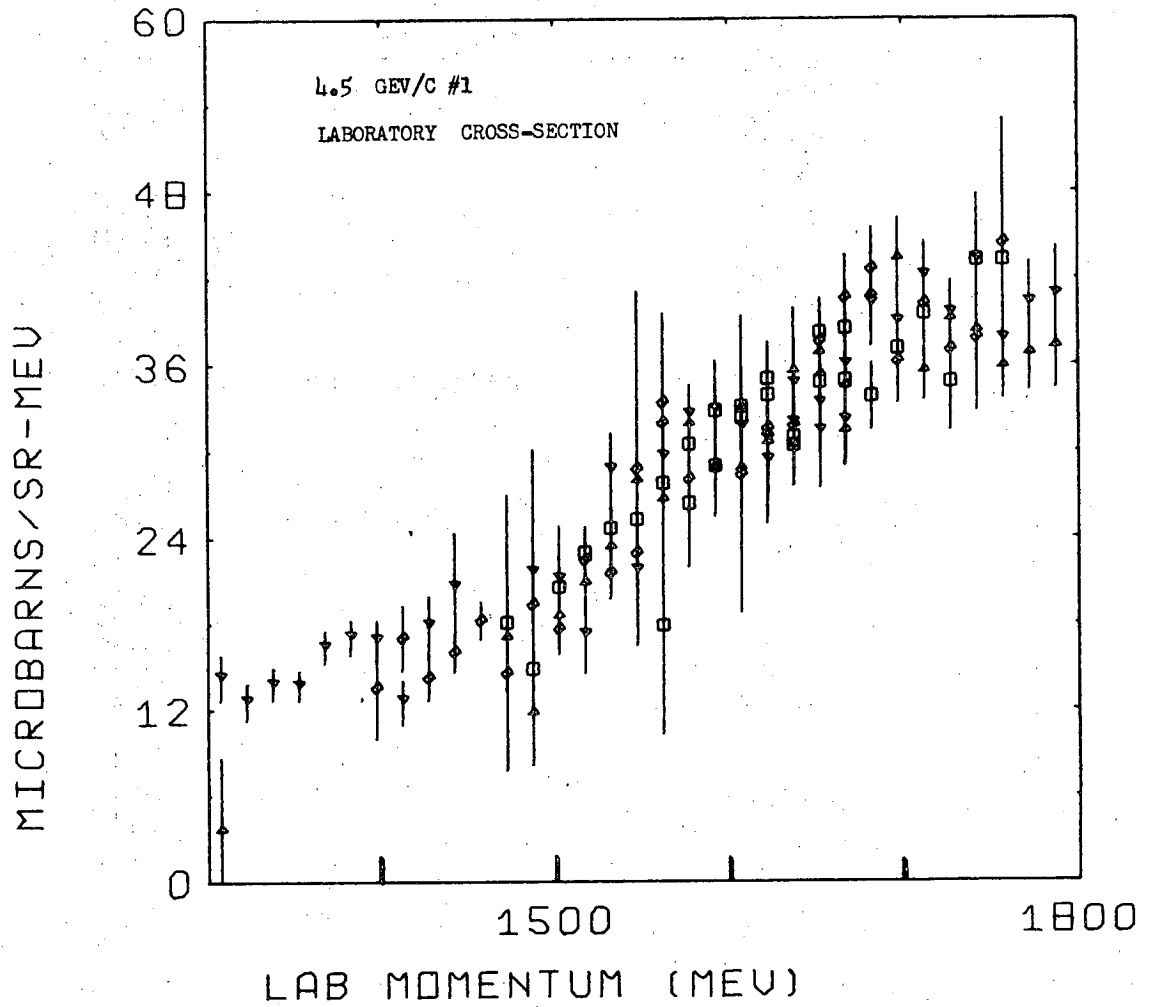


FIGURE 45

XBL 701-49

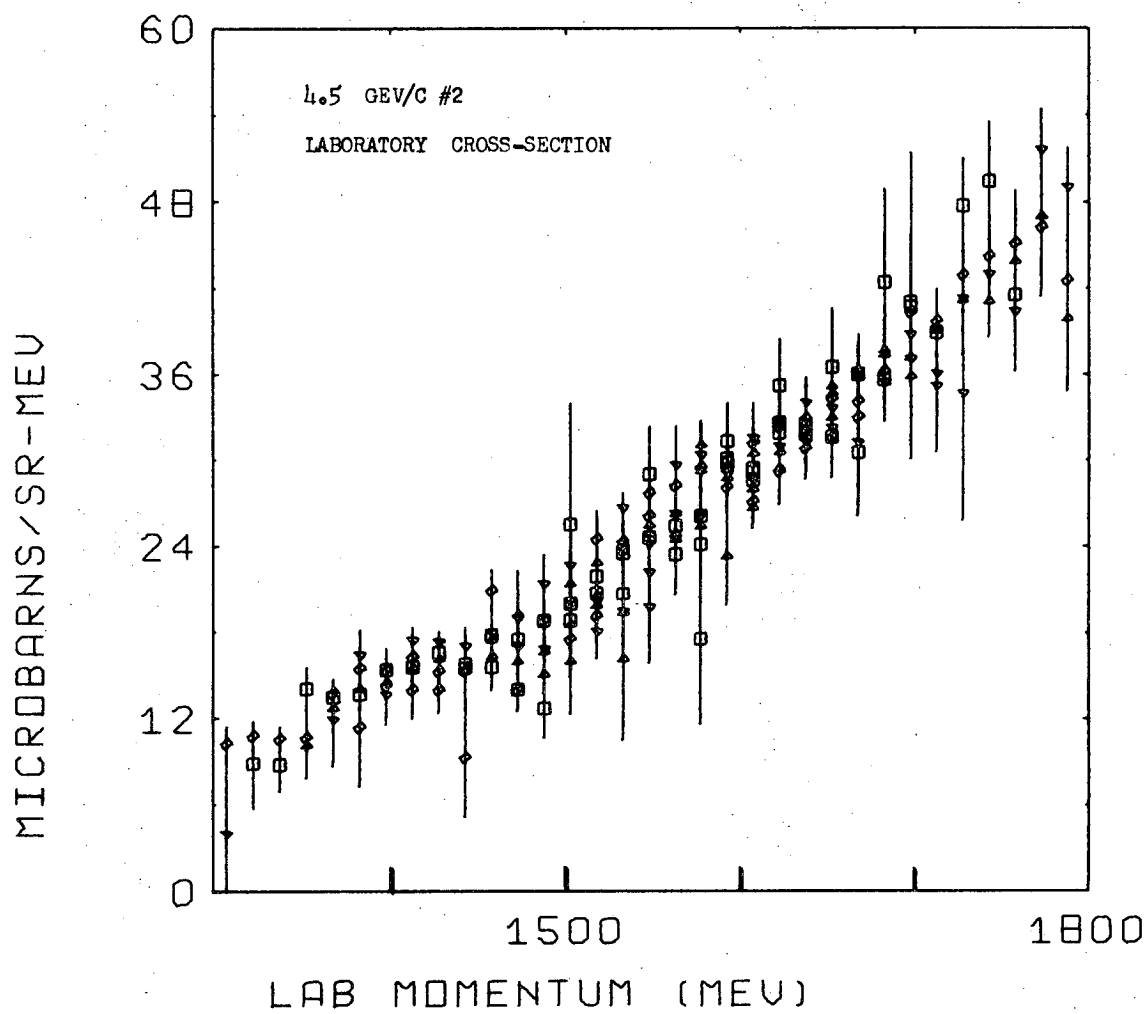


FIGURE 46

XBL 701-50

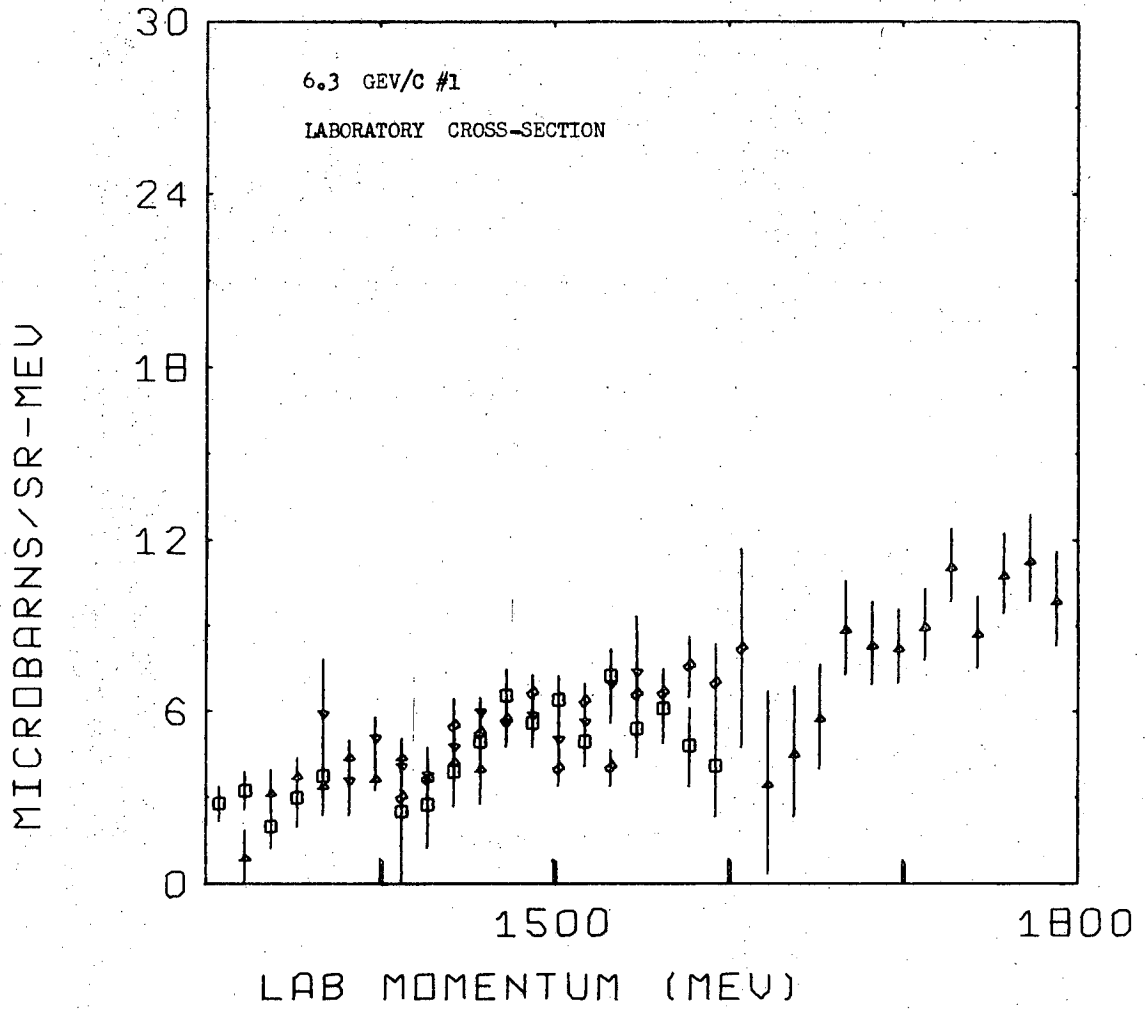


FIGURE 47

XBL 701-51

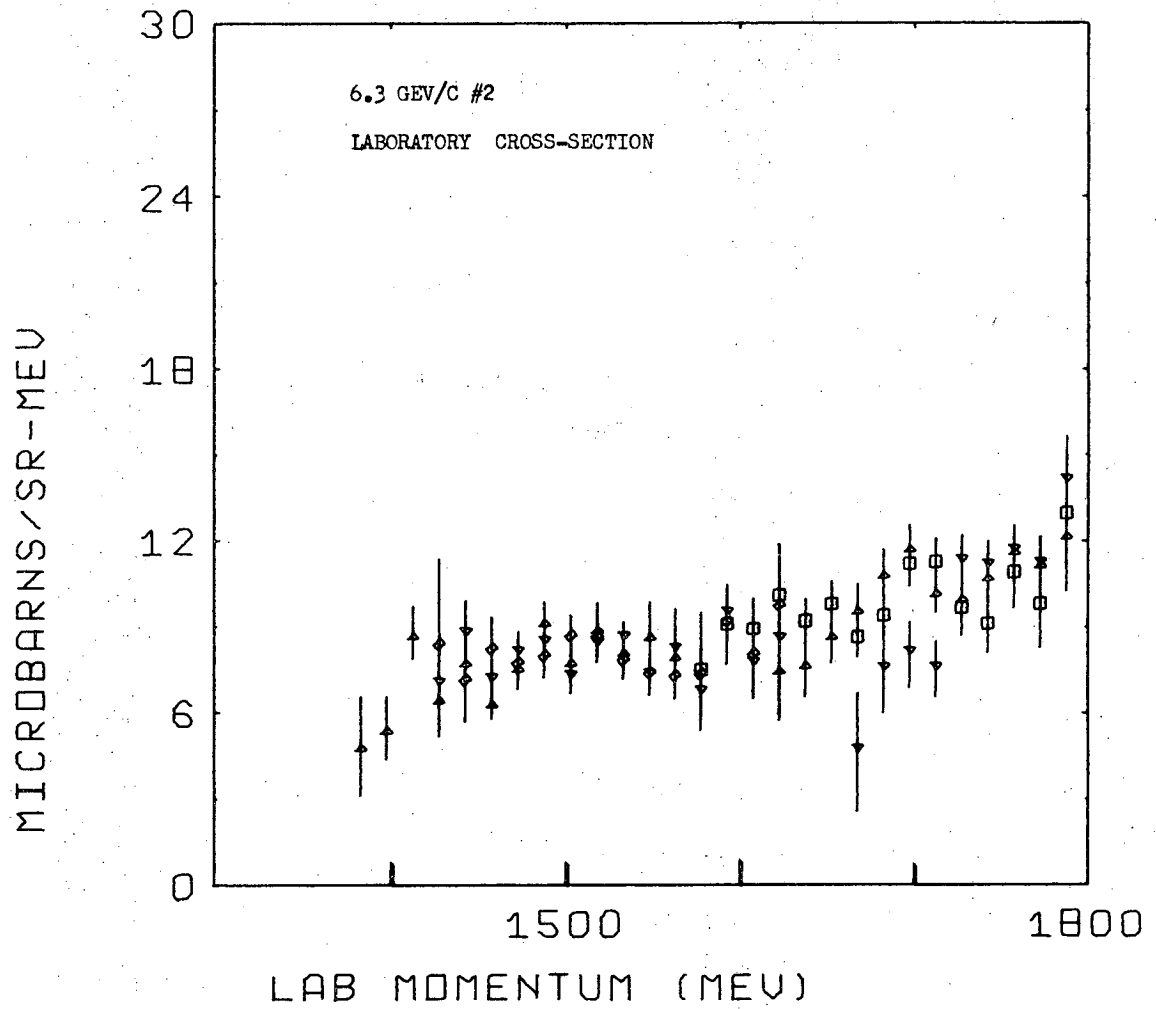


FIGURE 40

XBL 701-52

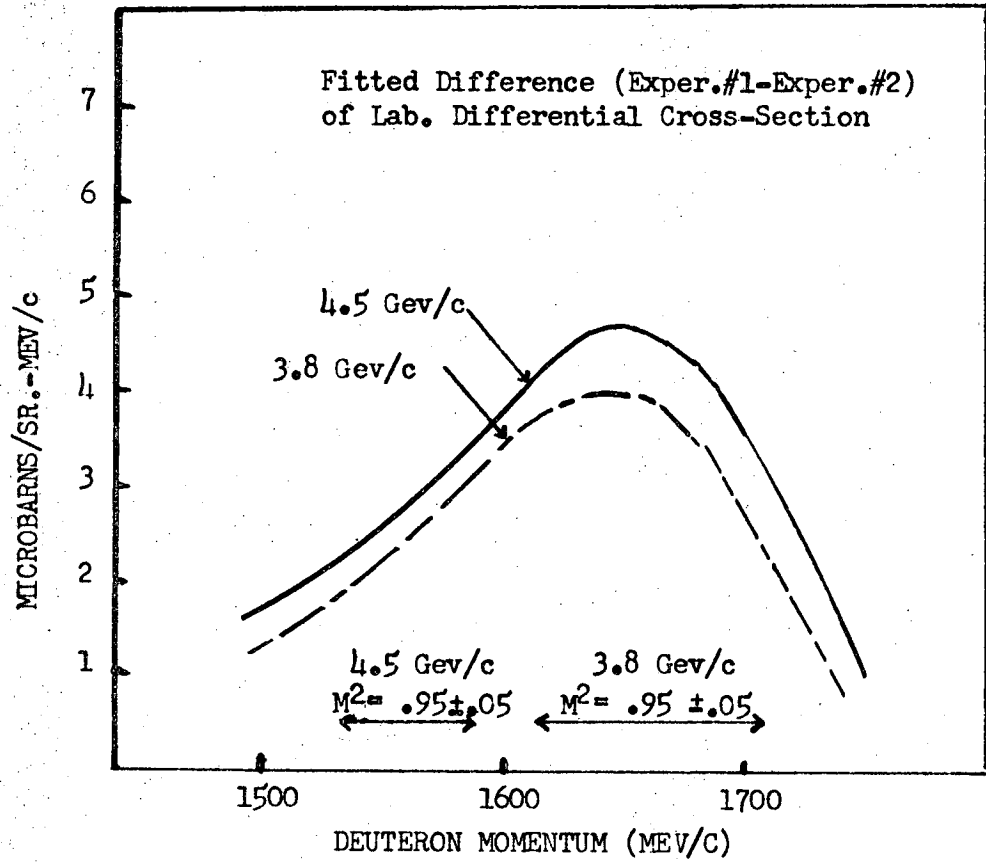


FIGURE 49

XBL 701-53

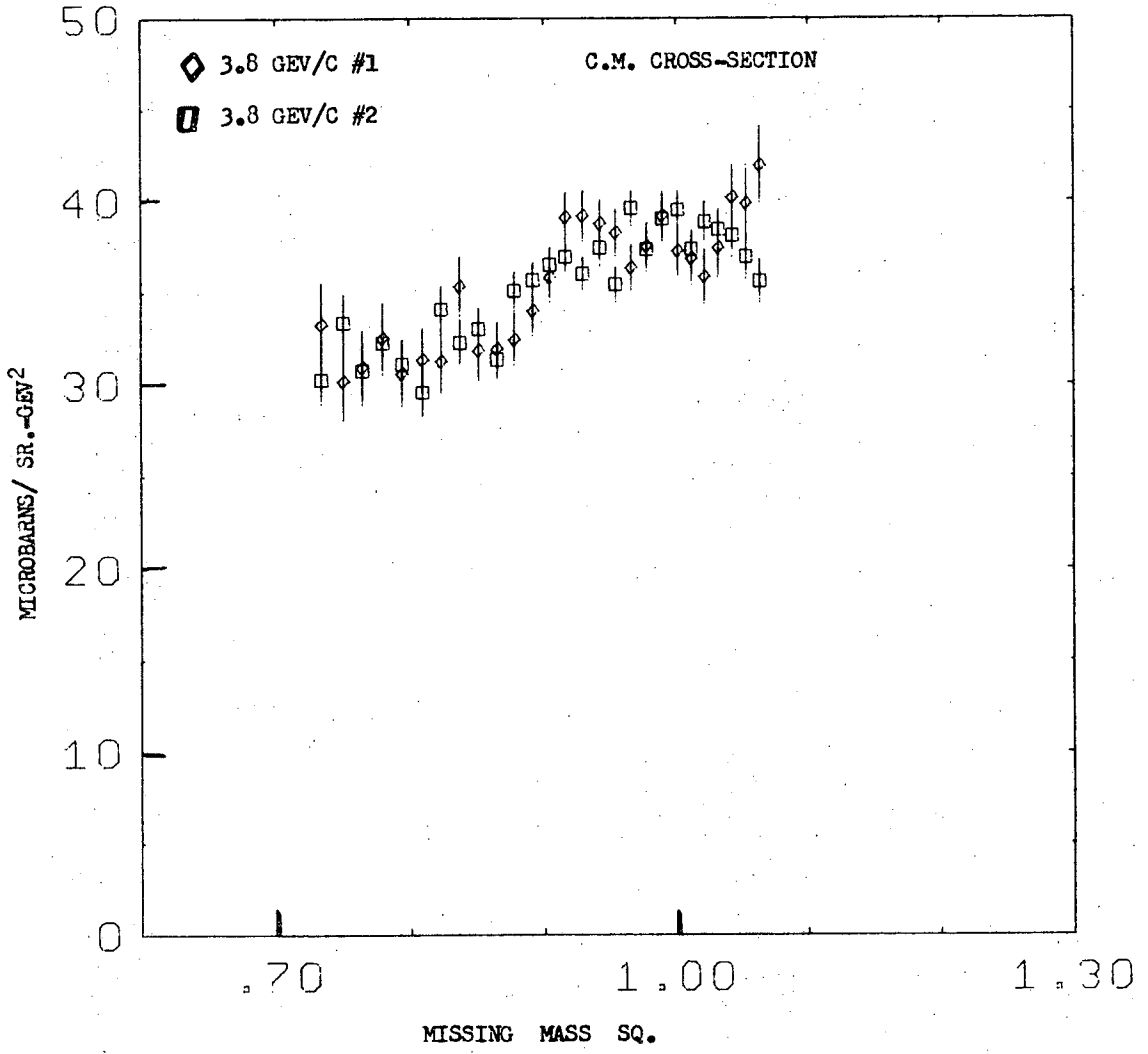


FIGURE 50

XBL 701-54

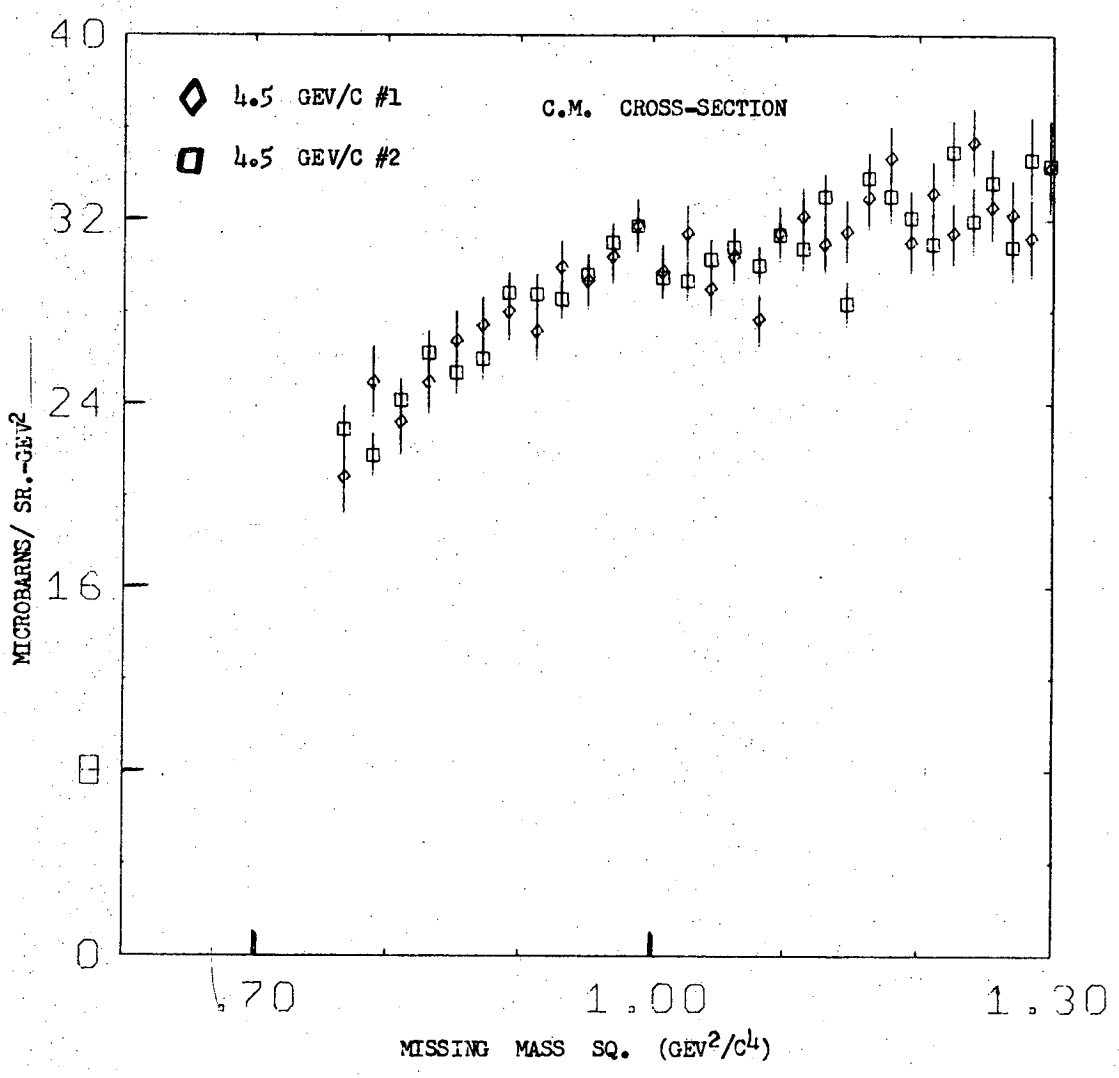


FIGURE 51

XBL 701-55

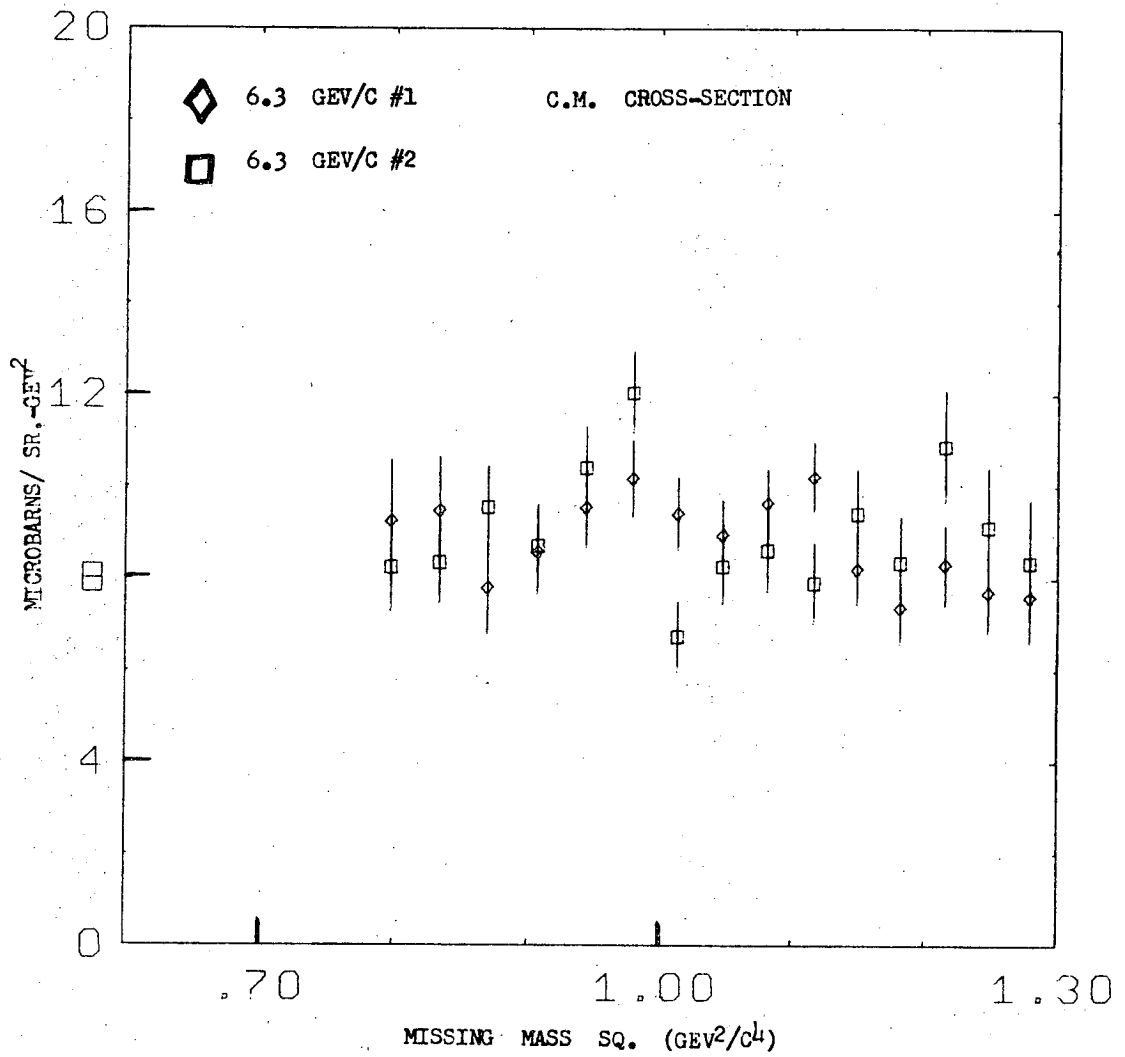


FIGURE 52

XBL 701-56

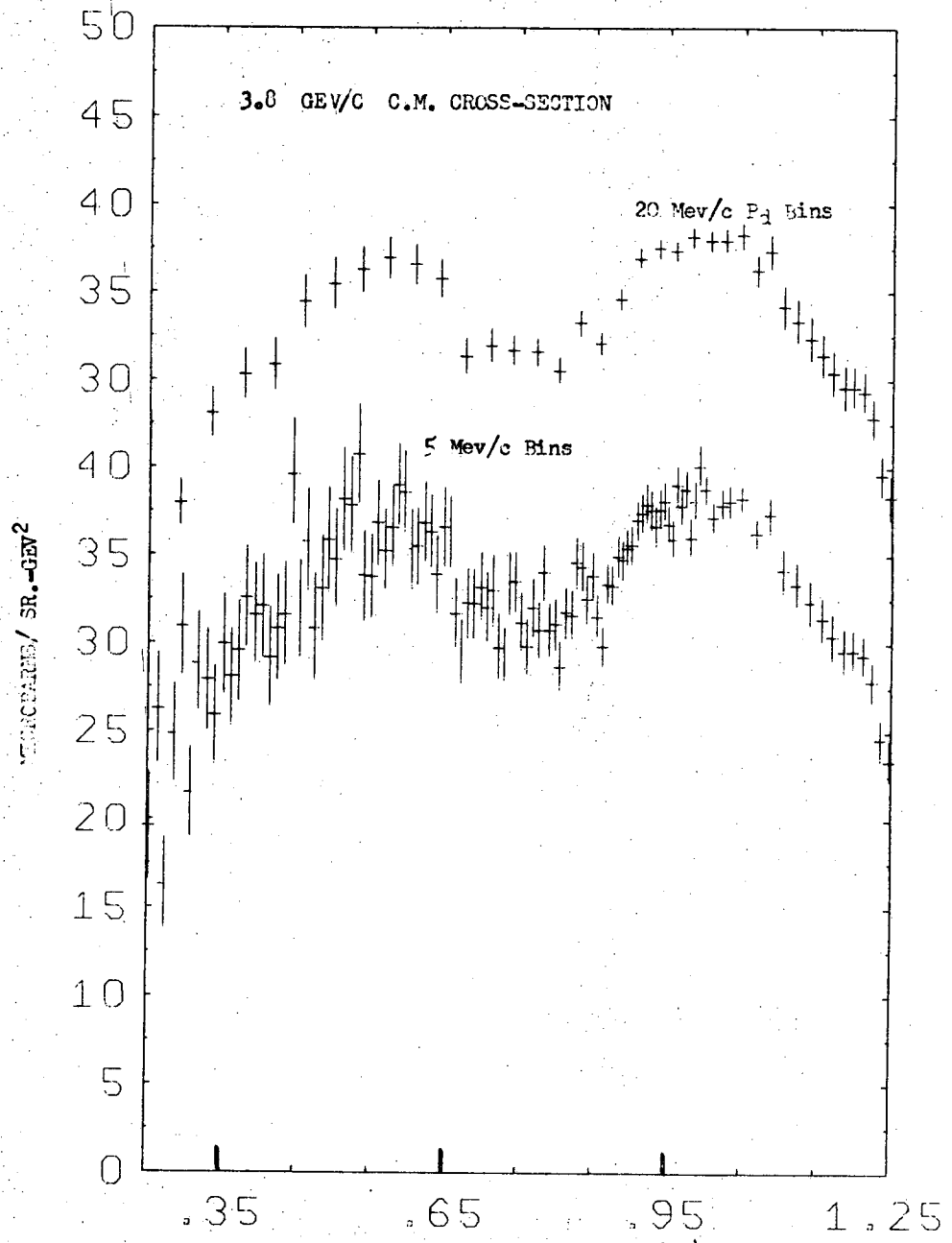


FIGURE 53

XBL 701-57

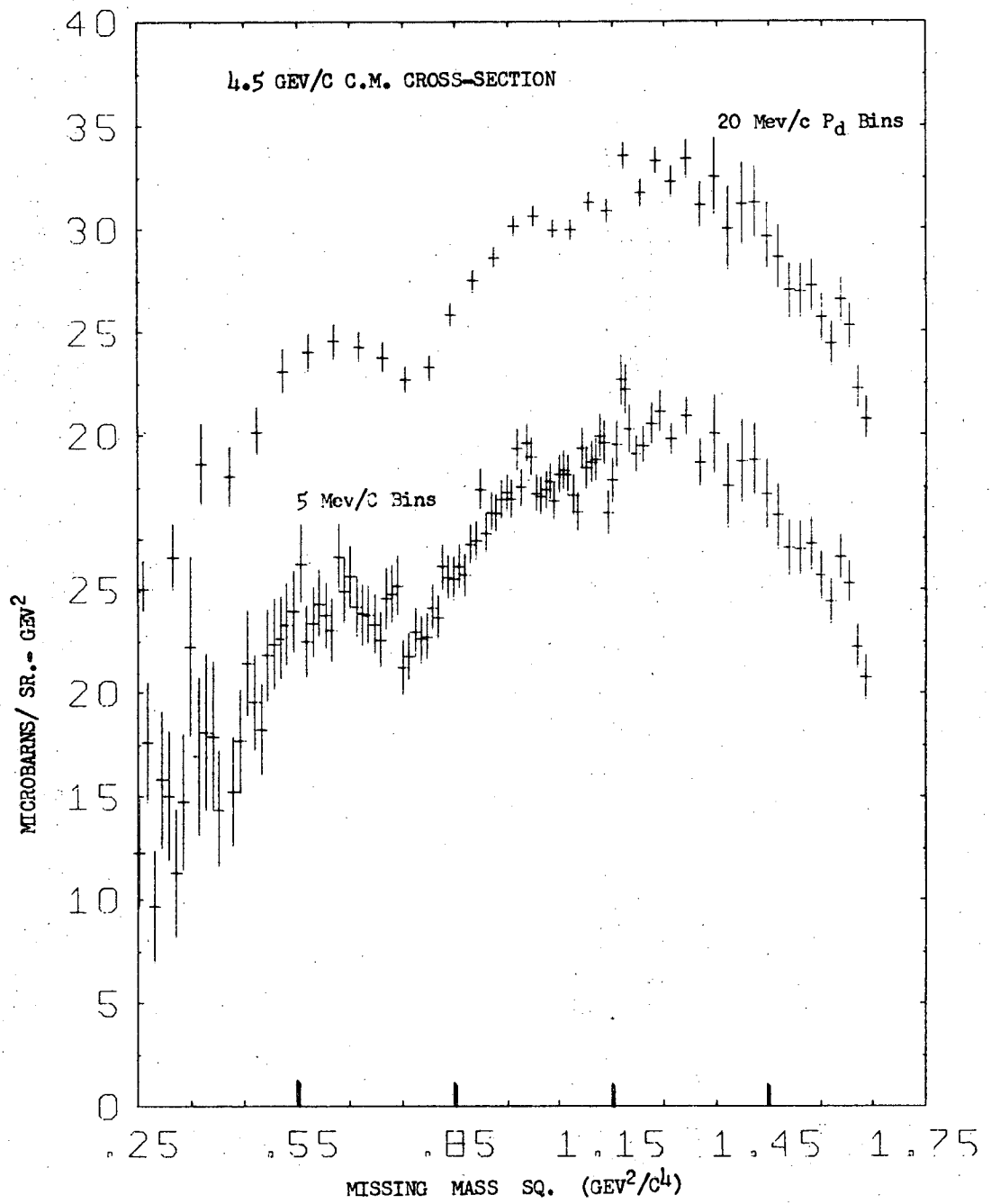


FIGURE 54

XBL 701-58

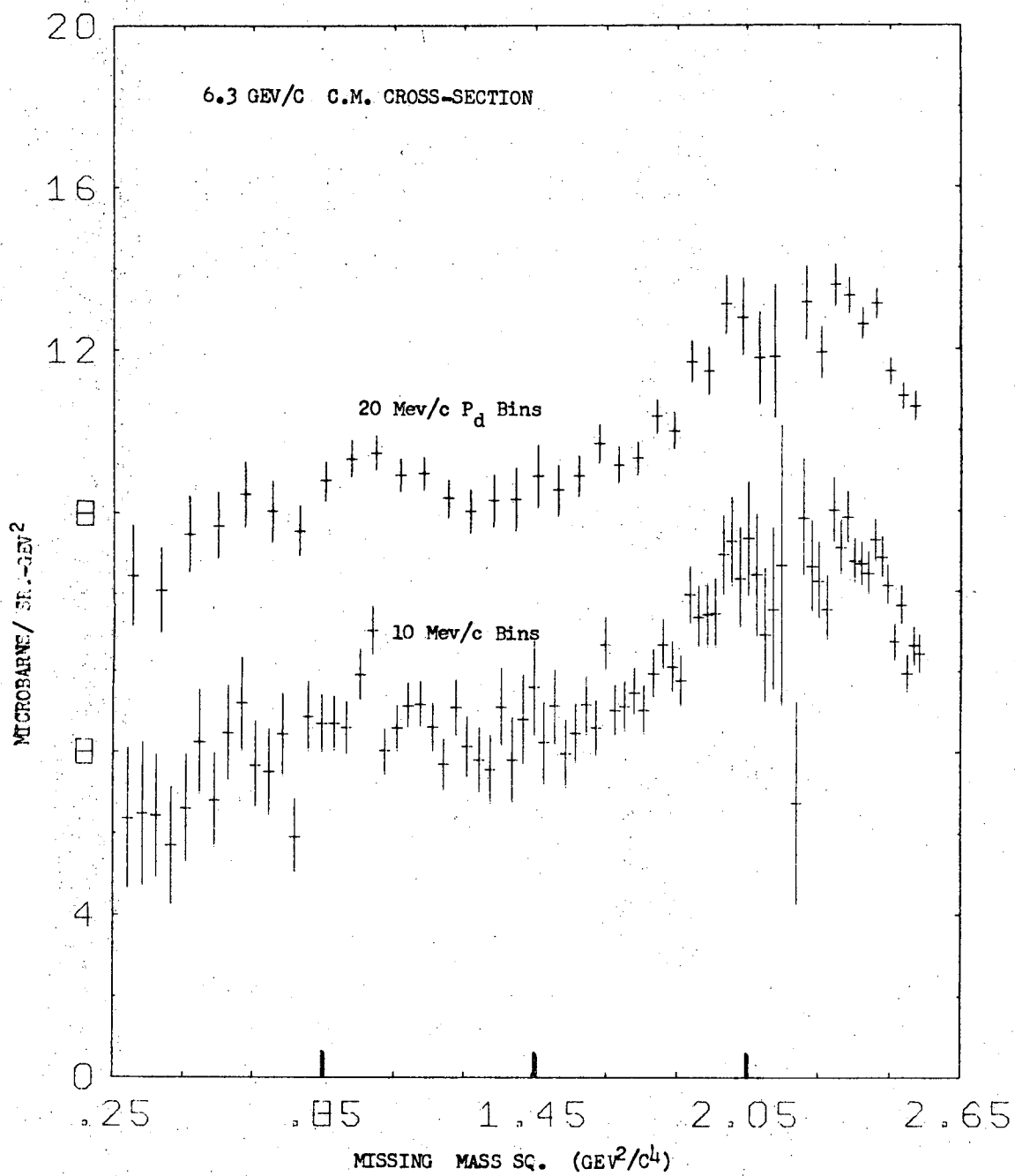


FIGURE 55

XBL 701-59

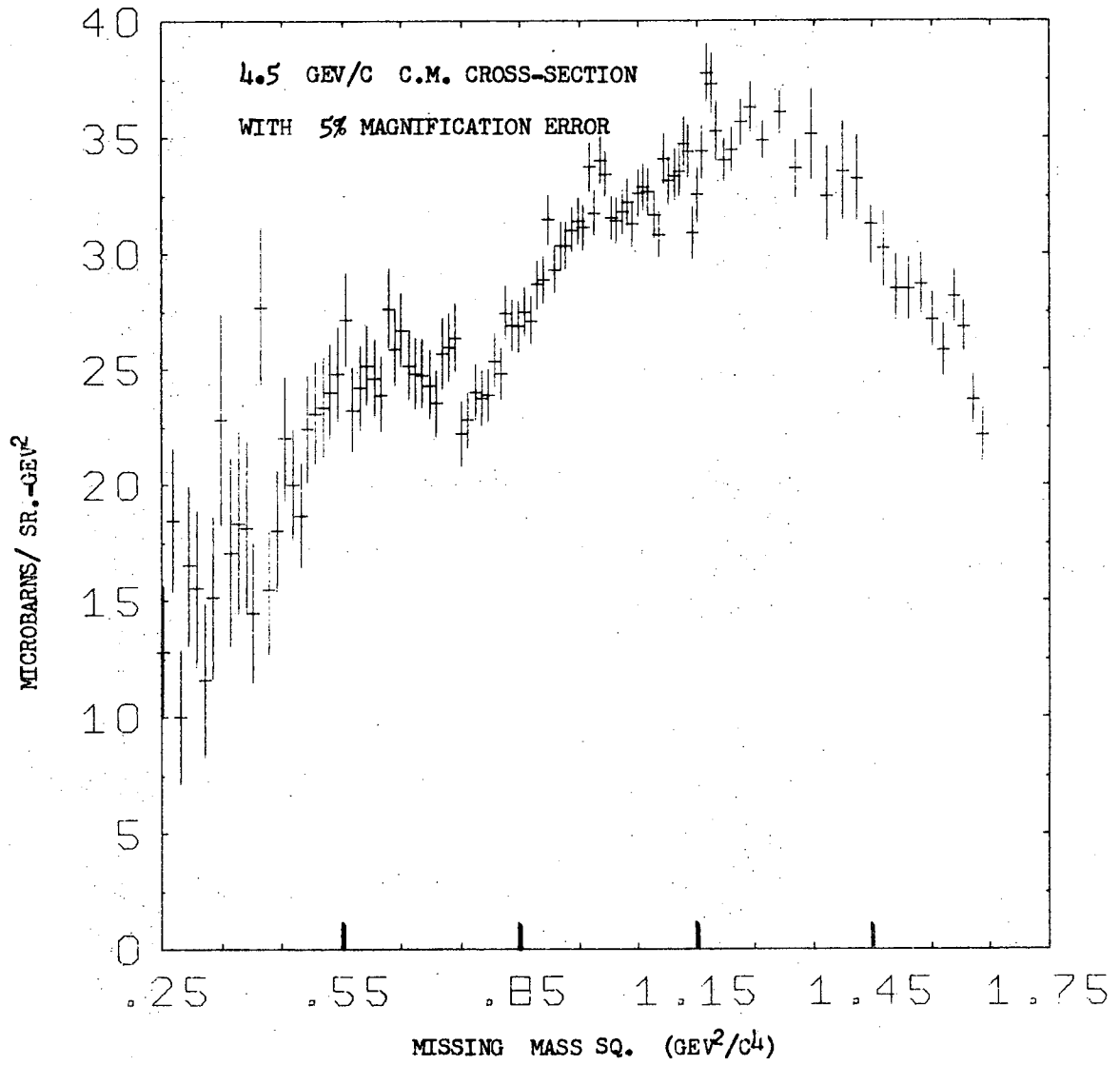


FIGURE 56

XBL 701-60

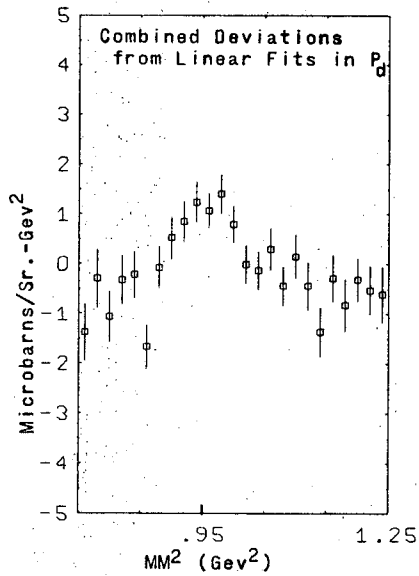


Figure 61

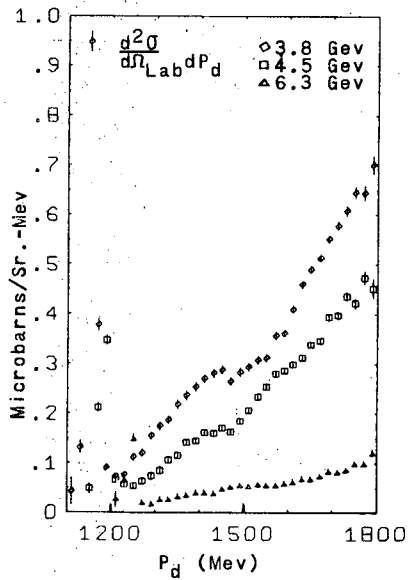
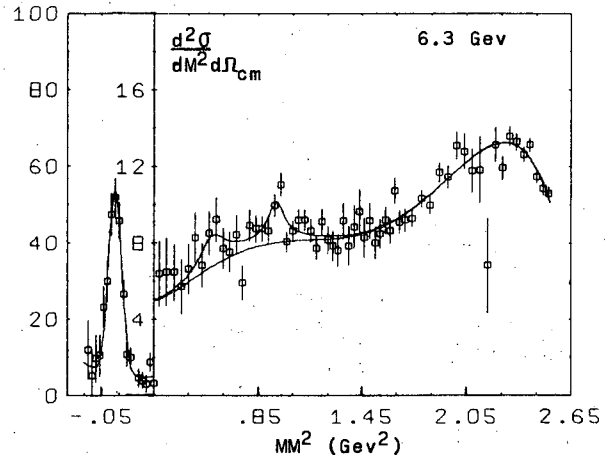
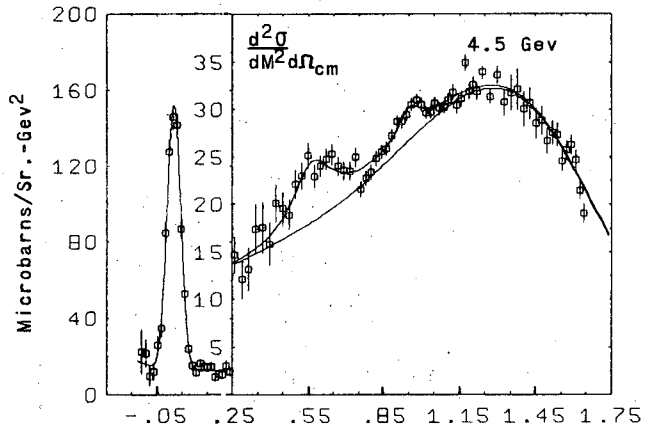
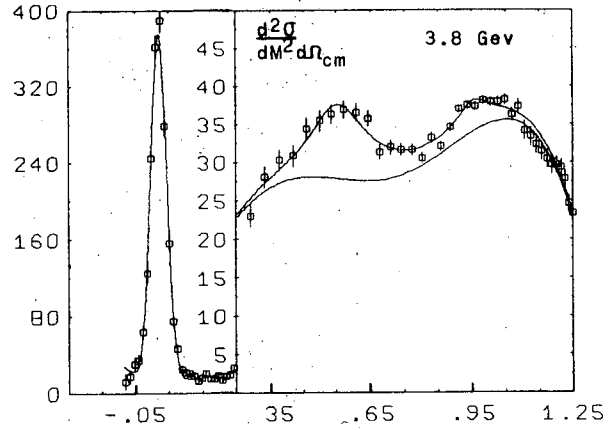


Figure 60



Figures 57,58,59 (Top to Bottom)

XBL 6912-6710

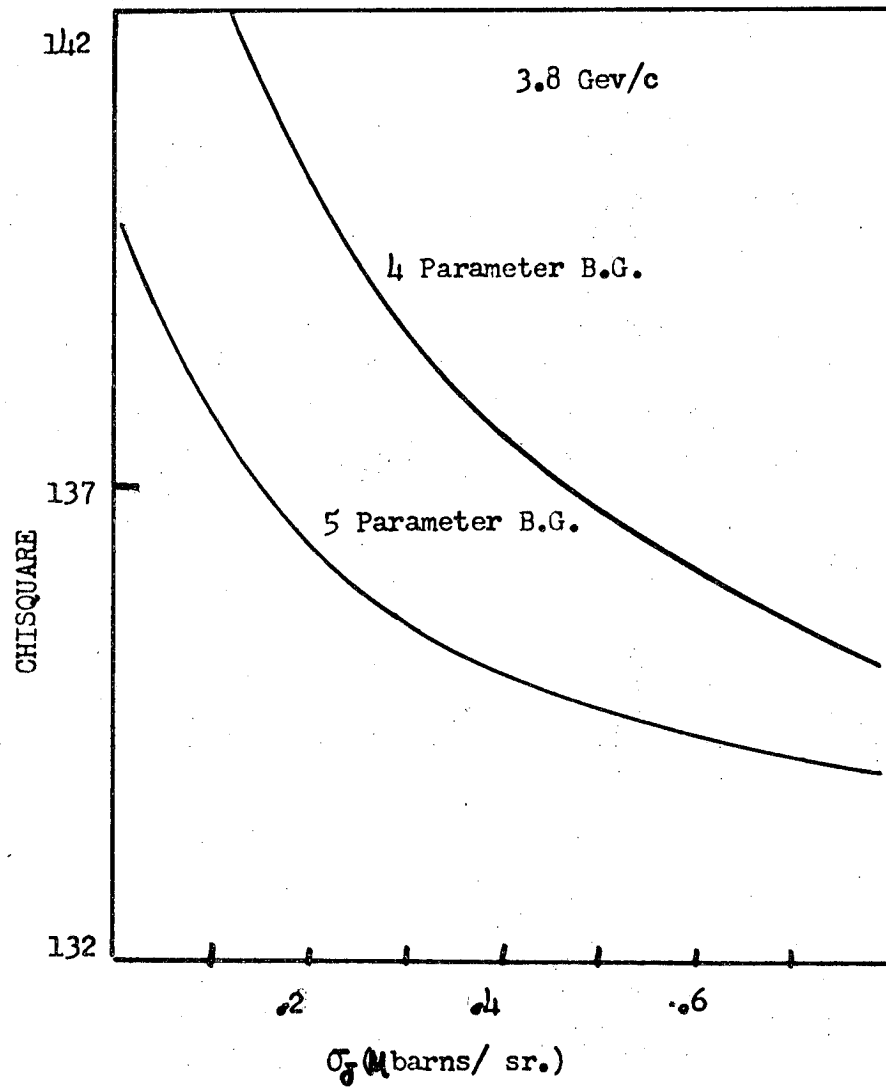


FIGURE 62-A

XBL 701-61

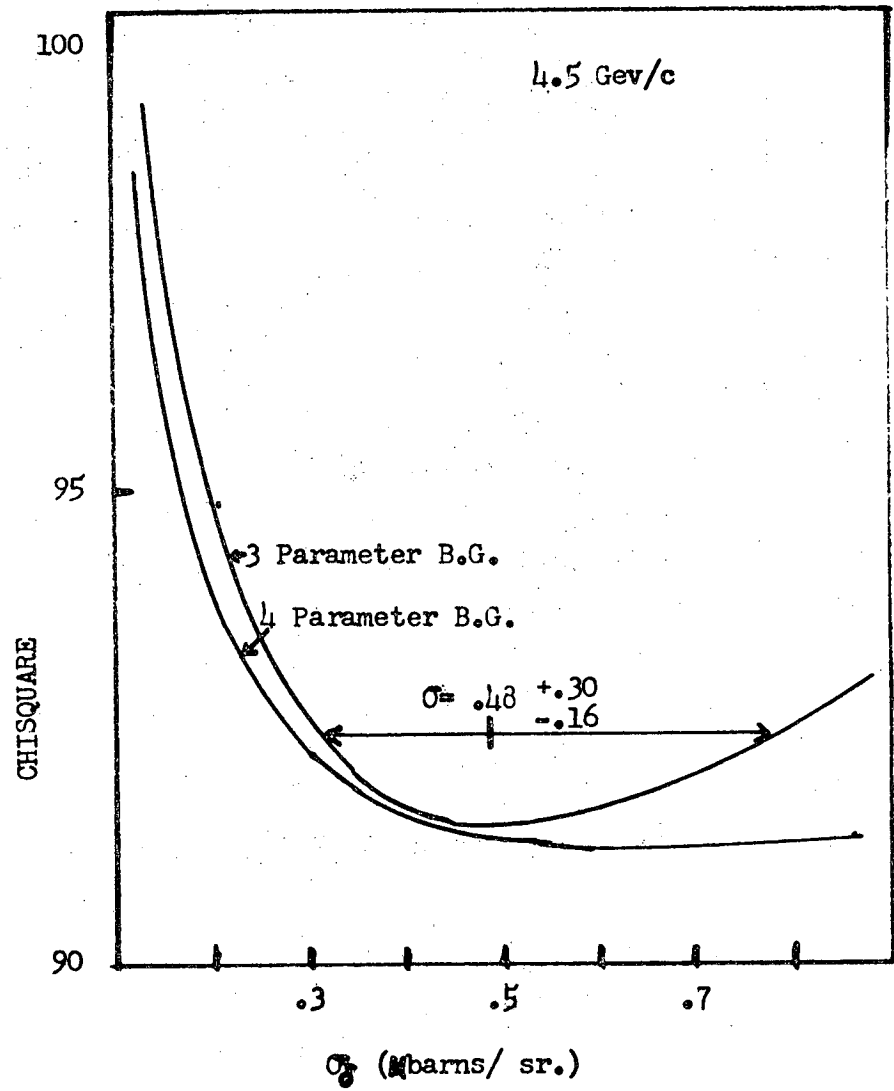


Figure 62-B

XBL 701-62

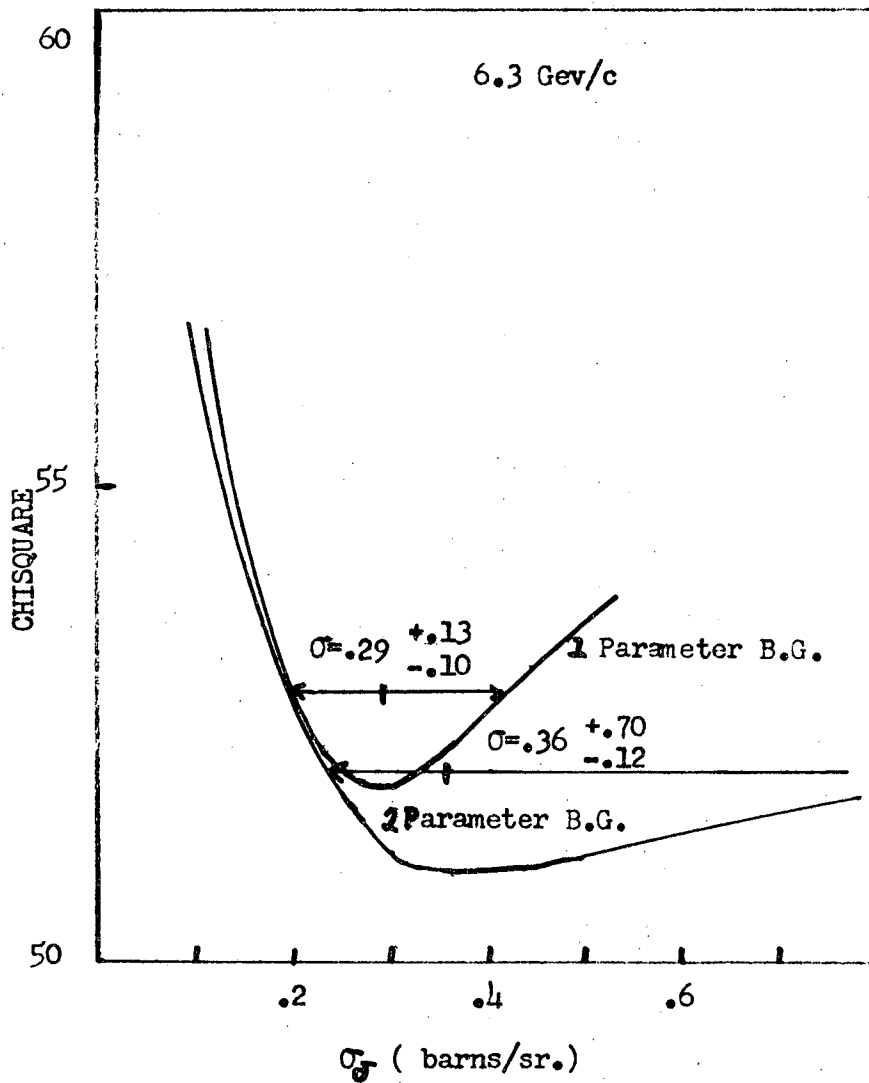


FIGURE 62-C

XBL 701-63

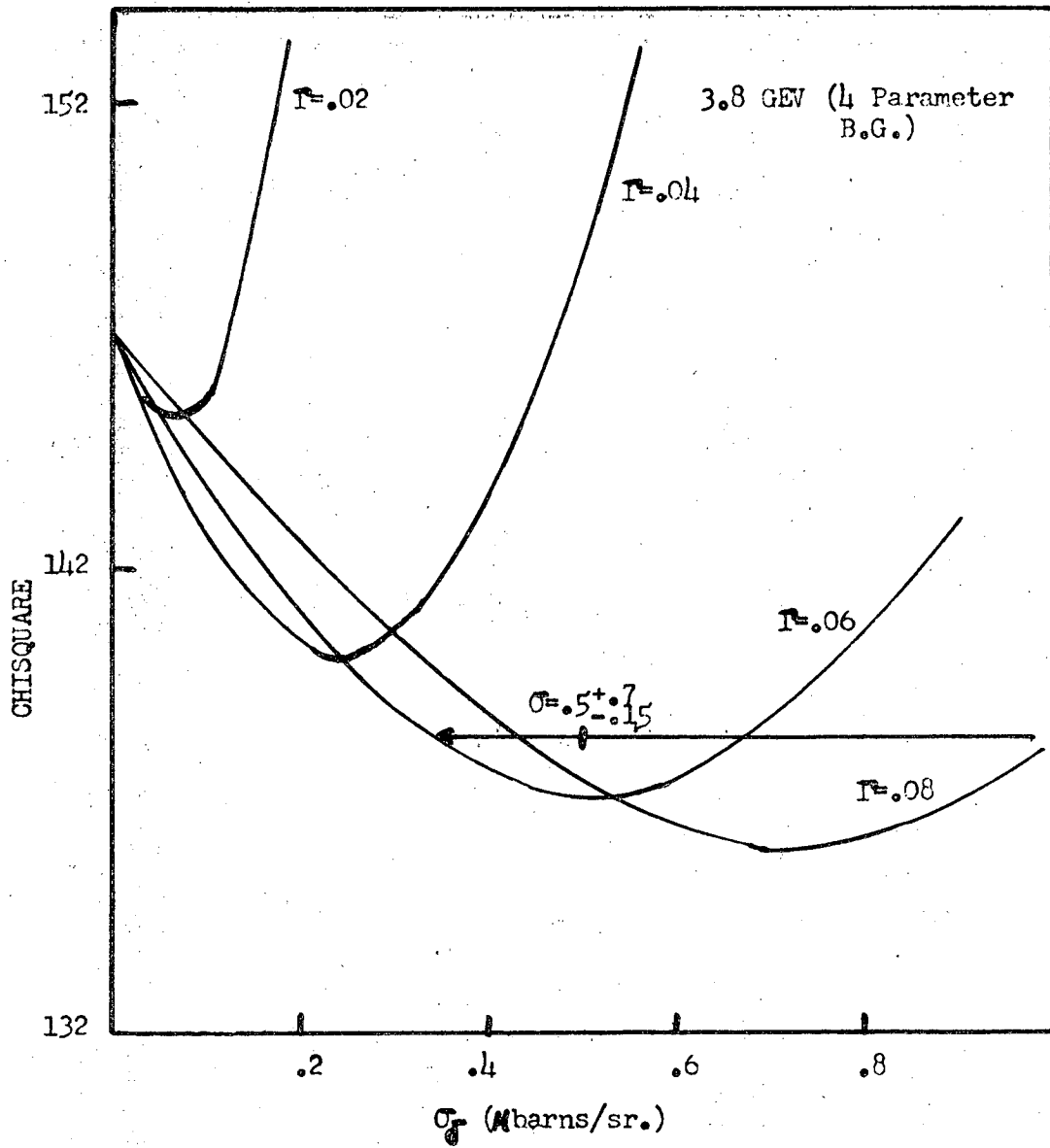


FIGURE 63-a

XBL 701-64

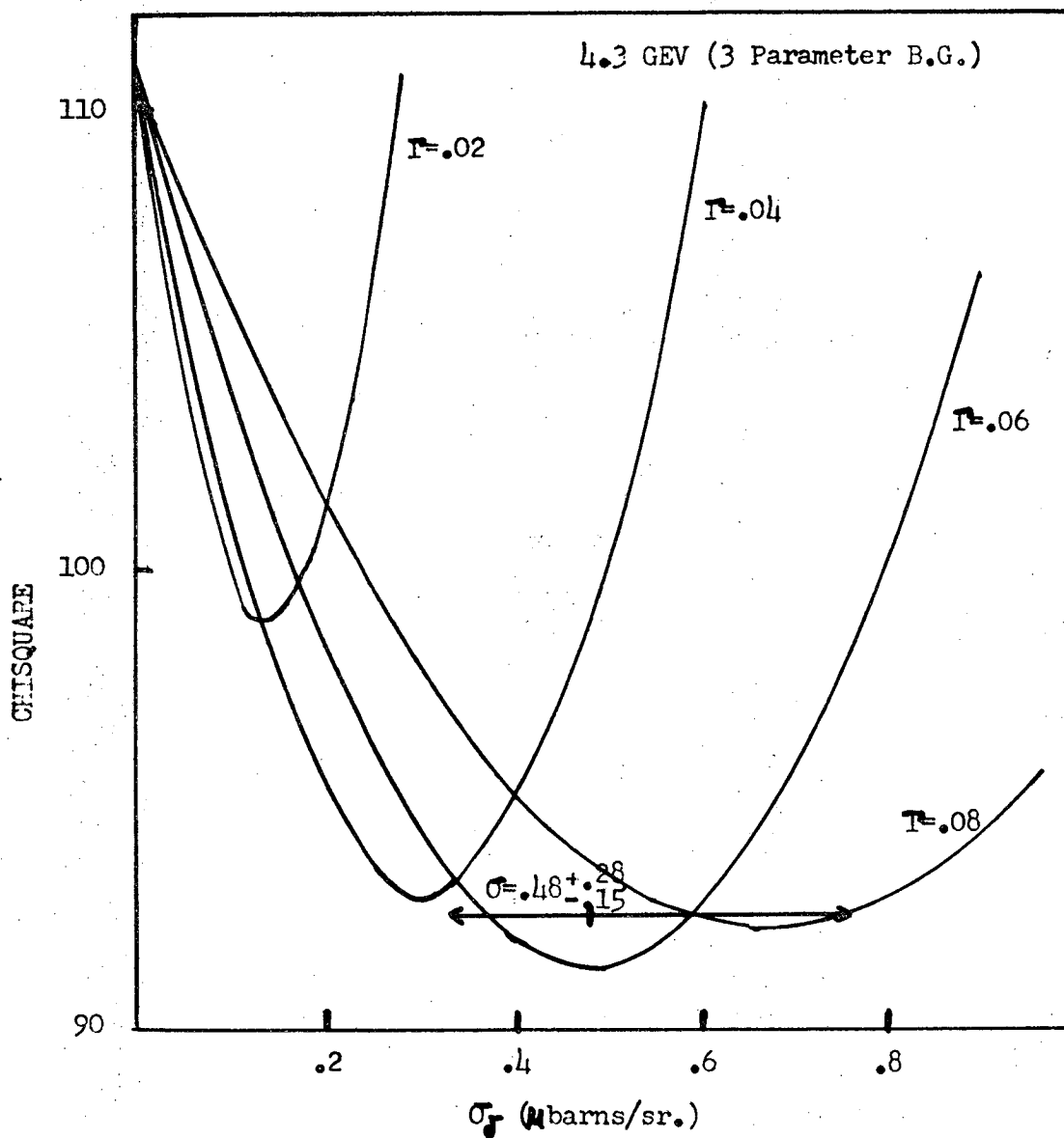


FIGURE 63-b

XBL 701-65

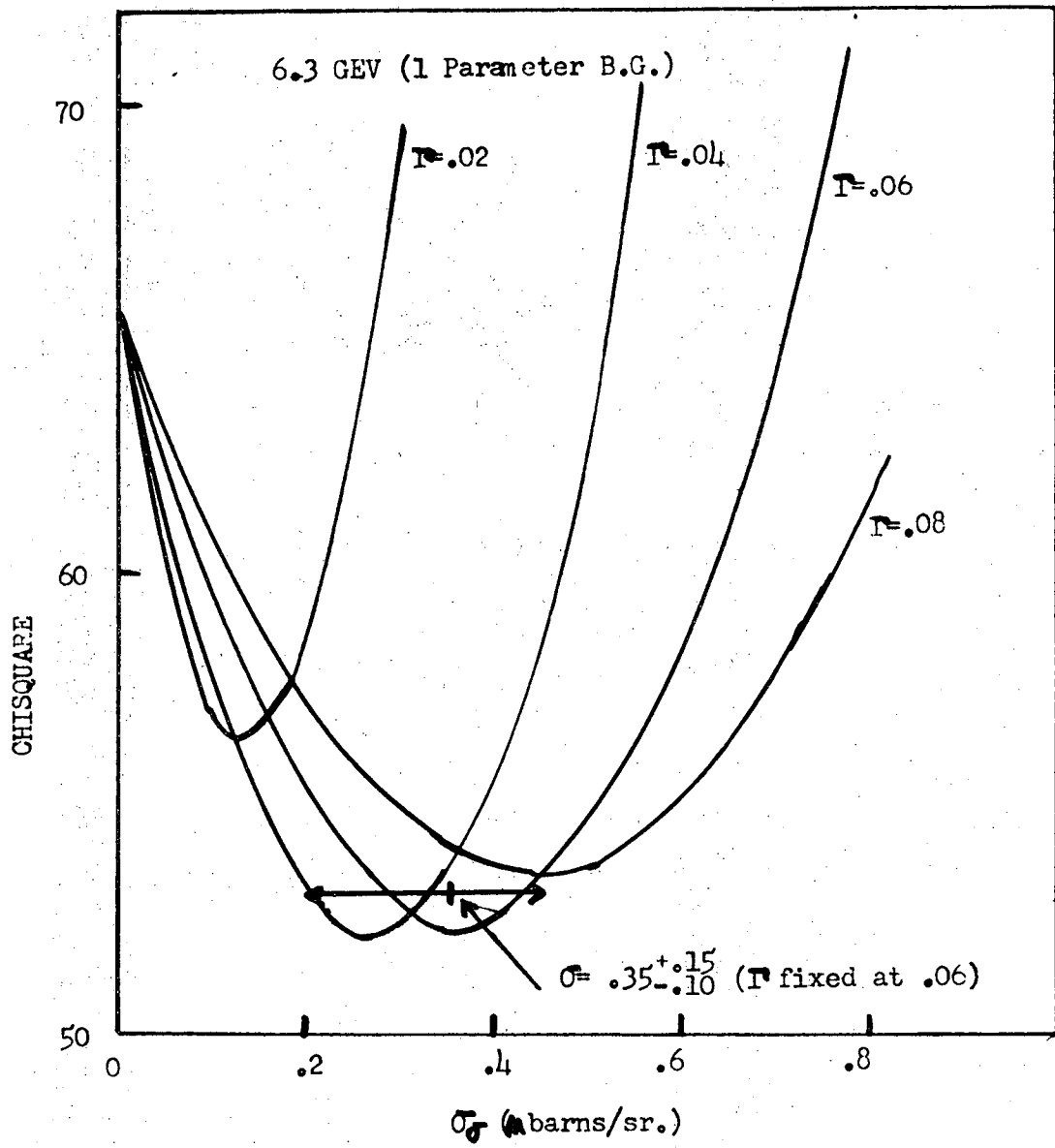


FIGURE 63-c

XBL 701-66

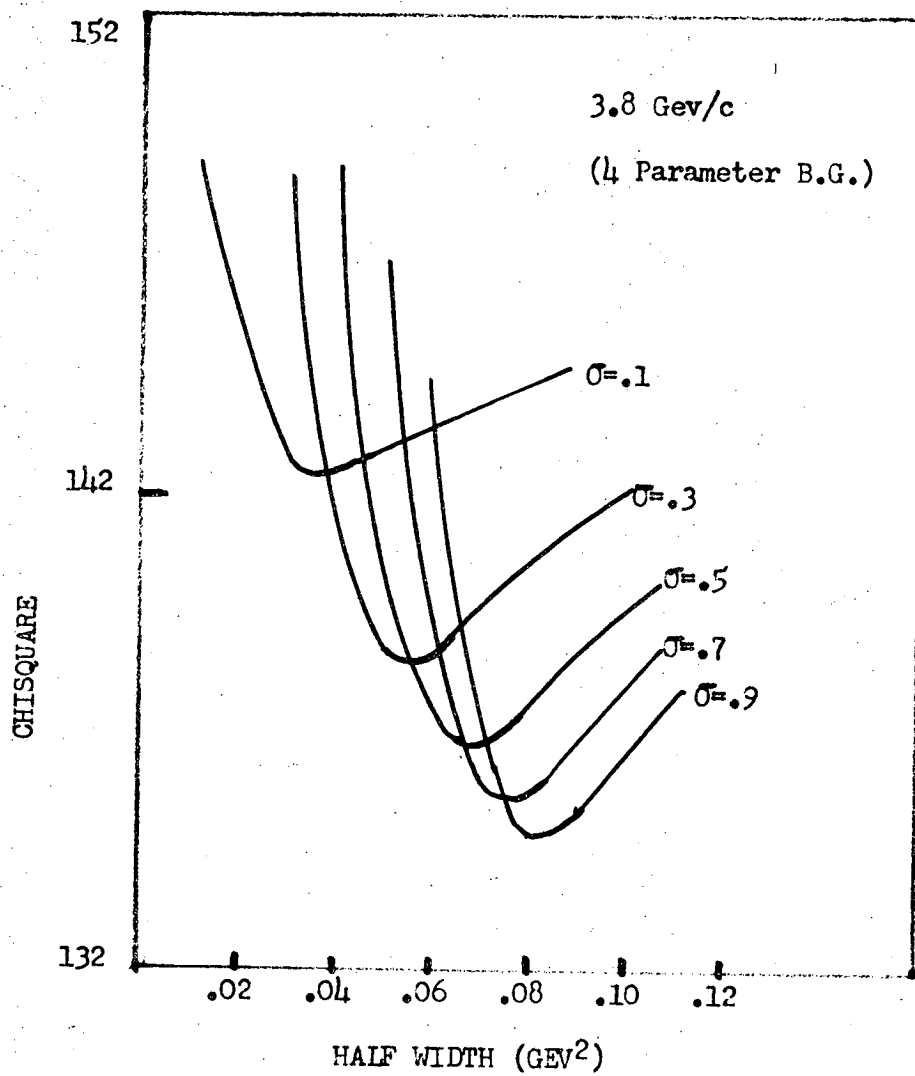


FIGURE 64-A

XBL 701-67

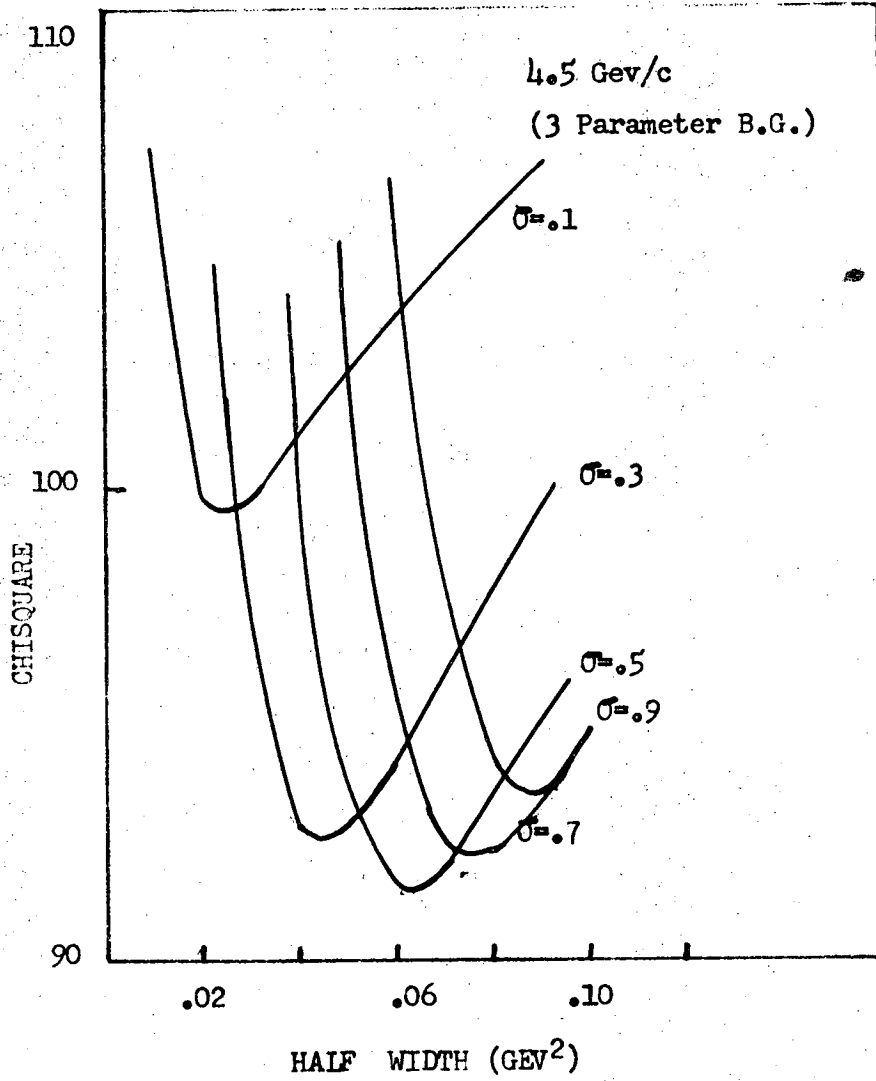


FIGURE 64-B

XBL 701-68

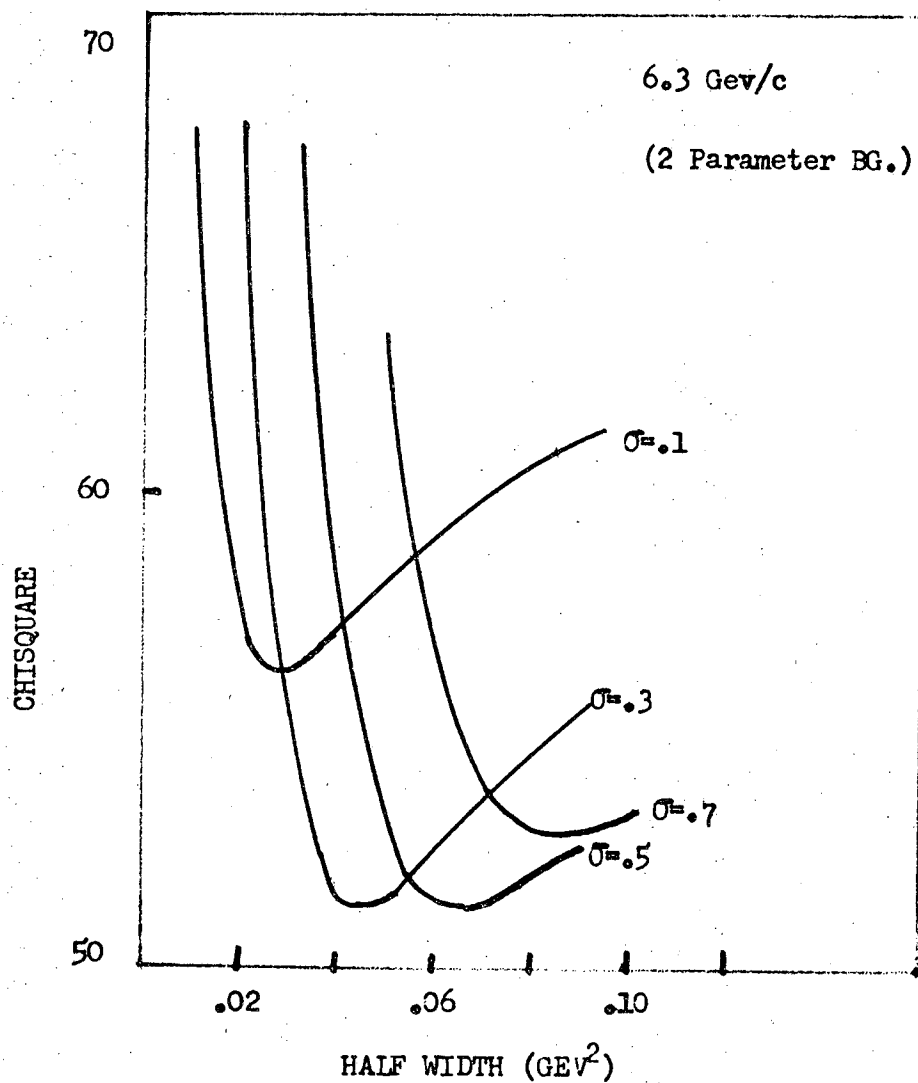


FIGURE 64-C

XBL 701-69

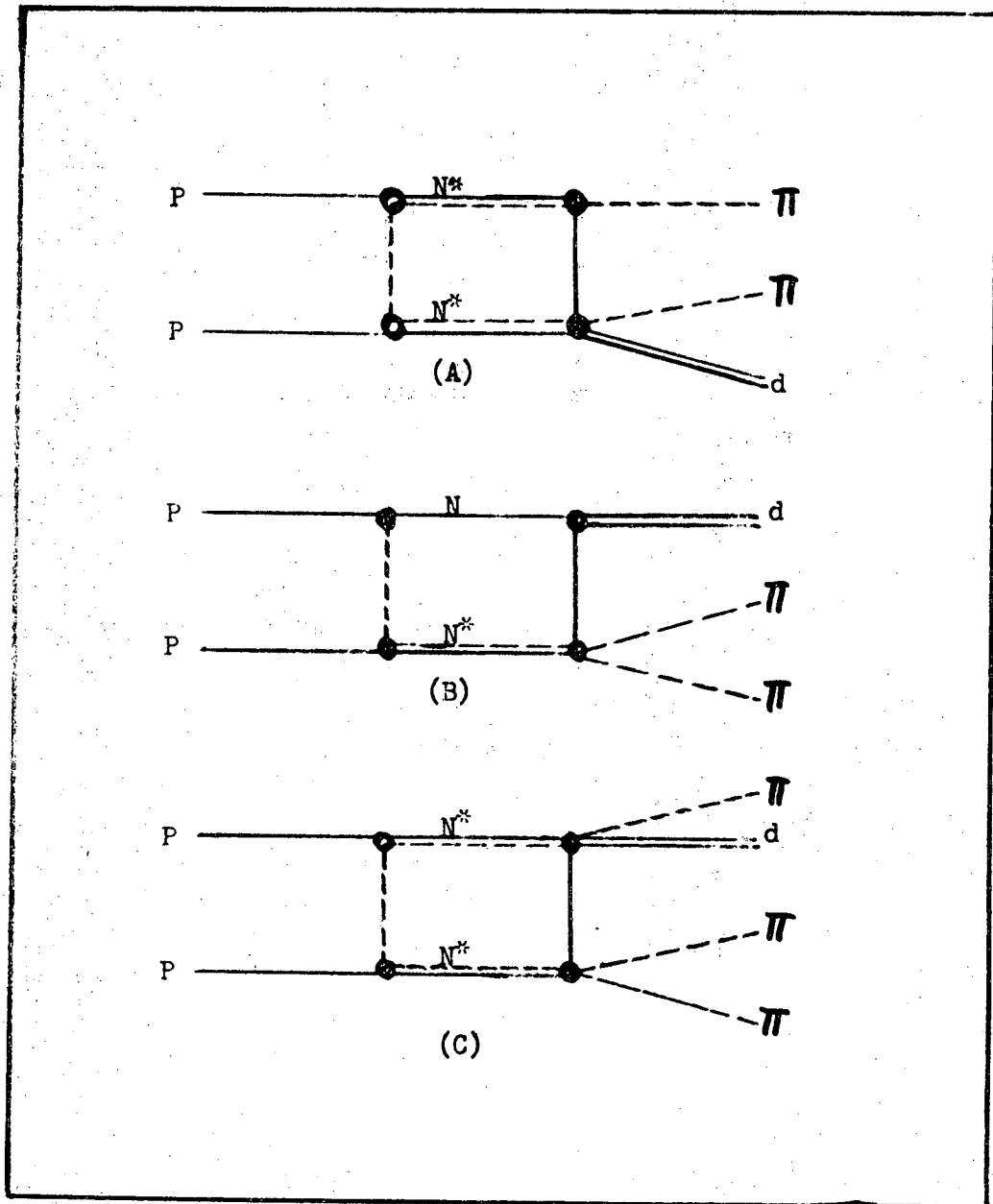


FIGURE 65

XBL 701-70

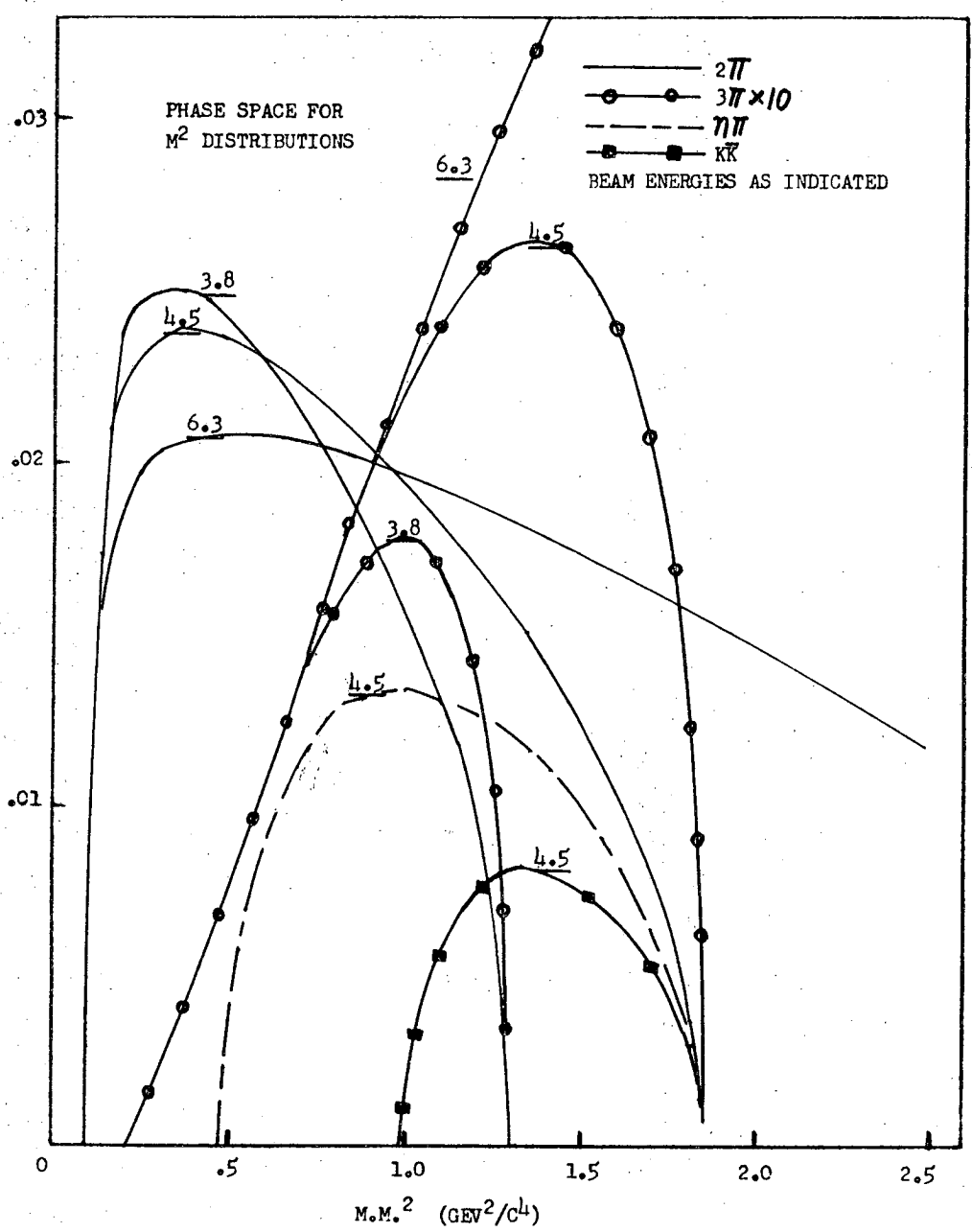


FIGURE 66

XBL 701-71

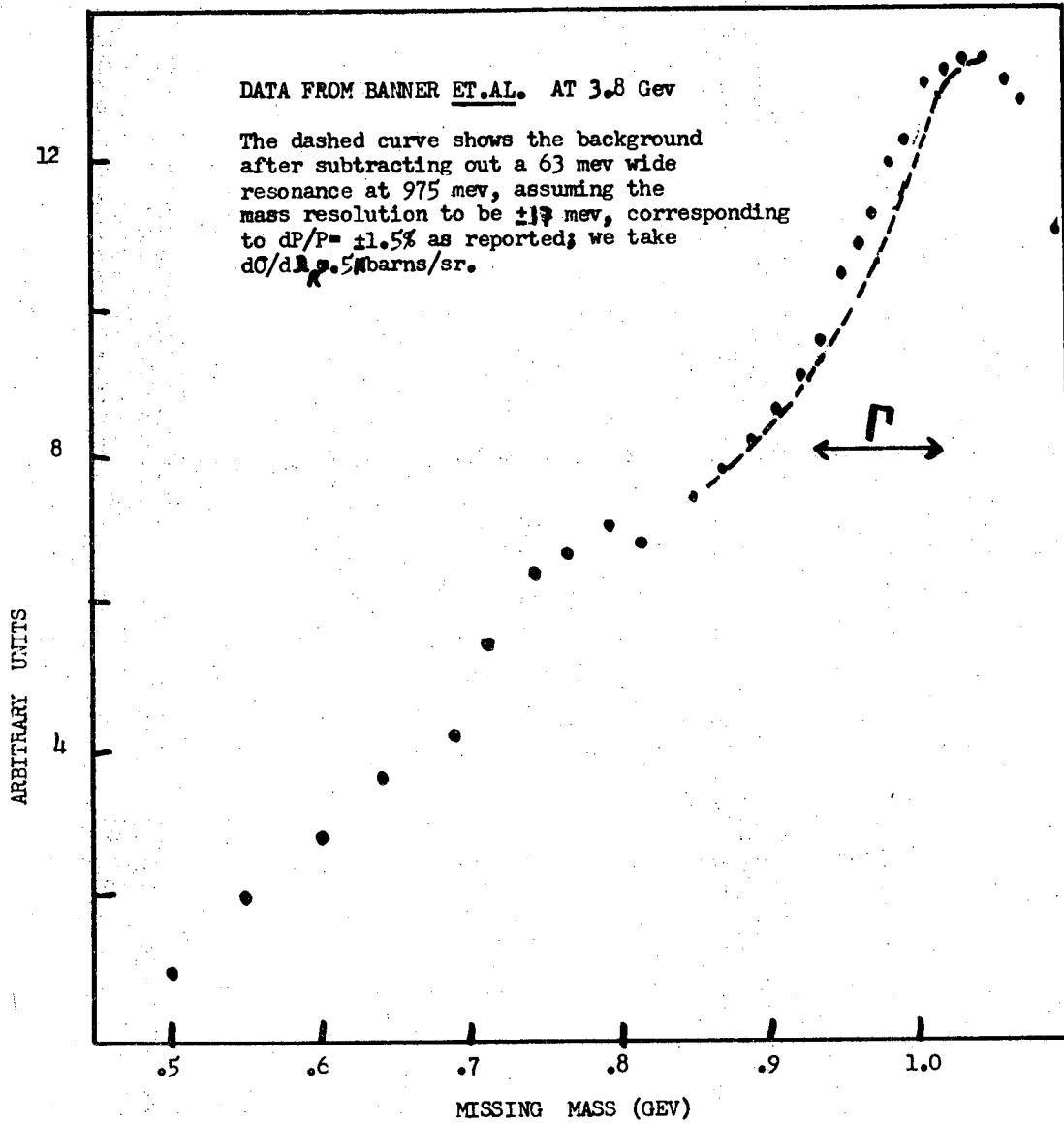


FIGURE 67

XBL 701-72

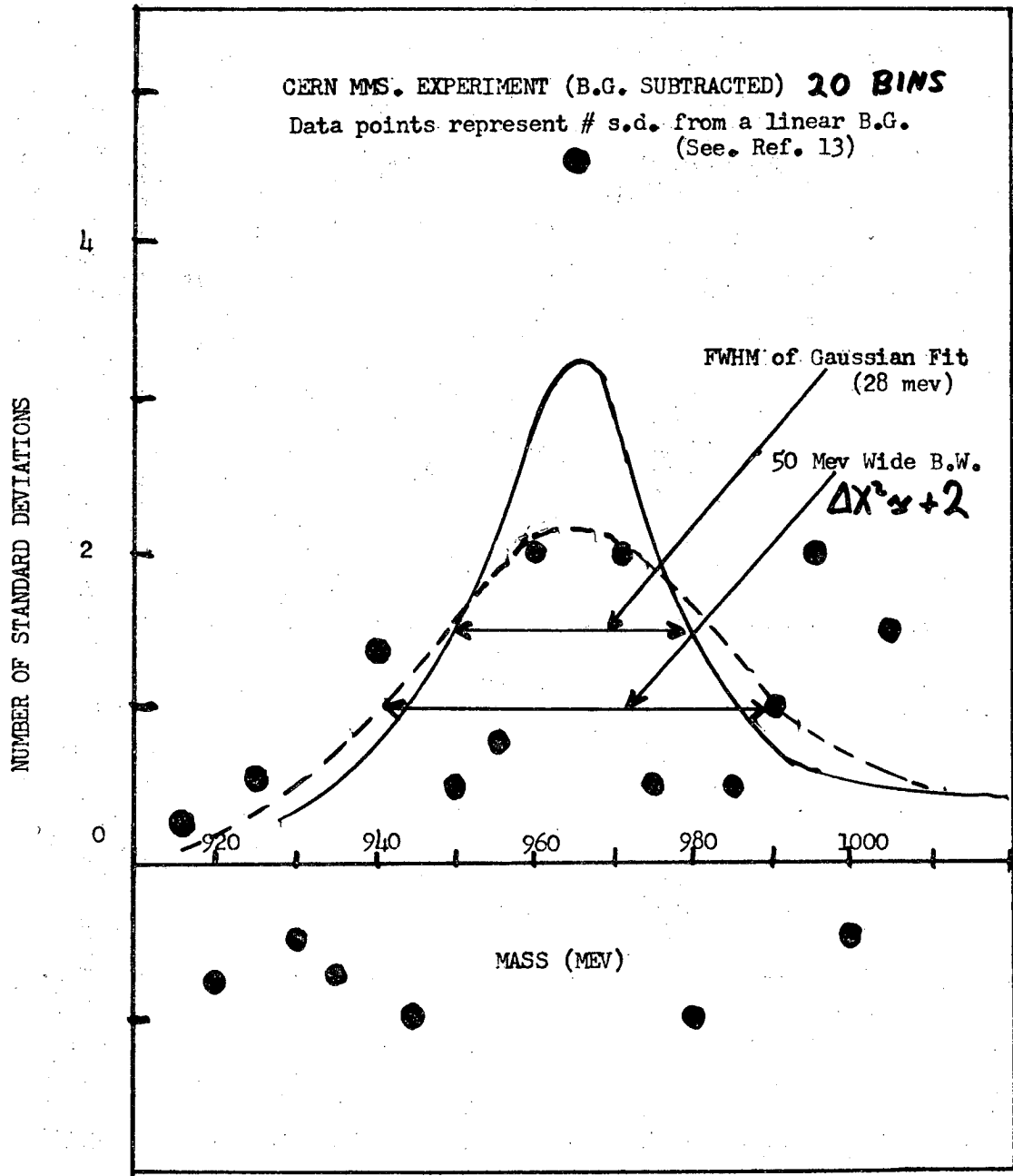


FIGURE 68

XBL 701-73

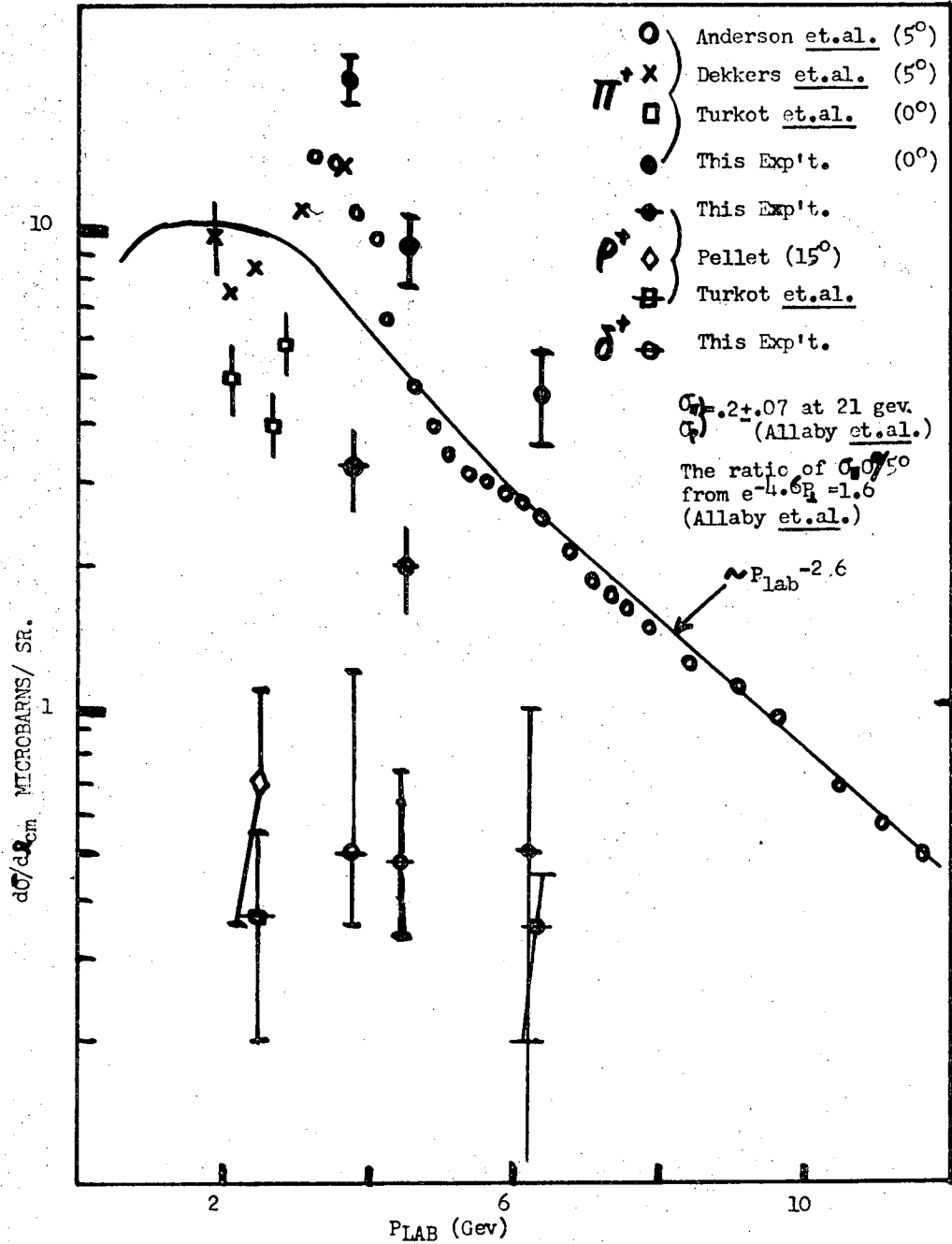


FIGURE 69

XBL 701-74

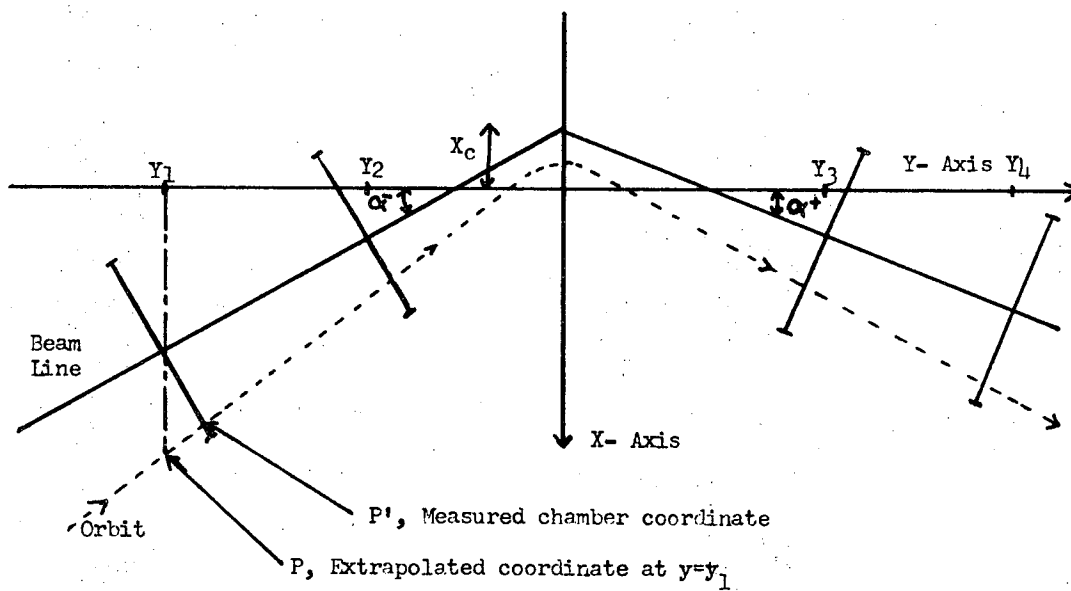


FIGURE 70

XBL 701-75

References:

- (1) N. P. Samios, ' Status of ρ and δ Bosons', Conference on Meson Spectroscopy at the University of Pennsylvania, 1968.
- (2) B. French, Rapporteur's Talk, 14'th Int'l. Conference on High Energy Physics, Vienna, 1968.
- (3) W. Kienzle, B. C. Maglic, B. Levrat, F. Lefebvres, D. Freytag, H. R. Blieden, Physics Letters 19, 438, 1965; M. N. Focacci, W. Kienzle, B. Levrat, B. C. Maglic, M. Martin, Phys. Rev. Letters, 17, 890, 1966.
- (4) J. Oostens, R. Chavanon, M. Crozon, J. Tocqueville, Physics Letters, 22, 708, 1966.
- (5) M. Banner, M. L. Fayoux, J. L. Hamel, J. Zsembery, J. Cheze, J. Teiger, Physics Letters 25B, 569, 1967.
- (6) M. Banner, M. L. Fayoux, J. L. Hamel, J. Zsembery, J. Cheze, J. Teiger, 300, 1967.
- (7) R. Ammar, R. Davis, W. Kropac, J. Mott, D. Slate, B. Werner, M. Derrick, T. Fields, and F. Schweingruber, Phys. Rev. Letters 21, 1832, 1968.
- (8) V. E. Barnes, S. U. Chung, R. L. Eisner, E. Flaminio, P. Guidoni, J. B. Kinson, N. P. Samios, D. Bassano, M. Goldberg, and K. Jaeger, Phys. Rev. Letters 23, 610, 1969.
- (9) D. J. Crennel, U. Karshon, K. W. Lai, J. S. O. Neall, J. M. Scarr, P. Baumel, R. M. Lea, T. G. Scumann, and E. M. Urwater, Phys. Rev. Letters 22, 1398, 1969
- (10) J. H. Campbell, S. Lichtman, F. J. Loeffler, D. H. Miller, R. J. Miller, W. J. Miller, R. B. Willman, Phys. Rev. Letters 22, 1204, 1969.
- (11) Ch. D'Andlau, A. Astier, M. Della-Negra, L. Dobrzynski, S. Wojcicki, J. Barlow, T. Jacobson, L. Montanet, L. Tallone-Lombardi, M. Tomas, A. M. Adamson, M. Baubillier, J. Duboc, M. Goldberg, E. Lew, D. Edwards, J. E. A. Lys, Physics Letters, 17, 347, 1965.

(12) A. Astier, J. Cohen-Ganouna, M. Della-Negra, B. Marechal, L. Montanet, M. Tomas, M. Baubillier, J. Duboc, Physics Letters 25B, 294, 1967.

(13) R. Dalitz, 'Mesonic Resonance States', Philadelphia Conference, 1968.

(14) J. E. Juhala, R. A. Leacock, J. I. Rhode, J. B. Kopelman, L. Marshall-Libby, E. Urvater, Physics Letters 27B, 257, 1968.

(15) W. Allison, A. Cruz, W. Schrankel, M. M. Haque, S. K. Tuli, P. J. Finney, C. M. Fisher, J. D. Gordon, R. M. Turnbull, R. Erskine, K. Sisterson, K. Paler, P. Chaudhuri, A. Eskreys, S. J. Goldsack, Physics Letters 25B, 619, 1967.

(16) R. Dalitz, Ann. Rev. Nuc. Science 13, 339, 1963.

(17) J. K. Kim, Phys. Rev. Letters 19, 1079, 1967; also W. Willis, H. Filthuth, P. Franzini, A. Minguzzi-Ranzi, A. Segar, R. Englemann, V. Hepp, E. Kluge, R. A. Burnstein, T. B. Day, R. G. Glasser, A. J. Herz, B. Kehoe, B. Sechi-Zorn, N. Seeman, G. A. Snow, Phys. Rev. Letters 13, 291, 1969.
We take $F/F+D = .41$

(18) Ignoring kinematic factors, the cross-section averaged over spins for resonance production is proportional to $M_r \gamma_r / q_r \cdot G_{NNM}^2$, where r is the resonance produced and 'M' is the exchanged meson. In the case of baryon exchange, we include a factor of 3 in the Rho production cross-section from the sum over final spin states (only one rho spin state is populated by spin zero exchange).

(19) E. W. Anderson, E. J. Bleser, H. R. Blieden, G. B. Collins, D. Garelick, J. Menes, F. Turkot, D. Birnbaum, R. Edelstein, N. C. Hien, T. J. McMahon, J. Mucci, J. Russ, Phys. Rev. Letters 22, 1390, 1969.

(20) P. A. Piroué and A. J. S. Smith, Phys. Rev. 148, 1315, 1966.

(21) R. M. Graven, F. D. Neu, H. H. Stellrecht, M. A. Torrano, M. A. Abolins, R. L. McCarthy, G. A. Smith, L. H. Smith, A. B. Wicklund, Nuclear Instruments and Methods 66, 125, 1968.

(22) I. V. Perez-Mendes, J. M. Pfab, Nucl. Instr. and Methods, 33, 141, 1965.

- (23) R. M. Bozorth, Ferromagnetism, N. Y., Van Nostrand, 1951.
- (24) W. A. Wenzel, 'Bevatron External Proton Beam', International Conference on High Energy Accelerators, Dubna, 1963.
- (25) 'Bevatron Experimenters' Handbook, 1967.
- (26) F. Macondray, U. C. R. L. Report 17642.
- (27) D. E. Pellett, Thesis, University of Michigan Tech. Report 26; J. B. Cumming, J. Hudis, A. M. Poskanzer, and S. Kaufman, Phys. Rev. 128, 2392, 1962.
- (28) J. Barale, 'Calibration of Secondary Emission Foils for Bevatron E. P. B. Measurements, Bevatron Report EET-929.
- (29) H. L. Anderson, M. Dixit, H. J. Evans, K. A. Klare, D. A. Larson, M. V. Sherbrook, R. L. Martin, K. W. Edwards, D. Kessler, D. E. Nagle, H. A. Thiessen, C. K. Hargrove, E. P. Hincks, S. Fukui, Phys. Rev. Letters 21, 853, 1968.
- (30) J. D. Jackson, 'On the Phenomenological Analysis of Resonances', Nuovo Cimento 34, 1644, 1964; We use eq. A-7 in appendix A to describe the Rho width; this choice is somewhat arbitrary, given the large background under the Rho.
- (31) C. Defoix, P. Rivet, J. Siaud, B. Conforto, M. Widgoff, F. Shively, Physics Letters 28B, 353, 1968.
- (32) D. Dekkers, B. Jordan, R. Mermod, C. C. Ting, G. Weber, T. R. Willitts, K. Winter, X. DeBouard, M. Vivargent, Physics Letters 11, 161, 1964.
- (33) F. Turkot, G. B. Collins, and T. Fujui, Phys. Rev. Letters 11, 474, 1963.
- (34) J. V. Allaby, F. Binon, A. N. Diddens, R. Duteil, A. Klovning, R. Meunier, J. P. Peigneux, E. J. Sacharidis, K. Schlupmann, M. Spighel, J. P. Stroot, A. M. Thorndike, and A. M. Wetherell, Proc. of the XIV'th Int'l. Conf. on High Energy Physics, Vienna, 1968.
- (35) V. Barger and C. Michael, Phys. Rev. Letters, 22, 1330, 1969.
- (36) T. Yao, Physical Review 134B, 454, 1964.

- (37) See J. D. Jackson, Classical Electrodynamics, Ch. 13; Ashmore, 'Multiple Scattering of Charged Particles', High Energy and Nuclear Physics Data Handbook, The Nat'l. Institute for Research in Nucl. Sci., Rutherford High Energy Lab., 1963.
- (38) M. Derrick, 'Mesons', Boulder Conference, 1969; ANL/HEP Report 6921.
- (39) A. B. Wicklund, 'Rapid Spectrometer Analysis', U. C. R. L. Report 18317.
- (40) F. T. Solmitz, 'Analysis of Experiments in Particle Physics', Ann. Rev. of Nucl. Science, 14, 1964.

Acknowledgments:

I wish to thank Walter D. Hartsough and the Bevatron staff for their skillful assistance during the run. I acknowledge the efforts of my colleagues who participated in the planning and execution of this experiment- Bob Graven, Hans Stellrecht, Fred Kreiss, Glenn Armstrong, Mike Torrano, Bob Gilmer, Frank Neu, and Buck Buckingham, and Drs. Maris Abolins, Larry Smith, David Pellett, Richard Lander, and Bob McCarthy. Special thanks are due to Professor Gerald Smith for guidance throughout my graduate career. I thank my fellow graduate students and members of group A for many helpful discussions. Finally, I wish to acknowledge the support and encouragement of Professor Luis Alvarez during my graduate years. The funds for this work were granted by the U. S. Atomic Energy Commission.

LEGAL NOTICE

This report was prepared as an account of Government sponsored work. Neither the United States, nor the Commission, nor any person acting on behalf of the Commission:

- A. Makes any warranty or representation, expressed or implied, with respect to the accuracy, completeness, or usefulness of the information contained in this report, or that the use of any information, apparatus, method, or process disclosed in this report may not infringe privately owned rights; or*
- B. Assumes any liabilities with respect to the use of, or for damages resulting from the use of any information, apparatus, method, or process disclosed in this report.*

As used in the above, "person acting on behalf of the Commission" includes any employee or contractor of the Commission, or employee of such contractor, to the extent that such employee or contractor of the Commission, or employee of such contractor prepares, disseminates, or provides access to, any information pursuant to his employment or contract with the Commission, or his employment with such contractor.

TECHNICAL INFORMATION DIVISION
LAWRENCE RADIATION LABORATORY
UNIVERSITY OF CALIFORNIA
BERKELEY, CALIFORNIA 94720